Discovery of antiskarn-hosted strategic metal mineralization in the Upper Cretaceous Twihinate carbonatite intrusion (West African Craton Margin, Moroccan Sahara)

Bouabdellah, Mohammed; Boukirou, Wissale; Jébrak, Michel; Bigot, Florent; Yans, Johan; Mouttaqi, Abdellah; El Gadarri, Mohamed; Errami, Abdellatif; Levresse, Gilles

Published in:
Ore Geology Reviews

DOI:
10.1016/j.oregeorev.2022.105105

Publication date:
2022

Document Version
Publisher's PDF, also known as Version of record

Ore Geology Reviews 149 (2022) 105105

Contents lists available at ScienceDirect

Ore Geology Reviews

journal homepage: www.elsevier.com/locate/oregeorev

Discovery of antiskarn-hosted strategic metal mineralization in the Upper Cretaceous Twihinate carbonatite intrusion (West African Craton Margin, Moroccan Sahara)

Mohammed Bouabdellah [a,*], Wissale Boukirou [a,*], Michel Jébrak [b], Florent Bigot [b], Johan Yans [c], Abdellah Mouttaqi [d], Mohamed El Gadarri [d], Abdellatif Errami [d], Gilles Levresse [e]

[a] Laboratoire des Gîtes Minéraux, Hydrogéologie & Environnement, Faculté des Sciences, 60000 Oujda, Morocco
[b] Department of Earth and Atmospheric Sciences, UQAM, CP 8888 Centre Ville, Montréal, Québec H3C3P8, Canada
[c] Institute of Life-Earth-Environment (ILEE), University of Namur, 61 rue de Bruxelles B-5000, Namur, Belgium
[d] Office National des Hydrocarbures et des Mines, 5 Avenue Moulay Hassan, Rabat, Morocco
[e] Programa de Geofluidos, Centro de Geociencias UNAM-Campus Juriquilla, AP 1-253, Querétaro, México CP 76230, Mexico

ARTICLE INFO

Keywords:
Carbonatite
Strategic metals
Antiskarn
Silica contamination
Moroccan Sahara

ABSTRACT

The Upper Cretaceous Twihinate carbonatite in Moroccan Sahara, which is the focus of ongoing exploration for Nb-P-Fe ± LREE ± U-Th resources, consists of a crescent-like intrusion made of a central sövite body encircled by an annular ring of vuggy siliceous breccia. Drill core logging coupled with petrographic observation, whole-rock and mineral chemistry reveal that the metasomatic interaction between the carbonatite melt and the silicate wall-rocks led to development of calc-silicate paragenesis within the sövite itself at depths ranging from ~60 to >200 m from the surface for which the term antiskarn is attributed. We provide the first petrographic and textural descriptions, and report the whole-rock major- and trace-element geochemistry and chemical compositions of the main antiskarn-forming minerals and related strategic metal-bearing ore. Geochemically, the antiskarn lithotypes are characterized by a compositional range of 7–17 wt% SiO_2, 25–72 wt% CaO, 1–2 wt% Al_2O_3, and 12–26 wt% loss on ignition, and enrichment in large-ion lithophile elements (LILE), particularly Sr (3125–7018 ppm ppm), Ba (393–1300 ppm), U (10–787 ppm) and light REEs (LREEs) (1058–1569 ppm), but not in the heavy REE (HREEs) and high-field strength elements (HFSE) such as Ti, Zr, Ta and Hf. Nb and V show, however, much higher concentrations ranging from 140 ppm to >1000 ppm, and 603 to 1008 ppm, respectively. Mineralogically, the antiskarn lithotypes consist predominantly of diopsidic (Di_{66-82} Hd_{18-34}) to aegirine-augite clinopyroxene (Di_{38-55} Ae_{21-35}) and andradite (And_{86-94} Gro_{1-9}) with subordinate amounts of micas (biotite/phlogopite) and titanite. The paragenetically later mineral assemblages involve amphibole, chlorite, epidotes, baryte, fluorite, kaolinite, carbonates and quartz. The main Nb-P-Fe ± LREE ± U-Th ore minerals consist of Fe oxides (titanomagnetite principally), pyrochlore group minerals, phosphates (apatite, monazite-(Ce)), and REE-fluorcarbonates (bastnäsite-(Ce)) with subordinate sulfides (chalcopyrite, sphalerite, and galena), fluorite and baryte. Development of the antiskarn calc-silicate paragenesis and related strategic metal-bearing mineralization is consistent with derivation from a carbonatite melt through assimilation of silicate country rocks including the Silurian-Devonian gneissic granitoid of the Laknouk suite. From an economic perspective, the widespread occurrence of high-Ti (0.7–16. 9 wt% Ti) and V- (0.2–0.7 wt% V) magnetite opens new opportunities in regard of exploration for V; an emerging strategic commodity whose presence has to be reassessed in the Twihinate prospect. The currently described antiskarn paragenesis may be therefore used as reliable exploration metallotect to target prospective occurrences in the search for critical metals including V as by product.

* Corresponding authors.
E-mail addresses: mbouabdellah2002@yahoo.fr (M. Bouabdellah), wissale.boukirou@fso.ump.ac.ma (W. Boukirou).

https://doi.org/10.1016/j.oregeorev.2022.105105
Received 16 April 2022; Received in revised form 7 September 2022; Accepted 12 September 2022
Available online 14 September 2022

1. Introduction

Although volumetrically insignificant among igneous rocks, carbonatites and their metasomatized and weathered derivatives stand out as the ones most targeted rock types as they provide most of the world's strategic metals production such as niobium, rare earth elements (REE), tantalum, phosphorous, copper, iron and fluorine (Chakhouradian and Wall, 2012; Verplanck et al., 2016; Goodenough et al., 2018; Simandl and Paradis, 2018; Anenburg et al., 2021). The exponentially increased demand for these high technology elements has provided an impetus for numerous mineral exploration and research projects focused on carbonatites and their genetically related alkaline silicate counterparts (Wall, 2014; Weng et al., 2015). Currently, about 10% of all documented carbonatite occurrences (50/630) are mined for those elements and about 40% of all REE exploration projects focus on carbonatites (Chakhouradian and Wall, 2012; Wang et al., 2020; Gonzàlvez-Alvarez et al., 2021).

Because of their extremely low viscosities, rapid ascent rates and, hence, short residence times within the crust (Pyle et al., 1991) together with their high enrichment in some incompatible trace elements (e.g., Sr, Ba and REEs) relative to crustal abundances, the mantle-derived carbonate melts are not supposed to be easily affected by crustal contamination (e.g., Bell, 1989). However, there is a growing number of petrographic (e.g., Chakhmouradian et al., 2008; Giebel et al., 2019, Anenburg et al., 2020a; Chmyz et al., 2022; Walter et al., 2022) and experimental studies (e.g., Anenburg and Mavrogenes, 2018) which contradicts this statement pointing instead for the role of crustal contamination in the deeply-derived carbonatite parental melt during ascent and subsequent emplacement. In this respect, recent experiments show that carbonatite metasomatism could occur between carbonatite melt and silicate rocks at decreasing magmatic temperatures from >700 °C down to 400 °C (e.g., Anenburg and Mavrogenes, 2018). The

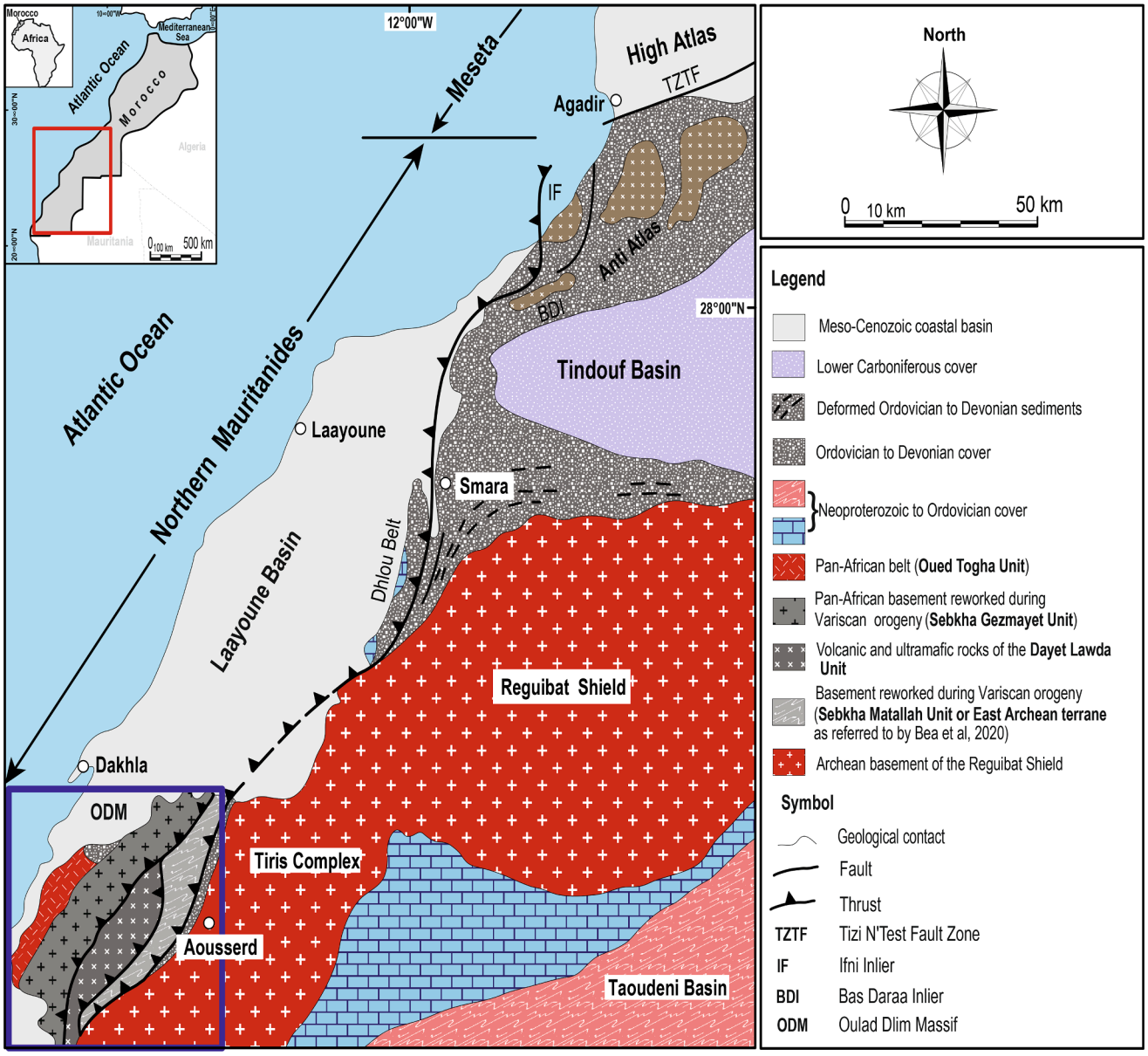

Fig. 1. Geological map of southern Morocco showing the main structural domains and lithological units along with location of the Oulad Dlim massif within the Souttoufide belt (i.e., Northern Mauritanides) and Western Reguibat shield (Modified after Michard et al., 2010, Villeneuve et al., 2015). Names of major cities are also indicated. The inset map in the upper and lower left corners show the location of the southern provinces of Morocco and Oulad Dlim massif within the framework of Africa and the southern part of Morocco, respectively.

resulting mineral assemblages resemble those successions commonly described in skarn-like deposits (Meinert et al., 2005). For a such assemblages, the term antiskarn has been introduced (Anenburg and Mavrogenes, 2018), and since then there is a wide growing acceptance for the use of this concept (Giebel et al., 2019; Anenburg et al., 2020a; Cangelosi et al., 2020; Chmyz et al., 2022; Walter et al., 2022).

In Morocco, the largest outcropping carbonatite rocks occur within the Eocene Tamazert alkaline complex in the central High Atlas Mountains where no economic mineralization has been documented so far (e.g., Bouabdellah et al., 2010). In 2007 and onward, discoveries of new carbonatite intrusions were reported by the Moroccan Office of Hydrocarbon and Mines (ONHYM) throughout the Oulad Dlim massif in the Moroccan Sahara, adjacent to the West African Craton (WAC) margin (Bouabdellah et al., 2012; Bouabdellah, 2013; Montero et al., 2016; Benaouda et al., 2020a,b; Boukirou et al., 2022) (Figs. 1, 2). Of these, the Twihinate carbonatite intrusion (22°17′N, 16°02′W) which is the focus of this contribution was discovered following regional airborne electromagnetic and gravimetric exploration surveys. Subsequent ground-

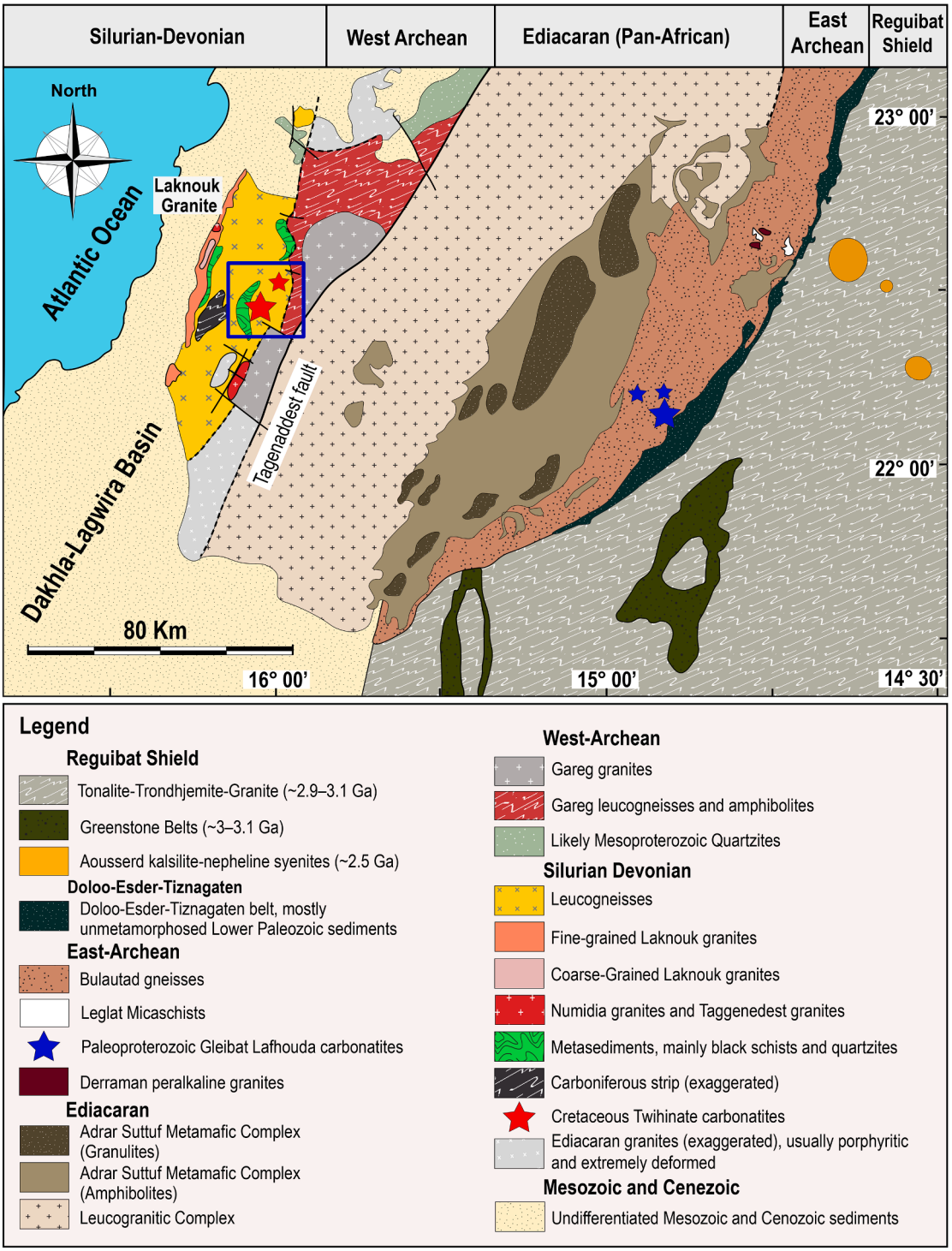

Fig. 2. Geological map of the Oulad Dlim massif of Moroccan Sahara at the NW Western African Craton margin outlining the main lithotectonic terranes. Adapted and modified from (Bea et al., 2020). Also indicated is the location of the Twihinate carbonatite intrusion.

based mapping, trenching, and surface rock channel sampling complemented by drilling of 54 vertical to inclined boreholes resulted in delineation of a promising 2 × 4 km prospect referred to as the Twihinate prospect (Fig. 3). Based on the results of these combined geochemical and geophysical surveys, total mineral resources have been estimated at 584.5 Mt grading 0.4% Nb_2O_5, 0.7% REE, 272 ppm Ta_2O_5, 193 ppm U_3O_8, and 35% Fe_2O_3 (https://www.onhym.com). Proven reserves are estimated at 216.2 Mt grading 1.25% REE and 0.34% Nb_2O_5.

In this paper which is based on 15 years of regional field mapping and drilling along with detailed examination of core samples from five

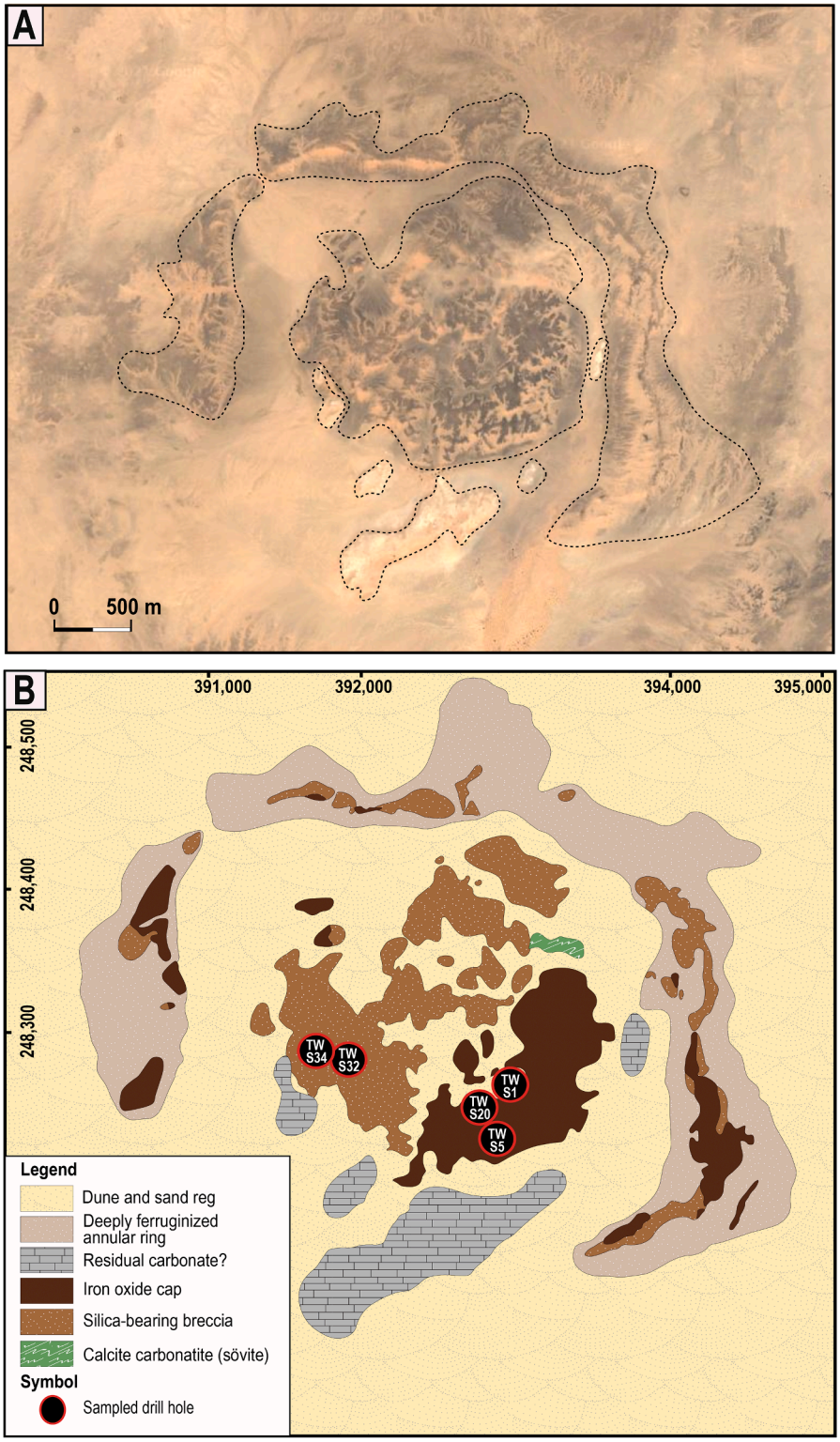

Fig. 3. Local geologic setting of the Twihinate carbonatite intrusion. (A) Google Earth picture showing the ring-shaped calcite carbonatite complex; (B) Simplified geological map of the Twihinate calcite carbonatite intrusion showing the main lithologies with sampled drill holes projected to surface (modified from ONHYM map). The references of drill holes mentioned in the text are indicated by filled black circles.

recently drilled exploration boreholes, we report the occurrence of an unusual carbonatite-related metasomatic paragenesis and related Nb-P-Fe ± LREE ± U-Th mineralization for which the term antiskarn is referred to. We provide detailed description on petrography, mineralogy and paragenetic succession of these unique calc-silicate-bearing carbonatite rocks. Also included are the whole-rock geochemistry and calc-silicate mineral chemistry of the antiskarn and ore-related phases to understand key processes involved in their formation. We show that the resulting calc-silicate paragenesis and related Nb-P-Fe ± LREE ± U-Th-rich mineralization formed at shallow crustal depths as the result of silica assimilation from the surrounding granitic host rocks at magmatic conditions. In view of exploration, this finding puts new directives on the ongoing drilling campaign for regional strategic metal exploration.

2. Regional and local geological settings

The *peri*-cratonic Oulad Dlim massif (Lat. 21°24′ to 23°30′N, Long. 14°36′ to 16°18′W) constitutes the northern termination of the Carboniferous Mauritanide foreland fold-and-thrust belt (Sougy, 1962) that overrides the western margin of the Archean Reguibat Shield of the WAC (Fig. 1). Current understanding of the geological setting of the massif is largely based on recent K-Ar, ^{40}Ar-^{39}Ar, and U-Pb geochronological studies of Villeneuve et al. (2006), Gärtner et al. (2013, 2016), Montero et al. (2014, 2016), and Bea et al. (2016, 2020). Controversy continues, however, on the evolution and geodynamic setting of the massif. In this respect, two contrasting geodynamic models have been proposed arguing for collision and subsequent westward thrusting of a series of Variscan tectonic nappes (Sougy and Bronner, 1969; Lécorché et al., 1991), or for units separated by sutures and thrust faults (Villeneuve et al., 2006, 2015; Michard et al., 2010; Gärtner et al., 2013, 2016). In opposite of these geodynamic models, other geologists (e.g., geochronological map of Bea et al., 2020) advocate that the terranes constituting the Oulad Dlim massif formed on the northwestern margin of the Reguibat Shield by fragmentation and subsequent formation of a NNE-trending Ediacaran (Pan-African) intracontinental rift and its filling during Silurian-Devonian time.

Available geochronological data indicate that magmatic activity occurred from 3160 ± 6 Ma to 271 ± 3 Ma, with two main peaks evident in the late Neoproterozoic to Cambrian, and in the Devonian. The youngest magmatic event is represented by the Twihinate carbonatite complex described therein whose emplacement is assigned to the Middle Cretaceous *peri*-Atlantic Alkaline Pulse (e.g., Matton and Jébrak, 2014; Montero et al., 2016). The oldest igneous rocks are the highly metamorphosed 2.9–3.1 Ga tonalite-trondhjemite-granodioritic (TTG) intrusions of the Aghaylas gneiss-migmatitic complex (Rjimati and Zemmouri, 2002; Bea et al., 2013; Montero et al., 2014) locally intruded by the 2.46 Ga Awsard kalsilite–nepheline syenite complex (Bea et al., 2013, 2014; Haissen et al., 2018), all of which being located adjacent to the Archean TTG rocks of the Reguibat Shield of the WAC (Bea et al., 2016; Montero et al., 2014). Later yet undated NNW- to NNE-trending, subalkaline tholeiitic mafic dyke and sill swarms were also reported (Villeneuve et al., 2015). To the north and west, the Oulad Dlim massif disappears under the Cretaceous and Cenozoic sediments of the Dakhla-Lagwira basin (Fig. 2). Structural features are attributed mainly to Pan-African and Variscan thin-skinned deformation (Lécorché et al., 1991; Villeneuve et al., 2015). Regional metamorphism is poorly constrained and heterogeneously developed; products range in facies from granulite- to eclogite to sub-greenschist (e.g., Molina et al., 2018).

The studied Twihinate carbonatite complex and related strategic metal-bearing mineralization (Fig. 2) is hosted within the central part of the Silurian-Devonian terrane (i.e., Oued Toghba unit of Villeneuve et al., 2006, 2015), approximately 260 km south of Dakhla city (Fig. 1). Stratigraphically, the oldest supracrustal sequences comprise an Archean high-grade metamorphosed granodioritic to leucogranitic gneissic protolith dated at 2913 ± 9 Ma (Villeneuve et al. 2015) locally intruded by hypabyssal post-Archean granitic intrusions of Ediacaran age (627–601 Ma, Bea et al., 2020). Less extensive series include metasedimentary sequences of amphibolites, micaschists, conglomerates, sandstones and quartzites. Collectively, all these supracrustal rocks were intensely deformed and hydrothermally altered, producing mylonitic corridors within the host rocks. Unconformably overlying the above-mentioned supracrustal rocks are the ca. 421 ± 3 Ma to 410 ± 2 Ma (SHRIMP zircon U-Pb dating; Montero et al., 2016; Bea et al., 2020) subduction-related gneissic to mylonitic peraluminous granitoids of the Laknouk suite whose emplacement seems to have exerted a strong control on the genesis of the Twihinate antiskarn and related strategic-bearing mineralization, as shown below.

3. The Twihinate carbonatite: field occurrence, petrography, and textural relationships

The Twihinate intrusion occurs as a well-defined, ~5-km-wide, ring-shaped structure that is clearly visible on satellite imagery (Fig. 3A) and aeromagnetic data interpretation. The magnetic anomalies show internal compositional variations with magnetic annular ring around a central, less magnetic plug of carbonatite. A recent U-Pb geochronological study of zircon from the carbonatite yielded an age of 104 ± 4 Ma (Montero et al., 2016). Surface mapping confirm the ring-like structure of the Twihinate intrusion (Fig. 3B). On surface, the carbonatite is poorly exposed, deeply weathered and so oxidized (Fig. 4A) that recognition of the original mineralogical and textural features is challenging except in few limited good rock exposures where the primary signature of the protolith is still preserved (Fig. 4B). When it is fresh, the core of the intrusion occurs as small sparse outcrops of brecciated medium- to coarse-grained mostly white to gray carbonatite (Fig. 3C, 4B). Conversely, strongly oxidized siliceous vuggy breccias and associated hydrothermal mineralization ring the carbonatite core (Fig. 3B). The contact between these two main units is not observable being covered by mobile sand and gravel. Unlike most carbonatite intrusions worldwide (Woolley and Church, 2005), the Twihinate intrusion does not show any obvious spatial connection with coeval alkaline igneous rocks. Throughout the Twihinate intrusion, dispersed mafic (Fig. 4C) to felsic (Fig. 4D) xenoliths and xenocrystic phases (Fig. 4E) are found sporadically occurring as partially to completely resorbed exotic fragments from the wall-rocks. Most of the enclaves have a dark-colored appearance, are either lenticular or ovoid in shape with size up to 1 m, show fine- to medium-grained texture, and tend to display sharp contact with the enclosing carbonatite. More importantly, some microgranular enclaves provide evidence for thermal and chemical interactions with their surrounding carbonatite. In this case, the resulting reaction structures consist either of a distinct bleached zone of silica and K-feldspar (Fig. 4C), greenish rim of diopside and chlorite pseudomorphs (Fig. 4D), or growth of grain-boundary coronae of tens of microns thick around biotite xenocrysts (Fig. 4E). Of particular interest is the observation that the Twihinate intrusion is texturally foliated and compositionally layered with dm to cm-thick bands and lenses of greenish silicate-rich rocks alternating with, or enclosed within, whitish carbonate-rich counterparts (Fig. 4F). The carbonate bands consist predominantly of calcite with subordinate apatite, pyrochlore, and magnetite whereas the interlayered silicate rocks are dominated by clinopyroxene and garnet with varying amounts of micas (biotite/phlogopite), titanite and chlorite depending on the silicate domain with which they are interlayered. Similar banded-textured carbonatite and related silicate-counterparts have been described in the Jacupiranga alkaline–carbonatite complex of southern Brazil (Chmyz et al., 2022), and in carbonatite of the Sung Valley ultramafic-alkaline-carbonatite complex of northeastern India (Pdah and Khonglah, 2022).

Mineralogically, the Twihinate carbonatite is exclusively calcitic (hereafter referred to as calcite carbonatite or sövite) and display textures varying from purely magmatic (Fig. 5A) to various stages of carbonatite wall-rock interaction (i.e., crustal assimilation, Fig. 5B, C). Original magmatic textures are obscured by the effects of both the

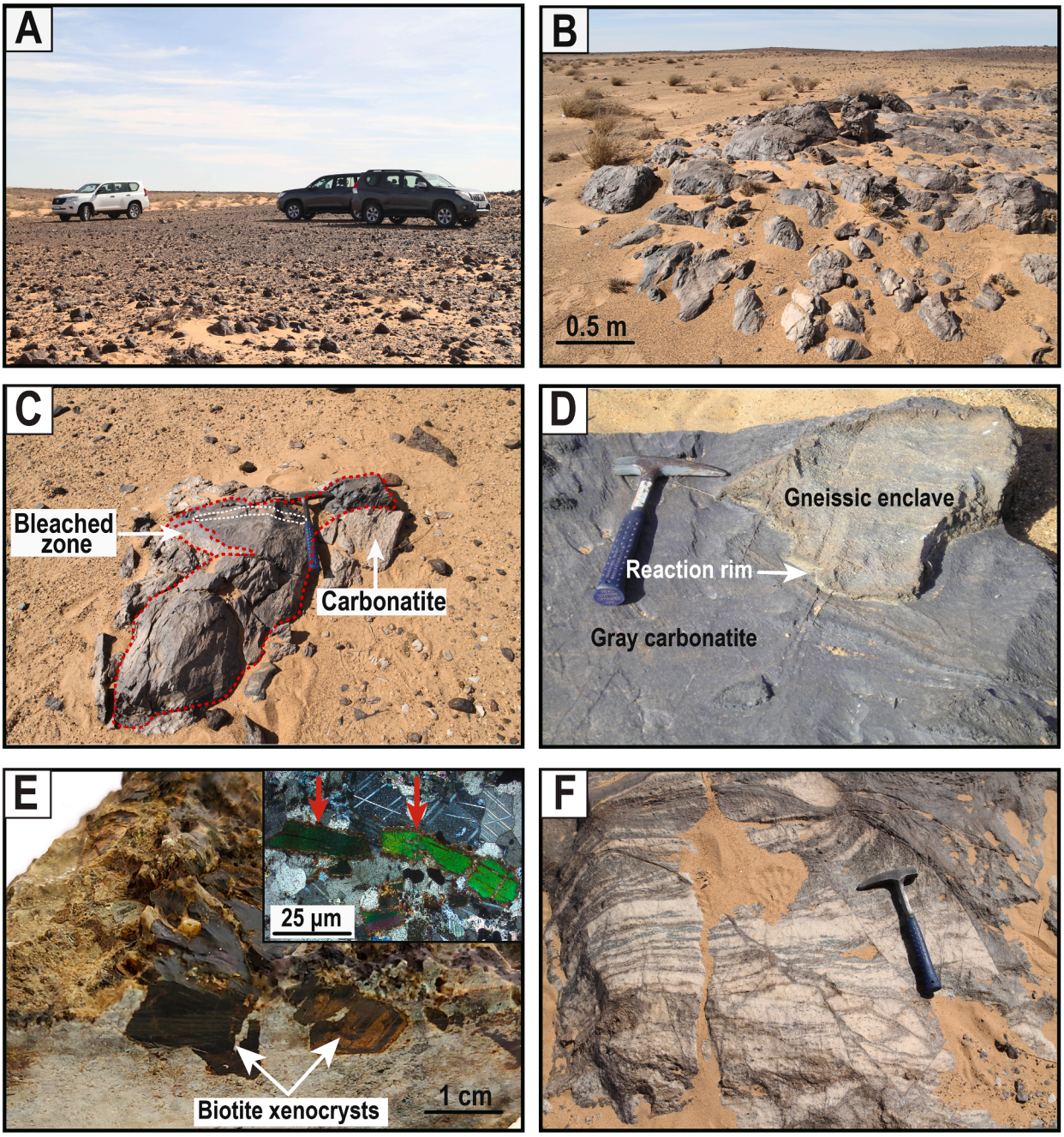

Fig. 4. Representative field photographs showing the mode of occurrence of the Twihinate carbonatite and associated enclaves and xenocrysts. (A) Panoramic view of the carbonatite intrusion showing the strongly oxidized dark boulders that overly the hidden carbonatites; (B) Close view of field exposure showing the morphology of the poorly outcropping brecciated carbonatite; (C) Wall-rock mafic microgranular enclave embedded into the carbonatite. The enclave is rounded and embayed indicating resorption during the magmatic stage; (D) Close up of carbonatite hosting a partially digested enclave of Precambrian gneiss with the contact zone (white arrow) being outlined by a greenish reaction rim made of clinopyroxene and chlorite; (E) Representative hand sample of carbonatite showing the occurrence of cm-sized phlogopite-biotite xenocrysts. The inset fossilizes a cross-polarized microscopic view of a large recrystallized biotite xenocryst mantled by a well-developed outer dark reaction coronae as indicated by the red arrows. This latter is interpreted as resulting from decomposition of biotite driven by heating or melt-fluid influx; (F) Close up of a banded-textured carbonatite showing alternation of whitish carbonate-rich and greenish silicate-rich layers. (For interpretation of the references to color in this figure legend, the reader is referred to the web version of this article.)

tectonic and subsequent multiple hydrothermal to surficial alteration events. Pervasive evidence of post-magmatic stress-related deformation include stretching, undulose extinction, grain-boundary migration, inequigranular foliated, alignment of elongate grains, and bent cleavage planes when cleavable minerals such as micas are involved. Nonetheless, the primary mineral paragenesis consists predominantly of >90 vol% anhedral calcite intergrown with subordinate apatite, monazite, pyrochlore, magnetite, strontianite, celestine, bastnäsite-(Ce), baryte and fluorite. Brecciated carbonatite exhibits a dark to yellowish-brown color with the matrix being formed by later hydrothermal to supergene minerals such as siderite, ankerite, goethite, hematite, and quartz.

4. Methodology, sampling and analytical methods

As surface outcrop is poorly exposed and intensively weathered, the

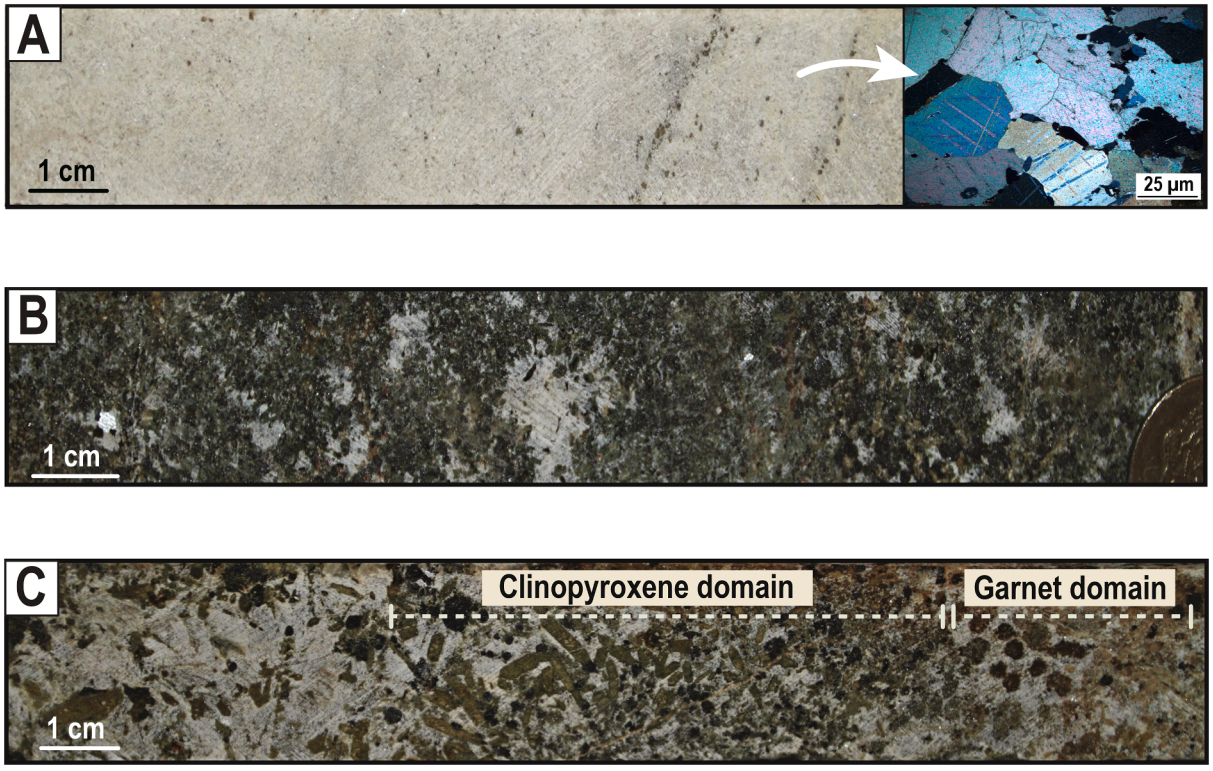

Fig. 5. Representative drill core photographs showing variable degrees of metasomatic contamination (i.e., assimilation) of the Twihinate carbonatites. (A) Fresh drill core of carbonatite with the inset (right corner) showing a microscopic view illustrating the isogranular-textured sövite; (B) Pervasive metasomatic contamination affecting the calcite carbonatite; (C) Close-up view showing the contact between the pyroxene-(left) and the garnet-dominated (right) domains.

current geologic investigation is based largely on exploration core samples drilled by ONHYM from 2007 to 2017. Weathering at Twihinate is deep, and fresh carbonatite was reached in all the examined boreholes at a depth of at least 50 m and deeper (Figs. 4, 5). Logged drill holes were therefore evaluated to get fresh samples and gain information from as much of the Twihinate intrusion as possible. In this respect, five drill holes 'TWS_1', 'TWS_5', 'TWS_{20}', 'TWS_{32}' and 'TWS_{34}' were made available by ONHYM and logged in detail (Fig. 3); three of which 'TWS_5', 'TWS_{20}' and 'TWS_{32}' served as the base for this study as they provided an overall picture of the different lithotypes of carbonatites and related metasomatic counterparts. Each of the >150 m-long drill holes intersected the carbonatite intrusion including the mineralized metasomatized lithotypes (Fig. 5A). Overall, a total of approximately 1,000-m was logged and systematically sampled. Of these, twenty core samples collected from drill hole 'TWS_5', and fifteen samples collected from 'TWS_{20}' were from depths of 60 to 140 m, and 50 to 260 m respectively. An additional 15 samples collected from drill hole 'TWS_{32}' were from depths of 62 to 130 m. All the representative core samples were selected for whole-rock geochemistry, microscopy and electron probe microanalyzer (EPMA) and laser ablation-inductively coupled plasma mass spectrometry (LA-ICP-MS) studies. Sample locations from drill holes are shown in Fig. 3.

Whole-rock analyses for a suite of fifty-seven major, minor and trace elements of drill core samples were determined at Activation Laboratory Ltd (Actlabs, Ancaster, ON, Canada) (http://www.actlabs.com) by Li metaborate/tetraborate fusion-inductively coupled plasma (FUS-ICP) for major elements, Li metaborate/tetraborate fusion-inductively coupled plasma-mass spectrometry (FUS-ICP/MS) for trace elements including the rare earth elements (REE), fusion-Ion Selective Electrode (FUS-ISE) for F, and Infrared spectroscopy for total S and total digestion-ICP-MS to refine Pb values.

Mineral identification, textural analysis and imaging were carried out using a petrographic microscope in both transmitted and reflected light on thin to thick (~30 µm) polished sections. Detailed textural analysis, back-scattered electron (BSE) imaging and corresponding SEM X-ray elemental maps along with mineral identification (based on energy-dispersive spectroscopy, or EDS, chemical analyses) were completed on carbon-coated thick sections using a HITACHI TM3000 scanning election microscope at "Plateforme analytique de la Faculté des Sciences d'Oujda" (Morocco) and Université du Québec à Montréal (Canada). The operating conditions were 15-kV accelerating voltage and 10-nA beam current.

EPMA analyses and element mapping of the major calc-silicate minerals and their associated ore-related phases were performed using a CAMECA SX-100 electron probe microanalyzer equipped with five wavelength-dispersive spectrometers (WDS) at Université Laval (Canada). The operating conditions were 15 kV accelerating voltage and a beam current of 20 nA, with variable counting times between 10 and 100 s and between 15 and 20 s in the peak and background, respectively. The beam diameter ranged from 1 to 5 µm and a ZAF matrix correction was applied during data reduction. Oxygen was calculated by stoichiometry and included in the data reduction, as was the correction for oxygen equivalence of the halogens (F and Cl). The calibration of the instrument was achieved using a range of natural and synthetic minerals, including Kα peaks for quartz (Si), hematite (Fe), orthoclase (K), plagioclase (Al), olivine (Mg), diopside (Ca), rutile (Ti), chromite (Cr), rhodochrosite (Mn), albite (Na), and apatite (P). The measurement of F and Cl contents in apatite could be problematic owing to the anisotropic diffusion of halogens during analyses (e.g., Stormer et al., 1993; Goldoff et al., 2012; Li et al., 2020). In order to overcome such constraints and consequently improve the analytical accuracy, a strict analytical protocol has been followed by using relatively short (20 s) peak count times for all elements, a 15 kV accelerating voltage and a 15 nA defocused (5 µm) beam, with F, Cl and P being analyzed first. For coarse-grained apatite, halogen analyses were conducted perpendicular to the c-axis of the crystal (e.g., Stormer et al., 1993; Goldoff et al., 2012; Li et al.,

2020).

The in-situ determination of trace elements in magnetite was performed on polished thin sections via a laser ablation system coupled to a mass spectrometer (LA-ICP-MS) at the LabMaTer laboratory of the Université du Québec à Chicoutimi (UQAC, Canada). The following elements were analyzed: ^{23}Na, ^{25}Mg, ^{27}Al, ^{29}Si, ^{39}K, ^{44}Ca, ^{45}Sc, ^{49}Ti, ^{51}V, ^{52}Cr, ^{55}Mn, ^{57}Fe, ^{59}Co, ^{60}Ni, ^{65}Cu, ^{66}Zn, ^{71}Ga, ^{74}Ge, ^{88}Sr, ^{89}Y, ^{90}Zr, ^{93}Nb, ^{95}Mo, ^{118}Sn, ^{139}La, ^{140}Ce, ^{141}Pr, ^{146}Nd, ^{153}Eu, ^{157}Gd, ^{159}Tb, ^{163}Dy, ^{165}Ho, ^{166}Er, ^{169}Tm, ^{172}Yb, ^{175}Lu, ^{178}Hf, ^{181}Ta, ^{182}W, ^{208}Pb, ^{232}Th and ^{238}U based on the method from Dare et al. (2014). The LA-ICP-MS system used is Resonetics RESOlution M-50 Excimer 193 nm laser equipped with a S155 ablation cell (Laurin Technic) coupled to an Agilent 7900 Model ICP-MS. The analyses were performed with 30 s of background acquisition to define the blank following by 20 s of sample data acquisition. A spot size dependent of the mineral grain size and ranged between 25 and 33 μm was used with a frequency of 15 Hz and an energy density of 3 J/cm^2. The USGS certified reference material GSE-1 g, a synthetic glass containing 10% Fe and doped with approximately 500 ppm of each trace element was used for instrument and mass calibration. Three reference materials were used for external calibration: BC28 (natural Ti-rich magnetite derived from the Bushveld complex; Dare et al., 2012), GSD-1 g (synthetic basalt glass), and Gprob6 (matrix artificial basalt glass). Material analyses were performed before each scan cycle to correct the deviation and calibrate the equipment. The results obtained are in good agreement with the working values. Si, Ca, V and Ti were monitored to ensure that the measured signal was pure magnetite. All acquired data was then reduced using the Iolite software (Paton et al., 2011).

5. Antiskarn textural characteristics, mineralogy and paragenesis

From careful examination of the logged drill cores, a red-brown to olive-green metasomatic banding (Fig. 4F) is developed within the sövite generally from a depth of ~50 to >260 m. This interval coincides with development of calc-silicate package of metasomatic rocks commonly displaying interlayering of greenish pyroxene-dominated and reddish-brown garnet individual bands (Fig. 5C). A macroscopic zonation is also evident to the naked eye, which grades downward from fresh white sövite precursor (Fig. 5A) into a metasomatized olive-green colored rock (Fig. 5B, C). At this stage of exploration, it is difficult to estimate the thickness and lateral extension of these metasomatic rocks and related mineralization. In this respect, it should be stressed that of the five examined drill holes, metasomatic lithotypes were intersected only in drill holes TWS_5 and TWS_{20} (Fig. 6). Where it does exist, the metasomatic horizons and related mineralization occur within the sövite either as E-W-oriented continuous layers or discontinuous patches up to 120 m thick and could be traced vertically for >100 m from its apex near depth 50 m down to 200 m, where it remains open in all directions. Supergene alteration is widely developed in the upper part of the examined drill interceptions and occurs as pulverulent halos of iron oxides and hydroxides (regolith) overlying the sövite (Fig. 6).

Mineralogically and texturally, the examined metasomatic rocks consist of a succession of calc-silicate layers (Fig. 4F) exhibiting mineralogical zonation with, from the paragenetically early to late phases, clinopyroxene (Fig. 7A), garnet (Fig. 7B), micas (Fig. 7C) and titanite (Fig. 7D) set in a matrix of igneous calcite; all of which having precipitated within the sövite intrusion itself close to the contact with the felsic country rocks. Subordinately, significant amounts of Nb-P-Fe ± LREE ± U-Th-bearing phases occur in intimate association with the calc-silicate sequence. Clinopyroxene occurs either as single 100 to 500 μm-sized pale green locally patchy-colored euhedral to subhedral crystals (Fig. 7A) or alternatively coexists with poikilitic garnet and micas (Fig. 7B). The mica group minerals occur as randomly oriented, poikilitic, up to 2-mm across subhedral to euhedral light green to dark brown pleochroic laths commonly associated with apatite, garnet, clinopyroxene and titanite. Most of the mica crystals contain numerous minute (<15 μm across) inclusions of apatite, monazite, and magnetite (Fig. 7C), and are strongly pleochroic with the corresponding colour changing from a yellow to light brown (phlogopite) to a dark reddish brown (biotite). Titanite is commonly dispersed within the antiskarn rocks. In a few drill intersections, titanite occurs either as individual <30 μm-sized anhedral to euhedral crystals enclosed in igneous calcite or as vermicular (i.e., symplectitic-like texture) to radiating intergrowths within apatite-rich zones (Fig. 7D). Moreover, the antiskarn event is overprinted by late-stage low-temperature mineral assemblages which consist of various proportions of chlorite, epidotes, magnetite/hematite, sulfides, kaolinite, quartz (or chalcedony), carbonates, fluorite, and baryte. Of these, chlorite, epidotes and carbonates are the most abundant and locally comprise 10 to 20 vol%, occurring between garnet crystals as 100- to 500-μm euhedral grains, and/or as pseudomorphs of clinopyroxene and micas. Late coarse-grained, anhedral to euhedral hydrothermal calcite and dolomite grains are cut and rimmed by finer grained manganoan calcite, ferroan dolomite, or siderite and ankerite crystals. A summary of the idealized paragenetic sequence is shown in Fig. 8.

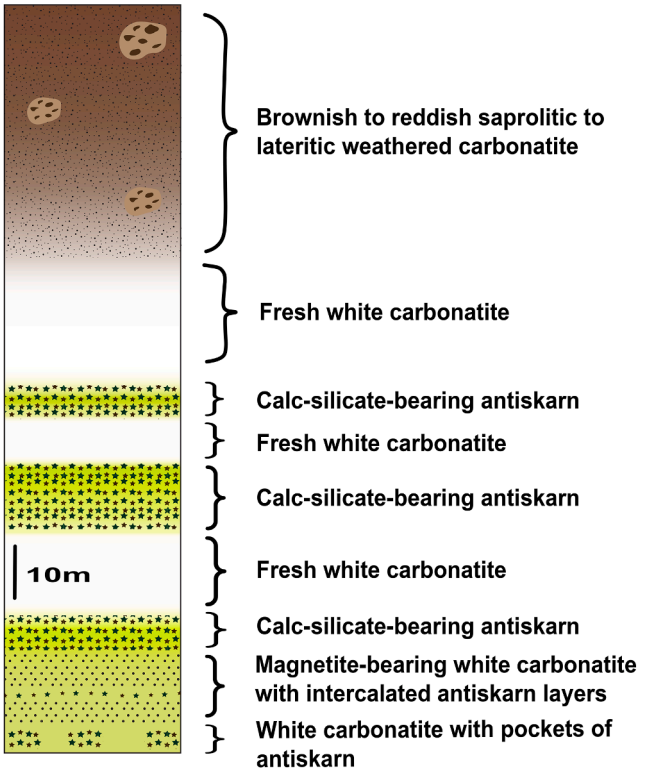

Fig. 6. Detailed core log of the exploration drill hole TWS_5 in the Twihinate prospect. Green horizons indicate the emplacement of the antiskarn rocks and sampling depths. (For interpretation of the references to color in this figure legend, the reader is referred to the web version of this article.)

Based on their petrographic and mineralogical attributes along with their similarity to the experimentally produced and naturally occurring metasomatic rocks genetically related to the reaction of carbonatite melt with surrounding silicate wall-rocks (e.g., Anenburg and Mavrogenes, 2018; Yaxley et al., 2022; Chmyz et al., 2022; Pdah and Khonglah, 2022; Walter et al., 2022), the above described metasomatic calc-silicate-bearing carbonatite lithotypes are recognized as sensu lato antiskarns (see below).

6. Nb-P-Fe ± LREE ± U ± Th mineralization and ore mineralogy

The Nb-P-Fe ± LREE ± U-Th-rich mineralization occurs either as

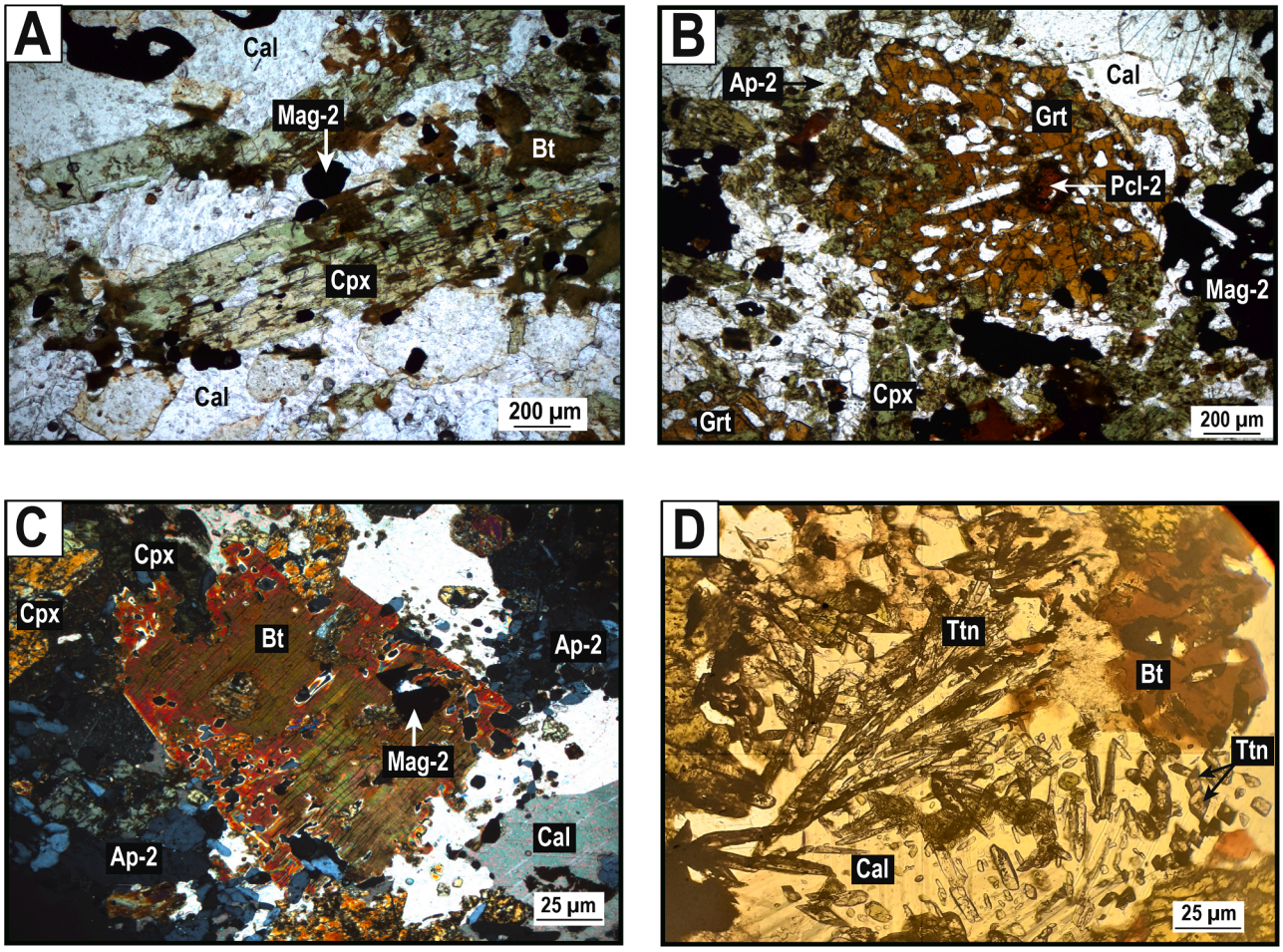

Fig. 7. Illustrative microscopic plane- and cross-polarized photomicrographs showing the calc-silicate paragenesis from the Twihinate antiskarn. (A) Clinopyroxene-dominated sample showing aggregates of euhedral clinopyroxene crystals and associated pyrochlore and magnetite grains; (B) Poikilitic euhedral garnet phenocryst containing pyrochlore, magnetite and apatite inclusions in set in the metasomatized calcite carbonatite; (C) Poikilitic biotite lath containing apatite and monazite with visible metamict halos; (D) Symplectite-textured titanite in biotite-bearing antiskarn rock.

fine- to medium-grained disseminations, and grouped clusters set in a matrix of calcite and associated calc-silicate phases or as cements to breccias, and to a lesser extent as infills of stringers, veinlets, and stockworks in the sövite. The bulk of mineralization is related to the antiskarn lithotypes and closely correlates with the distribution of calc-silicate phases. Over 30 ore and gangue minerals were identified at Twihinate prospect (Fig. 8). Ore minerals consists of various proportions of Fe-oxides (i.e., titanomagnetite principally) and phosphates (apatite, monazite-(Ce)), pyrochlore group minerals, REE-fluorcarbonates (mainly bastnäsite-(Ce)), sulfides (sphalerite, chalcopyrite, and galena), and various assemblages of strontianite, celestine, baryte and fluorite. Major mineral assemblages include (1) apatite-monazite + magnetite + pyrochlore + garnet + calcite, (2) pyrochlore + apatite + calcite + aegirine-augite + micas (biotite/phlogopite), and (3) garnet + micas (biotite/phlogopite) + titanite + magnetite + pyrochlore + sulfides + sulfates.

Magnetite is by far the main iron ore, displaying a variety of textures ranging from sparse crystals of diverse size dispersed within the sövite (Fig. 9A) to random clusters (Fig. 9B) where magnetite is intimately associated with apatite and in textural equilibrium with all the calc-silicate phases. Three generations of magnetite referred to as Mag-1, Mag-2 and Mag-3 are identified (Fig. 8). Collectively, magnetite grains are homogenous and unzoned containing locally sulfide inclusions or more rarely ilmenite exsolution lamellae. Mag-1 is commonly intergrown with primary calcite as interstitial subhedral to euhedral crystals ranging in size from 200 µm up to several cm across, and hence is interpreted as of early-stage orthomagmatic origin. In the antiskarn rocks, Mag-2 occurs as dispersed to clustered subhedral crystals in common association with apatite, garnet, clinopyroxene, and micas (biotite/phlogopite). Mag-3 is related to the late hydrothermal stage occurring as anhedral inclusions within amphibole, chlorite, and epidotes.

In conjunction with magnetite, pyrochlore-group minerals consist of multiple generations with pervasive overgrowth textures, and occur in all examinated samples as euhedral cubo-octahedral and octahedral crystals ranging from honey-yellow to dark brown in color, and from a few tens of µm to 5 mm across (Fig. 9C, D). These minerals are commonly intergrown with both the earlier orthomagmatic and subsequent antiskarn stage along with the late hydrothermal and supergene events. The earliest pyrochlore generation is restricted to the fresh sövite, and is commonly intergrown with apatite and magnetite-1 (Fig. 9C). In comparison with Pcl-1, the antiskarn-related pyrochlore referred to as Pcl-2 occurs in close spatial and temporal relationship with the calc-silicate phases (Fig. 9D). Conversely, Pcl-3 is largely restricted to weathered samples and probably formed under supergene conditions as inferred from its compositions (see below).

Apatite is a ubiquitous constituent of the examined samples, locally gaining the status of a major rock-forming mineral where it constitutes up to 50 vol% of the antiskarn. When it exists, apatite occurs as partially resorbed and disaggregated prismatic crystals and, less commonly, as clusters of radiating prisms or as vein-like clusters (Fig. 9E) and aggregates closely associated with magnetite and pyrochlore. Based on their

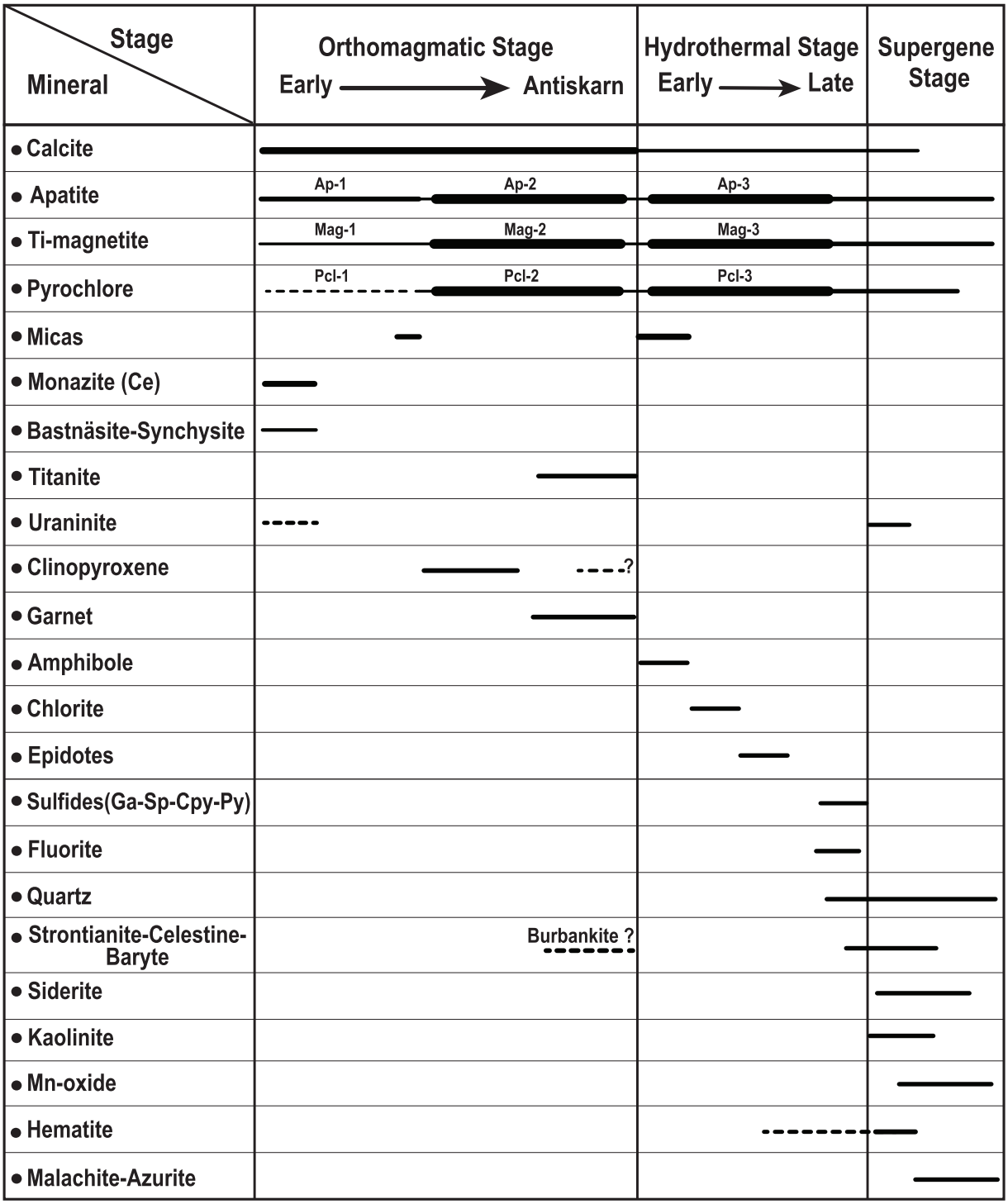

Fig. 8. Summary of the idealized paragenetic sequence identified at Twihinate Nb-P-Fe ± LREE ± U-Th-rich prospect illustrating the paragenetic position of the antiskarn metasomatic event and related mineralization. Bar thickness represents schematically the relative abundance of precipitated minerals. Dotted lines indicate uncertainties.

compositions and textures, three stages of apatite formation are also recognized, comprising an early orthomagmatic apatite (Ap-1), followed by two successive apatite generations referred to as antiskarn Ap-2 and late-stage hydrothermal Ap-3 (Fig. 8). Notably, Ap-1 occurs as anhedral to euhedral poikilitic crystals (typically <50 μm) containing ubiquitous ovoid to prismatic inclusions of monazite whose presence was confirmed by micro-Raman spectroscopy. Texturally, Ap-1 and Ap-2 host inclusions of magmatic calcite and vice versa, indicating these minerals are cogenetic. In contrast, Ap-3 is clearly epigenetic as it occurs as structurally controlled late-stage infills of fractures (Fig. 9E), veinlets and stockworks, as matrix in brecciated zones, or as aggregates of acicular apatite crystals commonly associated with magnetite, and to a lesser degree pyrochlore. Of note, Ap-3 is texturally devoid of monazite inclusions. Equivalent mineralogic and textural features have been documented in the Nolans Bore Mesoproterozoic P-REE-Th ore deposit of the Northern Territory of Australia (Anenburg et al., 2020a) as well as in the Canadian Hoidas Lake deposit in Saskatchewan (Pandur et al. 2015, 2016).

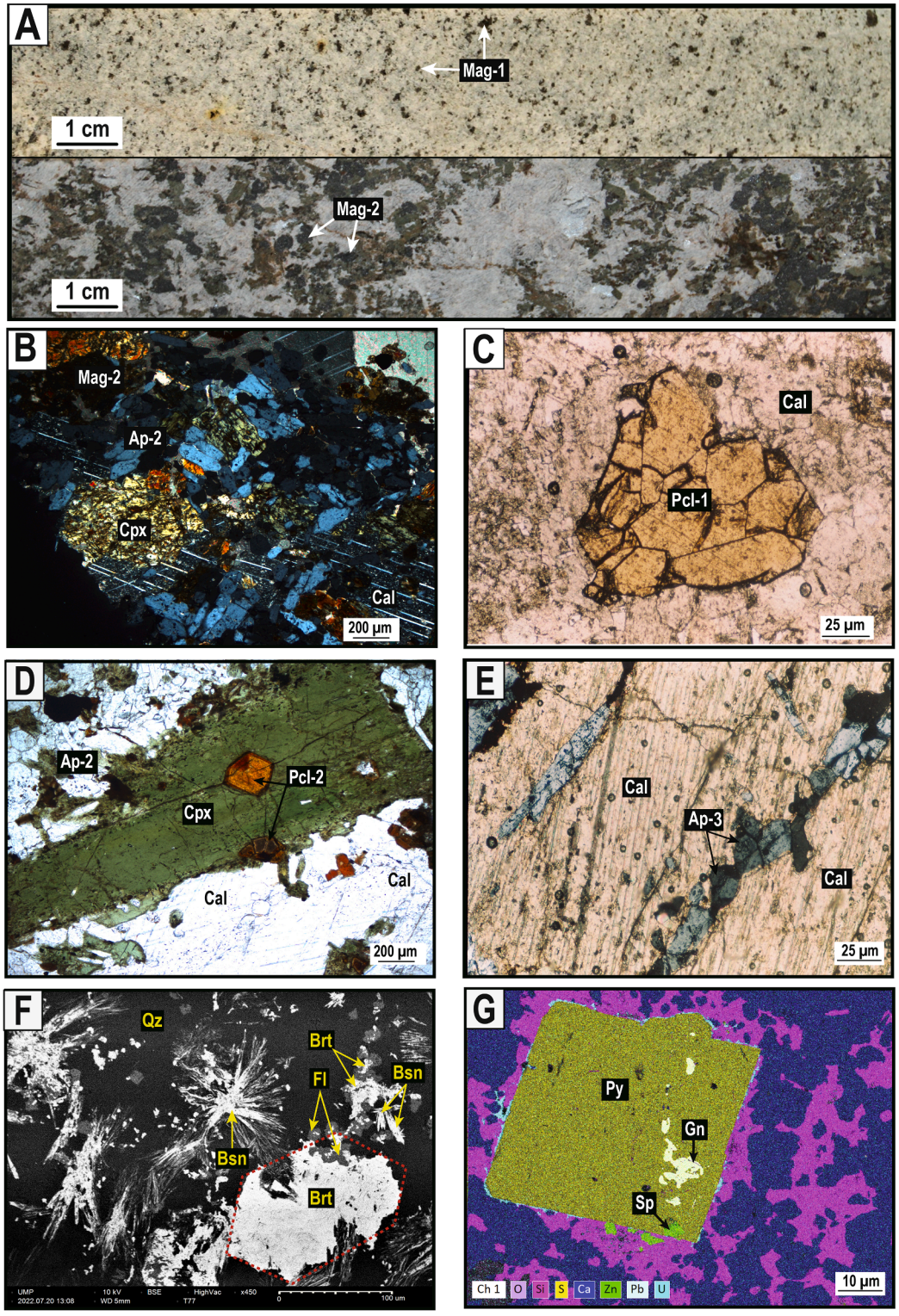

Fig. 9. Representative photographs of exploration drill core slabs of TWS_5 borehole and petrographic photomicrographs highlighting the mineralogy of the Twihinate antiskarn and related Nb-P-Fe ± LREE ± U-Th mineralization. (A) Photographs of exploration drill core slabs of TWS_5 borehole showing the occurrence of disseminated magnetite grains in fresh sövite (top slab) and pyroxene-dominated antiskarn (bottom slab). Although both rock types are similar with respect to carbonate components, the antiskarn sample is characterised by a high proportion of silicates (pyroxene) and associated iron mineralization typified by the widespread development of magnetite-2; (B) Cluster of clinopyroxene, apatite, and magnetite assemblage set in a matrix of igneous calcite (i.e., sövite); (C) Euhedral magmatic pyrochlore crystal set in a matrix of igneous calcite (i.e., sövite); (D) Clinopyroxene-dominated sample showing clinopyroxene phenocryst hosting pyrochlore; (E) Close-up view of carbonatite showing shear fracturing and rock cleavage and subsequent infills of phosphate mineralization typified by apatite grains along healed fracture planes; (F) Back scatter electron micrograph showing pseudomorphs of baryte-fluorite-bastnäsite-(Ce) after a dihexagonal prismatic crystal, interpreted as former burbankite; (G) Late-stage uraninite overgrowths around pyrite and corresponding elemental map of S, Pb and Zn in counts per seconds. Note also the occurrence of galena and sphalerite as inclusions within the host pyrite.

Monazite, the main LREE-bearing mineral, occurs either as up to 30 μm-sized euhedral to subhedral crystals enclosed in or along fluorapatite rims and fractures, or as aggregates disseminated in calcite. Bastnäsite-(Ce), the principal and most abundant REE-bearing mineral, is observed as radiating clusters of euhedral prismatic crystals (Fig. 9F), and is commonly intergrown with quartz, fluorite and baryte. Uraninite is a scarce phase of the mineral assemblages. Where it exists, uraninite is commonly fine-grained (typically <10 μm in length), and occurs as euhedral phase enclosed in major rock-forming minerals. Uraninite has also been depicted as a late overgrowth phase rimming the margins of sulfide grains (Fig. 9G). Metamict halos of several tens of microns in width around uraninite grains are commonly observed. These radiation-induced destruction rims which resulted from the combined effects of metamictization and metasomatism are associated with secondary minerals such as U-rich silicates (probably coffinite) and unidentified Ca-Fe-U-bearing aluminosilicate (probably clay minerals) closely associated with goethite. Sulfides formed in the late hydrothermal stage with abundant pyrite chalcopyrite, sphalerite, galena, and pyrrhotite (Fig. 9G). Typically, sulfides occur together with fluorite, baryte, bastnäsite-(Ce), and quartz in irregularly distributed clusters or stringers and veinlet infills or as disseminated grains within the calcite carbonatite overprinting earlier igneous and antiskarn paragenesis. The fluorite and baryte are present invariably in subordinate amounts interstitial to garnet-pyroxene, and as late fracture fillings.

7. Antiskarn lithogeochemistry

The three antiskarn samples display a significant proportion of SiO_2 (7–17 wt%), CaO (25–42 wt%), and Al_2O_3 (1–2 wt%) in conjunction with elevated loss on ignition (12–26 wt%). Such high loss reflects an abundance of volatile-rich phases (CO_2 and H_2O) such as phlogopite, chlorite, and carbonates in these rocks. A summary of major and trace element whole-rock compositions is presented in Table 1 and displayed in Fig. 10.

In comparison with the trace element abundances of carbonatites, the antiskarn lithotypes are characterized by slightly higher concentrations, but overlap to larger degrees with the carbonatite rocks (Fig. 10). Strontium and Rb concentrations range from 3125 to 7018 ppm, and 8 to 37 ppm, respectively. Conversely, Th and U, and more importantly Nb and V concentrations are distinctly high ranging from 37 to 187 ppm, 10 to 787 ppm, 140 to >1000 ppm, and 603 to 1008 ppm, respectively (Table 1). Base metals such as Pb (31–93 ppm) and Zn (190–490 ppm) as well as Ga (14–41 ppm) are present at noticeable levels. The ΣREE + Y concentrations are similar to those of carbonatite, ranging from 1087 to 1607 ppm, with a mean value of 1327 ± 262 ppm (Table 1). Chondrite-normalized trace element patterns show enrichment in large ion lithophile elements (LILE) and LREE relative to HREE, and strong to moderate negative anomalies in Rb, K, P, Zr, Hf and Ti (Fig. 10), and characteristically lack a Eu anomaly. Of particular note is the perfect match between the chondrite-normalized multielement patterns of antiskarn rocks and those of carbonatites (Fig. 10).

Table 1
Representative major (wt.%) and trace element (ppm) concentrations of Twihinate antiskarn (West African Craton Margin, Moroccan Sahara).

Borehole No.	TWS5	TWS20	TWS20
Sample No.	TW8	TN8	TN19
Depth (m)	82	186	240
Major elements (wt %)			
SiO_2	11.18	16.74	6.78
Al_2O_3	0.75	1.29	1.75
Fe_2O_3	11.18	24.23	31.33
MnO	0.38	0.489	0.614
MgO	1.99	2.84	1.31
CaO	42.25	24.93	28.92
Na_2O	0.68	1.65	0.21
K_2O	0.25	1.11	0.44
TiO_2	0.3	0.776	1.363
P_2O_5	3.44	6.17	3.61
LOI	26.28	11.95	21.71
Total	**98.68**	**92.17**	**96.78**
Trace element (ppm)			
LHFSE			
Cs	<0.5	0.70	2.00
Rb	8.00	37.00	21.00
Ba	393.00	1300.00	594.00
Sr	7018.00	3125.00	4189.00
HFSE			
Th	187.00	104.00	37.00
U	787.00	86.60	10.20
Nb	>1000	409.00	140.00
Ta	9.50	5.80	2.40
Pb	31.00	93.00	<5
Zr	704.00	150.00	491.00
Hf	1.90	0.90	0.40
Y	37.00	69.00	60.00
REE			
La	307.00	380.00	236.00
Ce	647.00	715.00	489.00
Pr	60.10	82.40	56.20
Nd	202.00	300.00	211.00
Sm	27.60	47.50	33.50
Eu	7.66	12.70	9.41
Gd	17.10	31.20	23.30
Tb	1.80	3.90	2.90
Dy	7.90	18.30	14.00
Ho	1.20	3.00	2.20
Er	3.00	6.60	5.00
Tm	0.41	0.81	0.61
Yb	2.40	4.70	3.60
Lu	0.34	0.72	0.52
∑REE	**1285.51**	**1606.83**	**1087.24**
TM			
Cr	<20	<20	<20
Co	6.00	27.00	8.00
Ni	<20	<20	<20
V	603.00	1008.00	985.00
Sc	<1	<1	<1
Cu	<10	<10	10.00
Zn	190.00	380.00	490.00
Ga	14.00	32.00	41.00

8. Mineral chemistry of antiskarn and ore-related phases

The distribution of trace elements in calc-silicate minerals (clinopyroxene, garnet, micas) and ore-related phases such as magnetite, apatite and pyrochlore, coupled with textural relationships, provide powerful geochemical tool to discriminate between different ore deposit types, and to track back the origin and physico-chemical characteristics (temperature, f_{O2}) of fluids/melts responsible for metasomatism as they record the nature of melts and/or fluids from which these minerals saturate (e.g., Nadoll et al., 2014, and references therein). In this respect, in situ representative EPMA and LA-ICP-MS analyses of selected clinopyroxene, garnet, micas, and chlorite along with co-genetic magnetite, apatite and pyrochlore were performed to determine major, minor, and trace element concentrations. The results are summarized in Tables 2 to 8 and plotted in Figs. 11–15.

8.1. Clinopyroxene

Representative analyses are summarized in Table 2 and illustrated in Fig. 11A, B. Formula calculations are based on four cations and six oxygens. Compositionally, the EPMA analyses define an evolutionary trend from diopside (Di_{66-82} Hd_{18-34}) to aegirine-augite (Di_{38-55} Ae_{21-35}) compositions (Table 2, Fig. 11A, B) with low concentrations of Ti (<1.5 wt% TiO_2) and Al (0.3–1.7 wt% Al_2O_3) but significant Na contents (up to 4.17 wt% Na_2O). The Ni and Co contents are very low commonly below limit detection. These compositions are in line with the literature data

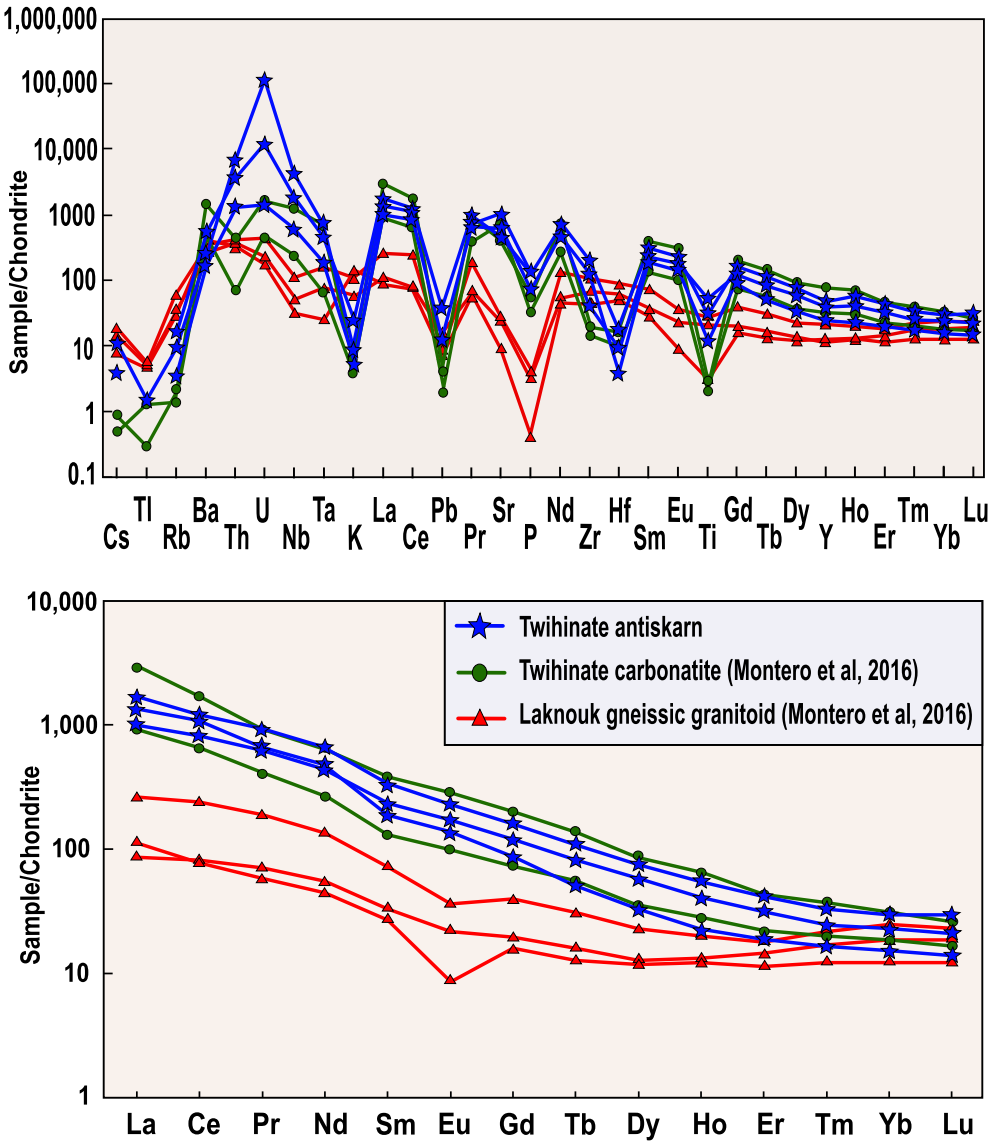

Fig. 10. Chondrite-normalized incompatible trace element (A) and REE (B) patterns of representative Twihinate antiskarn compositions compared to those of carbonatite and associated Laknouk gneissic granitoids (Montero et al., 2016). Normalizing values from McDonough and Sun (1995). Note the striking similarities between the carbonatite patterns and those for antiskarns.

(e.g., Giebel et al., 2019; Anenburg et al., 2020a; Chmyz et al., 2022).

8.2. Garnet

A total of 27 spot EPMA elemental analyses were carried out on selected garnet crystals. The obtained compositions are summarized in Table 3 and illustrated in Fig. 11C. These include both core and rim areas of crystals. Formula calculations are based on eight cations and twelve oxygens, using the calculation scheme of Locock (2008). The compositional variation in terms of the concentration of the major element oxides is SiO_2 (31.92–35.09 wt%), CaO (32.31–32.84 wt%), Al_2O_3 (0.82–2.38 wt%), FeO_T (22.64–25.88 wt%), with lower concentrations of TiO_2 (1.03–3.06 wt%), MnO (0.52–0.74 wt%), MgO (0.30–0.91 wt%), and Cr_2O_3 whose contents are commonly below limit detection. No significant compositional zoning in Ca, Si, and Al contents from the core to rim has been detected. Overall, garnets show consistently high andradite endmember compositions ($And_{86\text{-}94}$ $Gro_{1\text{-}9}$; Fig. 11C) with minor amounts of spessartine, pyrope, and almandine accounting for <15 mol % of the total (Table 3, Fig. 11C), and thus classified as andradite.

8.3. Micas and chlorite

Representative analyses of micas are given in Table 4 and illustrated in Fig. 11D. Formula calculations are based on an ideal trioctahedral mica formula ($XY_3[Z_4O_{10}][OH, F, Cl]_2$) and the data were normalized to 7 (tetrahedral [Z] plus octahedral [Y]) cations and 22 oxygens. Overall, micas from Twihinate antiskarn are characterized by a large spread in Fe/(Fe + Mg) values, thus defining two types of micas referred to as biotite (XFe = 0.32–0.52) (after Foster, 1960), and phlogopite (XFe = 0.11–0.15); both of which plot within the re-equilibrated biotite field of Nachit et al., (2005) (Fig. 11D). Conversely, chlorite indicate a Si- and Mg-enriched end-member (diabantite) with Mg/(Mg + Fe) ratio from 0.54 to 0.69 (Table 5; Fig. 11E). Formula calculations are based on 28 oxygens (with Fe^{2+}/Fe^{3+} and OH calculated assuming full site occupancy). The occurrence of diabantite in the Twihinate antiskarn rocks is one of the notable mineralogical attributes of these metasomatized lithotypes.

Table 2
Representative EPMA compositions of clinopyroxene from the Twihinate antiskarn (West African Craton Margin, Moroccan Sahara).

Sample		SiO_2	TiO_2	Al_2O_3	Cr_2O_3	FeO	MnO	MgO	CaO	Na_2O	NiO	CoO	Total	Si	Al^{IV}	Fe^{3+}	Σ	Al^{VI}	Fe^{3+}	Ti	Cr	Mg	Fe^{2+}	Mn	Ni	Co	Σ	Ca	Na	Σ	Q	Jd	Aeg	Di	Hed	Aeg	Nomenclature
TW9																																				
Z1 1a	1	52.35	0.07	0.44	b.d.	14.30	1.08	8.43	17.81	3.99	0.01	b.d.	98.49	1.991	0.009	-	2.0	0.010	0.282	0.002	-	0.478	0.173	0.035	0.000	-	1.0	0.726	0.294	1.0	70.05	1.06	28.89	47.79	20.75	29.42	Aeg-Aug
Z1 1b	2	52.90	0.07	0.33	b.d.	13.66	1.04	9.10	17.34	4.21	b.d.	b.d.	98.64	1.997	0.003	-	2.0	0.012	0.289	0.002	-	0.512	0.143	0.033	-	-	1.0	0.701	0.308	1.0	68.74	1.24	30.02	51.20	17.61	30.83	Aeg-Aug
Z1 2a	1	52.16	0.15	0.60	0.01	13.97	1.22	8.43	17.55	4.14	0.02	0.04	98.29	1.984	0.016	-	2.0	0.011	0.294	0.004	0.000	0.478	0.151	0.039	0.001	0.001	1.0	0.715	0.305	1.0	68.76	1.13	30.11	47.83	18.98	30.54	Aeg-Aug
Z1 2b	2	52.15	0.09	0.43	b.d.	14.52	1.18	8.28	17.56	3.97	0.00	0.02	98.21	1.992	0.009	-	2.0	0.011	0.279	0.003	-	0.471	0.184	0.038	-	0.001	1.0	0.719	0.294	1.0	70.02	1.14	28.85	47.12	22.24	29.42	Aeg-Aug
Z1 3		51.11	0.28	0.73	0.01	16.27	1.48	6.67	18.34	3.34	b.d.	0.02	98.25	1.982	0.018	-	2.0	0.016	0.232	0.008	0.000	0.386	0.296	0.049	-	0.001	1.0	0.762	0.251	1.0	74.19	1.64	24.17	38.56	34.46	25.12	Aeg-Aug
Z1 4		52.84	0.16	0.40	b.d.	14.23	0.98	8.70	17.05	4.50	b.d.	b.d.	98.85	1.991	0.009	-	2.0	0.009	0.312	0.005	-	0.489	0.137	0.031	-	-	1.0	0.688	0.329	1.0	66.64	0.95	32.41	48.85	16.78	32.87	Aeg-Aug
Z2 1	1	49.57	0.73	2.77	b.d.	9.96	0.92	10.85	23.49	0.90	b.d.	0.01	99.19	1.878	0.122	-	2.0	0.002	0.144	0.021	-	0.613	0.172	0.029	-	0.000	1.0	0.954	0.066	1.0	92.90	0.07	7.03	61.27	20.11	6.64	Di
Z2 2	2	51.03	0.49	1.61	0.02	9.48	1.25	11.31	23.96	0.71	b.d.	b.d.	99.85	1.922	0.072	0.006	2.0	-	0.100	0.014	0.001	0.635	0.192	0.040	-	-	1.0	0.967	0.052	1.0	94.56	0.00	5.44	63.50	23.15	5.16	Di
Z2 3	3	52.48	0.15	1.01	b.d.	6.99	0.87	13.10	24.73	0.46	b.d.	b.d.	99.78	1.957	0.043	-	2.0	0.001	0.066	0.004	-	0.728	0.152	0.027	-	-	1.0	0.988	0.033	1.0	96.59	0.06	3.35	72.84	17.91	3.30	Di
Z2 4		49.11	1.49	2.07	0.00	12.96	0.83	8.84	21.11	1.98	b.d.	b.d.	98.38	1.892	0.094	0.015	2.0	-	0.167	0.043	0.000	0.508	0.236	0.027	-	-	1.0	0.871	0.148	1.0	84.52	0.00	15.48	50.76	26.31	14.79	Di
Z3 1		51.70	0.11	0.69	b.d.	14.85	1.06	7.90	17.88	3.90	0.01	b.d.	98.08	1.981	0.019	-	2.0	0.012	0.284	0.003	-	0.451	0.192	0.034	0.000	-	1.0	0.734	0.290	1.0	70.40	1.19	28.40	45.11	22.64	28.95	Aeg-Aug
Z3 2		51.68	0.12	0.69	0.01	14.83	1.14	7.79	17.68	4.09	0.00	b.d.	98.03	1.979	0.021	-	2.0	0.010	0.299	0.004	0.000	0.445	0.176	0.037	0.000	-	1.0	0.726	0.304	1.0	68.92	1.03	30.06	44.47	21.29	30.36	Aeg-Aug
Z3 3	1	52.47	0.08	0.48	0.10	14.29	1.33	8.23	17.75	3.97	b.d.	0.02	98.73	1.994	0.006	-	2.0	0.015	0.269	0.002	0.003	0.467	0.185	0.043	-	0.001	1.0	0.723	0.292	1.0	70.15	1.62	28.23	46.65	22.80	29.24	Aeg-Aug
Z3 4	2	51.54	0.12	0.69	0.00	14.92	1.34	7.97	18.65	3.35	b.d.	b.d.	98.58	1.974	0.026	-	2.0	0.006	0.256	0.003	0.000	0.455	0.222	0.044	-	-	1.0	0.766	0.249	1.0	74.35	0.55	25.10	45.52	26.53	24.88	Aeg-Aug
Z3 5	3	52.27	0.12	0.62	b.d.	14.06	1.24	8.64	18.41	3.59	b.d.	0.04	98.99	1.982	0.018	-	2.0	0.010	0.260	0.004	-	0.489	0.186	0.040	-	0.001	1.0	0.748	0.264	1.0	72.95	0.96	26.10	48.85	22.64	26.38	Aeg-Aug
Z3 6	1	51.97	0.14	0.66	b.d.	14.32	1.19	8.02	18.10	3.59	0.01	b.d.	98.01	1.996	0.004	-	2.0	0.026	0.233	0.004	-	0.459	0.227	0.039	0.000	-	1.0	0.745	0.268	1.0	72.78	2.71	24.51	45.93	26.50	26.75	Aeg-Aug
Z3 7	rim 2	51.60	0.11	1.46	b.d.	7.90	0.78	12.01	22.44	1.41	0.00	b.d.	97.71	1.956	0.044	-	2.0	0.022	0.124	0.003	-	0.679	0.127	0.025	0.000	-	1.0	0.912	0.103	1.0	89.25	1.61	9.14	67.87	15.20	10.34	Di
Z3 8	3	52.31	0.03	0.60	0.01	12.32	1.14	9.33	20.09	2.85	0.03	0.01	98.71	1.987	0.013	-	2.0	0.014	0.203	0.001	0.000	0.528	0.188	0.037	0.001	0.000	1.0	0.818	0.210	1.0	78.53	1.38	20.09	52.82	22.52	20.97	Aeg-Aug
Z5 19		52.41	0.17	0.51	b.d.	13.15	1.05	9.61	19.06	3.18	0.05	b.d.	99.18	1.978	0.022	-	2.0	0.001	0.239	0.005	-	0.541	0.177	0.034	0.002	-	1.0	0.771	0.232	1.0	76.20	0.11	23.69	54.07	21.03	23.24	Aeg-Aug
Z5 20		52.23	0.14	0.56	b.d.	13.57	1.20	9.19	19.45	3.08	0.01	0.01	99.42	1.973	0.025	0.002	2.0	-	0.239	0.004	-	0.517	0.188	0.038	0.000	0.000	1.0	0.787	0.226	1.0	76.80	0.00	23.20	51.74	22.61	22.55	Aeg-Aug
Z5 21		51.39	0.12	0.56	b.d.	13.63	1.16	9.05	19.41	2.91	b.d.	0.01	98.22	1.968	0.025	0.007	2.0	-	0.236	0.004	-	0.517	0.193	0.038	-	0.000	1.0	0.796	0.216	1.0	77.72	0.00	22.28	51.67	23.05	21.58	Aeg-Aug
Z5 22		52.04	0.10	0.48	0.01	13.57	1.07	9.03	18.79	3.50	b.d.	b.d.	98.61	1.976	0.022	0.002	2.0	-	0.269	0.003	0.000	0.511	0.160	0.035	-	-	1.0	0.765	0.257	1.0	73.61	0.00	26.39	51.14	19.47	25.74	Aeg-Aug
Z7 5	1	52.16	0.11	0.36	b.d.	13.10	1.28	9.37	19.46	3.19	b.d.	0.01	99.03	1.974	0.016	0.010	2.0	-	0.248	0.003	-	0.529	0.156	0.041	-	0.000	1.0	0.789	0.234	1.0	75.87	0.00	24.13	52.85	19.67	23.42	Aeg-Aug
Z7 6	2	51.73	0.10	0.64	b.d.	11.25	1.11	10.22	21.63	1.96	0.00	b.d.	98.64	1.968	0.029	0.003	2.0	-	0.169	0.003	-	0.580	0.186	0.036	0.000	-	1.0	0.882	0.145	1.0	85.06	0.00	14.94	57.97	22.19	14.47	Di
Z7 8	3	52.70	0.03	0.34	0.03	13.67	1.08	9.25	18.73	3.56	b.d.	0.01	99.38	1.984	0.015	0.001	2.0	-	0.267	0.001	0.001	0.519	0.162	0.034	-	0.000	1.0	0.755	0.260	1.0	73.45	0.00	26.55	51.91	19.64	25.96	Aeg-Aug
Z7 9	4	52.23	0.12	0.38	b.d.	13.27	1.14	8.93	18.52	3.28	0.02	b.d.	97.89	2.002	-	-	2.0	0.017	0.213	0.003	-	0.510	0.213	0.037	0.001	-	1.0	0.761	0.244	1.0	75.27	1.84	22.89	51.01	24.95	24.37	Aeg-Aug
Z7 10	5	52.14	0.13	0.66	0.01	12.99	1.11	9.17	19.12	3.20	0.01	b.d.	98.54	1.983	0.018	-	2.0	0.012	0.229	0.004	0.000	0.520	0.184	0.036	0.000	-	1.0	0.779	0.236	1.0	75.87	1.22	22.90	52.00	22.00	23.58	Aeg-Aug
Z7 11	6	52.33	0.10	0.53	0.00	12.27	1.18	9.67	19.73	3.08	b.d.	b.d.	98.89	1.978	0.022	-	2.0	0.002	0.236	0.003	0.000	0.545	0.152	0.038	-	-	1.0	0.799	0.226	1.0	76.79	0.17	23.04	54.50	18.94	22.60	Aeg-Aug
Z8 3	1	51.99	0.12	0.63	b.d.	12.74	1.08	9.47	20.04	2.44	0.00	b.d.	98.51	1.986	0.014	-	2.0	0.014	0.172	0.004	-	0.539	0.236	0.035	0.000	-	1.0	0.820	0.181	1.0	81.52	1.41	17.07	53.90	27.06	18.08	Di
Z8 5	2	50.49	0.41	1.85	0.01	10.15	1.01	11.22	23.51	0.95	b.d.	0.03	99.63	1.903	0.082	0.015	2.0	-	0.141	0.012	0.000	0.630	0.164	0.032	-	0.001	1.0	0.950	0.070	1.0	92.60	0.00	7.40	63.04	19.61	6.97	Di
TW10													0.00																								
Z1 1		51.45	0.28	0.69	0.06	14.92	1.44	7.74	18.07	3.52	b.d.	b.d.	98.16	1.980	0.020	-	2.0	0.011	0.249	0.008	0.002	0.444	0.231	0.047	-	-	1.0	0.745	0.263	1.0	73.00	1.16	25.83	44.37	27.81	26.25	Aeg-Aug
Z1 2	1	52.67	0.18	0.42	b.d.	11.72	1.07	10.42	20.48	2.37	0.02	b.d.	99.36	1.986	0.014	-	2.0	0.004	0.171	0.005	-	0.586	0.198	0.034	0.001	-	1.0	0.827	0.173	1.0	82.29	0.43	17.28	58.57	23.26	17.34	Di
Z1 3	2	52.43	0.07	0.36	0.01	11.60	1.06	10.30	20.29	2.56	b.d.	0.01	98.70	1.986	0.014	-	2.0	0.002	0.192	0.002	0.000	0.582	0.176	0.034	-	0.000	1.0	0.824	0.188	1.0	80.77	0.23	19.00	58.18	20.94	18.82	Di
Z1 4	1	51.67	0.18	0.65	b.d.	14.11	1.17	8.51	19.15	3.13	b.d.	0.01	98.58	1.975	0.025	-	2.0	0.004	0.237	0.005	-	0.485	0.214	0.038	-	0.000	1.0	0.785	0.232	1.0	76.19	0.43	23.37	48.50	25.18	23.18	Aeg-Aug
Z1 5	2	51.96	0.22	0.44	b.d.	16.02	1.02	6.93	15.93	4.70	b.d.	b.d.	97.20	2.010	-	-	2.0	0.020	0.293	0.006	-	0.400	0.225	0.033	-	-	1.0	0.660	0.352	1.0	64.58	2.24	33.18	39.99	25.82	35.24	Aeg-Aug
Z1 6	3	50.99	0.23	0.70	b.d.	14.61	1.46	8.10	18.52	3.38	b.d.	b.d.	98.00	1.963	0.032	0.006	2.0	-	0.270	0.007	-	0.465	0.194	0.048	-	-	1.0	0.764	0.252	1.0	73.83	0.00	26.17	46.46	24.20	25.21	Aeg-Aug
Z1 7	4	53.20	0.06	0.46	b.d.	11.59	1.08	10.79	19.86	2.17	b.d.	b.d.	99.20	2.008	-	-	2.0	0.021	0.118	0.002	-	0.607	0.248	0.005	-	-	1.0	0.803	0.159	1.0	83.93	2.38	13.69	60.72	25.28	15.87	Di
Z1 8	5	51.54	0.30	0.75	0.02	14.31	1.23	8.09	18.53	3.40	0.01	0.01	98.18	1.979	0.021	-	2.0	0.012	0.240	0.009	0.001	0.463	0.220	0.040	0.000	0.000	1.0	0.762	0.253	1.0	74.07	1.28	24.65	46.27	25.99	25.28	Aeg-Aug
Z1 9		52.22	0.05	0.50	b.d.	11.68	1.10	10.32	20.82	2.30	b.d.	0.01	99.01	1.976	0.022	0.002	2.0	-	0.187	0.002	-	0.582	0.182	0.035	-	0.000	1.0	0.844	0.169	1.0	82.66	0.00	17.34	58.20	21.68	16.86	Di
Z2 7	1	51.23	0.66	0.95	0.08	15.59	1.12	7.42	16.63	4.43	b.d.	0.02	98.14	1.963	0.037	-	2.0	0.006	0.312	0.019	0.002	0.424	0.188	0.036	-	0.001	1.0	0.683	0.329	1.0	66.28	0.64	33.09	42.38	22.44	32.94	Aeg-Aug
Z2 8	rim 2	50.85	0.37	1.10	b.d.	15.51	0.89	7.20	18.01	3.56	b.d.	b.d.	97.50	1.973	0.027	-	2.0	0.023	0.246	0.011	-	0.416	0.258	0.029	-	-	1.0	0.749	0.268	1.0	72.63	2.33	25.04	41.64	28.68	26.80	Aeg-Aug
Z2 9	3	50.93	0.53	0.99	b.d.	14.68	1.11	7.95	18.16	3.66	0.04	b.d.	98.07	1.956	0.044	-	2.0	0.001	0.278	0.015	-	0.455	0.193	0.036	0.001	-	1.0	0.747	0.273	1.0	71.91	0.08	28.01	45.53	22.93	27.26	Aeg-Aug
Z2 10	4	51.09	0.68	0.99	b.d.	14.24	1.19	7.98	18.49	3.32	0.01	0.04	98.02	1.968	0.032	-	2.0	0.013	0.223	0.020	-	0.458	0.235	0.039	0.000	0.001	1.0	0.763	0.248	1.0	74.62	1.39	24.00	45.79	27.39	24.77	Aeg-Aug
Z4 11		52.38	0.11	0.24	0.04	12.50	0.82	9.66	17.82	4.02	b.d.	0.01	97.60	1.991	0.009	-	2.0	0.002	0.289	0.003	0.001	0.547	0.108	0.027	-	0.000	1.0	0.726	0.296	1.0	69.98	0.19	29.84	54.73	13.44	29.62	Aeg-Aug
Z4 12		51.39	0.04	0.28	b.d.	11.92	1.04	9.56	18.19	3.55	b.d.	0.02	95.98	1.991	0.009	-	2.0	0.004	0.263	0.001	-	0.552	0.123	0.034	-	0.001	1.0	0.755	0.267	1.0	72.85	0.40	26.76	55.24	15.71	26.66	Aeg-Aug
Z4 13		52.03	0.22	0.42	b.d.	12.64	1.02	9.65	19.16	3.22	b.d.	b.d.	98.35	1.977	0.019	0.005	2.0	-	0.243	0.006	-	0.546	0.154	0.033	-	-	1.0	0.780	0.237	1.0	75.77	0.00	24.23	54.64	18.68	23.68	Aeg-Aug
Z6 11	1	52.02	0.07	0.68	0.05	10.44	1.13	10.99	20.98	2.39	0.03	0.00	98.80	1.960	0.030	0.010	2.0	-	0.205	0.002	0.002	0.618	0.114	0.036	0.001	0.000	1.0	0.847	0.175	1.0	81.87	0.00	18.13	61.76	15.05	17.48	Di
Z6 12	2	52.29	0.06	0.51	0.06	10.87	1.09	10.59	21.09	2.38	0.04	b.d.	98.96	1.973	0.023	0.004	2.0	-	0.193	0.002	0.002	0.596	0.146	0.035	0.001	-	1.0	0.853	0.174	1.0	82.08	0.00	17.92	59.56	18.10	17.40	Di
Z6 13	3	51.87	0.04	0.87	0.02	8.75	1.04	12.08	23.52	1.03	b.d.	0.00	99.23	1.951	0.039	0.010	2.0	-	0.120	0.001	0.001	0.677	0.145	0.033	-	0.000	1.0	0.948	0.075	1.0	92.16	0.00	7.84	67.72	17.82	7.53	Di
Z6 14	rim 4	52.36	0.04	0.59	b.d.	7.45	1.03	13.10	24.22	0.68	b.d.	b.d.	99.48	1.957	0.026	0.017	2.0	-	0.089	0.001	-	0.730	0.127	0.033	-	-	1.0	0.970	0.049	1.0	94.89	0.00	5.11	73.02	16.00	4.92	Di

Notes:
Analyses with high or low totals (>101 or <96 wt.%) or poor stoichiometries are omitted.
Abbreviations: b.d. = below detection; Di = Diopside; Aeg-Aug = Aegirine-Augite.

Table 3
Representative EPMA compositions of garnet from the Twihinate antiskarn (West African Craton Margin, Moroccan Sahara).

Sample	SiO_2	TiO_2	Al_2O_3	Cr_2O_3	FeO	MnO	MgO	ZnO	CaO	Total	Si	Al^{IV}	Al^{VI}	Ti^{4+}	Cr^{2+}	Fe^{3+}	Fe^{2+}	Mn^{2+}	Mg^{2+}	Zn	Ca^{2+}	Total	And	Grs	Pyr	Sps	Uva
TW9																											
Z5 12	33.03	2.46	2.13	0.03	23.56	0.59	0.62	0.03	32.52	97.20	2.875	0.125	0.108	0.161	0.002	1.442	0.273	0.044	0.081	0.002	3.033	8.15	86.70	8.16	3.24	1.75	0.14
Z5 13	33.47	3.06	2.16	b.d.	23.57	0.66	0.70	b.d.	32.68	98.50	2.870	0.130	0.101	0.197	-	1.420	0.270	0.048	0.090	-	3.002	8.13	86.70	7.68	3.65	1.96	-
Z5 14	34.53	2.04	0.82	b.d.	25.88	0.74	0.30	b.d.	32.47	99.11	2.962	0.038	0.051	0.132	-	1.508	0.348	0.054	0.038	-	2.985	8.12	94.77	1.41	1.59	2.24	-
Z5 15	33.83	2.30	1.72	0.07	23.73	0.64	0.70	b.d.	32.69	97.92	2.918	0.082	0.104	0.149	0.005	1.450	0.261	0.047	0.090	-	3.021	8.13	88.97	5.13	3.69	1.92	0.30
Z5 16	32.73	2.39	1.85	0.04	23.69	0.60	0.69	b.d.	32.68	96.92	2.863	0.137	0.066	0.157	0.003	1.479	0.254	0.045	0.090	-	3.063	8.16	88.44	6.01	3.60	1.78	0.16
Z5 17	32.44	2.43	2.17	0.01	23.40	0.62	0.58	0.01	32.59	96.47	2.850	0.150	0.090	0.161	0.001	1.459	0.260	0.046	0.076	0.001	3.068	8.16	86.60	8.51	3.01	1.83	0.05
Z5 18	31.92	2.66	2.02	b.d.	23.83	0.61	0.68	b.d.	32.43	96.40	2.815	0.185	0.039	0.177	-	1.488	0.269	0.045	0.090	-	3.065	8.17	87.61	7.08	3.52	1.79	-
Z6 5	33.58	2.38	1.38	0.02	24.47	0.71	0.57	b.d.	32.61	97.99	2.906	0.094	0.057	0.155	0.001	1.487	0.284	0.052	0.073	-	3.025	8.13	91.27	3.54	3.00	2.12	0.07
Z6 6	33.50	2.67	2.16	0.02	23.39	0.64	0.67	b.d.	32.61	97.86	2.889	0.111	0.122	0.173	0.002	1.421	0.266	0.047	0.086	-	3.014	8.13	86.55	7.96	3.50	1.90	0.10
Z6 7	32.74	2.65	2.21	0.02	23.56	0.63	0.64	b.d.	32.54	97.19	2.853	0.147	0.094	0.173	0.002	1.445	0.272	0.046	0.083	-	3.037	8.15	86.37	8.39	3.29	1.85	0.09
Z6 8	33.08	2.36	1.79	b.d.	23.39	0.65	0.66	0.01	32.31	96.46	2.899	0.101	0.096	0.156	-	1.457	0.257	0.049	0.087	0.001	3.035	8.14	88.77	5.74	3.52	1.97	-
TW10																											
Z3 1	34.41	1.63	2.28	b.d.	23.11	0.61	0.71	0.08	32.43	97.41	2.968	0.032	0.213	0.106	-	1.403	0.264	0.044	0.092	0.005	2.997	8.12	85.84	8.62	3.73	1.80	-
Z3 2	34.82	1.70	2.24	b.d.	22.94	0.60	0.69	0.02	32.61	97.77	2.986	0.014	0.226	0.110	-	1.389	0.256	0.043	0.088	0.001	2.997	8.11	86.00	8.57	3.64	1.79	-
Z3 3	34.31	1.69	2.17	b.d.	23.16	0.65	0.76	0.02	32.61	97.55	2.957	0.043	0.191	0.109	-	1.418	0.252	0.047	0.097	0.001	3.012	8.13	86.57	7.55	3.95	1.93	-
Z3 4	34.26	1.34	1.93	b.d.	23.32	0.66	0.68	b.d.	32.60	97.02	2.973	0.027	0.184	0.087	-	1.441	0.251	0.049	0.088	-	3.031	8.13	87.94	6.49	3.59	1.98	-
Z4 8	34.40	1.22	1.51	b.d.	24.29	0.52	0.51	b.d.	32.81	97.53	2.980	0.020	0.144	0.080	-	1.478	0.282	0.038	0.066	-	3.046	8.13	90.58	5.17	2.69	1.57	-
Z4 9	34.57	1.49	1.89	b.d.	23.61	0.60	0.65	0.06	32.80	97.89	2.974	0.026	0.178	0.096	-	1.439	0.260	0.044	0.083	0.004	3.024	8.13	88.24	6.57	3.39	1.80	-
Z4 10	34.02	2.06	2.08	0.06	22.71	0.57	0.73	0.03	32.76	97.19	2.942	0.058	0.167	0.134	0.004	1.413	0.230	0.042	0.094	0.002	3.036	8.12	86.74	7.45	3.84	1.72	0.26
Z5 1	34.71	1.51	2.12	0.05	23.15	0.57	0.60	0.07	32.72	97.68	2.985	0.015	0.213	0.098	0.004	1.406	0.259	0.042	0.077	0.005	3.015	8.12	86.58	8.33	3.16	1.71	0.22
Z5 2	33.44	2.36	2.23	0.06	22.64	0.56	0.79	0.04	32.63	96.91	2.904	0.096	0.147	0.154	0.004	1.415	0.230	0.041	0.102	0.003	3.037	8.13	85.92	8.05	4.13	1.67	0.23
Z5 3	34.47	1.79	2.26	b.d.	22.93	0.58	0.70	0.04	32.79	97.72	2.962	0.038	0.205	0.115	-	1.402	0.246	0.042	0.089	0.002	3.019	8.12	85.95	8.68	3.65	1.73	-
Z5 4	33.50	2.07	2.38	0.06	22.82	0.60	0.91	0.05	32.62	97.19	2.902	0.098	0.161	0.135	0.004	1.420	0.233	0.044	0.117	0.003	3.027	8.14	85.17	8.13	4.69	1.77	0.24
Z5 5	33.87	1.44	2.00	0.10	23.80	0.57	0.63	b.d.	32.84	97.48	2.935	0.065	0.152	0.094	0.007	1.457	0.268	0.042	0.081	-	3.050	8.15	87.35	7.32	3.24	1.67	0.43
Z5 6	33.38	1.64	1.95	0.05	23.38	0.56	0.58	0.08	32.67	96.50	2.923	0.077	0.137	0.108	0.003	1.460	0.252	0.041	0.076	0.005	3.066	8.15	87.74	7.38	3.03	1.66	0.19
Z6 15	35.09	1.03	1.52	b.d.	24.50	0.64	0.55	b.d.	32.74	98.33	3.010	0.000	0.164	0.067	-	1.464	0.293	0.046	0.070	-	3.010	8.12	90.50	4.72	2.87	1.91	-
Z6 16	34.68	1.51	2.17	b.d.	23.31	0.57	0.64	b.d.	32.77	97.82	2.979	0.021	0.212	0.098	-	1.411	0.264	0.041	0.082	-	3.016	8.12	86.55	8.42	3.35	1.69	-
Z6 17	35.03	1.25	2.05	0.01	23.78	0.59	0.60	0.02	32.72	98.24	2.998	0.002	0.218	0.080	0.000	1.419	0.283	0.042	0.076	0.001	3.001	8.12	87.28	7.83	3.12	1.74	0.03

NOTES: b.d. = below detection
Analyses with high or low totals (>101 or <96 wt%) or poor stoichiometries are omitted.

Table 4
Representative EPMA compositions of micas from the Twihinate antiskarn (West African Craton Margin, Moroccan Sahara).

	Biotite								Phlogopite	
	TW9 (n = 31)		TW10 (n = 14)		D7b (n = 14)		D7a (n = 13)		W8 (n = 12)	
%	Avg	Std	Avg	Std	Avg	Std	Avg	Std	Avg	Std
SiO_2	36.40	0.91	37.49	0.62	36.68	1.10	37.93	1.05	39.16	0.84
TiO_2	1.31	0.23	1.28	0.27	1.12	0.21	1.02	0.22	1.52	0.67
Al_2O_3	10.91	0.46	10.57	0.50	14.14	0.40	13.90	0.91	11.86	0.93
FeO	21.44	2.37	17.25	1.47	14.07	0.33	13.82	0.59	6.51	0.40
MnO	1.52	0.19	1.14	0.15	0.13	0.02	0.14	0.03	0.13	0.02
MgO	13.64	1.53	16.71	1.10	17.12	1.13	16.92	0.96	24.29	1.01
CaO	0.10	0.07	0.12	0.09	0.06	0.04	0.07	0.05	0.10	0.07
Na_2O	0.10	0.07	0.14	0.06	0.05	0.02	0.05	0.03	0.39	0.04
K_2O	9.09	0.69	9.26	0.53	8.50	1.05	8.95	0.57	9.15	0.42
Cr_2O_3	0.01	0.02	0.02	0.04	0.10	0.06	0.09	0.06	0.02	0.02
NiO	0.01	0.01	0.00	0.01	0.03	0.02	0.02	0.01	0.03	0.02
BaO	0.02	0.03	0.01	0.02	1.41	0.27	1.30	0.58	0.47	0.66
H_2O	3.61	0.09	3.65	0.13	3.60	0.10	3.58	0.09	3.79	0.14
F	0.38	0.15	0.43	0.23	0.58	0.16	0.71	0.16	0.58	0.24
Cl	0.01	0.01	0.01	0.01	0.04	0.01	0.05	0.02	0.01	0.01
Total	98.57	1.16	98.11	1.16	97.67	1.26	98.58	0.87	98.04	1.11
Number of cations on the basis of 22 (O)										
O = F,Cl	0.16	0.06	0.18	0.10	0.25	0.07	0.31	0.07	0.24	0.10
Total	98.41	1.14	97.93	1.16	97.41	1.25	98.27	0.89	97.79	1.08
Si	5.66	0.05	5.71	0.05	5.54	0.10	5.64	0.10	5.62	0.08
Al^{IV}	2.00	0.08	1.90	0.09	2.46	0.10	2.35	0.12	2.01	0.15
Al^{VI}	0.00	0.00	0.00	0.00	0.06	0.05	0.09	0.07	0.00	0.00
Ti^{4+}	0.15	0.03	0.15	0.03	0.13	0.02	0.11	0.02	0.16	0.07
Fe^{2+}	2.80	0.35	2.20	0.20	1.78	0.05	1.72	0.09	0.78	0.05
Cr^{2+}	0.00	0.00	0.00	0.00	0.01	0.01	0.01	0.01	0.00	0.00
Mn^{2+}	0.20	0.03	0.15	0.02	0.02	0.00	0.02	0.00	0.02	0.00
Mg^{2+}	3.16	0.31	3.79	0.22	3.86	0.29	3.75	0.19	5.20	0.19
Ca^{2+}	0.02	0.01	0.02	0.01	0.01	0.01	0.01	0.01	0.01	0.01
Na^{+}	0.03	0.02	0.04	0.02	0.01	0.00	0.02	0.01	0.11	0.01
K^{+}	1.80	0.11	1.80	0.09	1.64	0.19	1.70	0.10	1.68	0.08
Ni	0.00	0.00	0.00	0.00	0.00	0.00	0.00	0.00	0.00	0.00
OH^{-}	3.81	0.07	3.79	0.11	3.71	0.08	3.65	0.07	3.74	0.11
Total	19.63	0.10	19.54	0.11	19.23	0.13	19.06	0.09	19.33	0.12
F	0.19	0.07	0.21	0.11	0.28	0.08	0.34	0.08	0.26	0.11
Cl	0.00	0.00	0.00	0.00	0.01	0.00	0.01	0.00	0.00	0.00
XMg	0.53	0.05	0.63	0.03	0.68	0.01	0.69	0.02	0.87	0.01

NOTES
Analyses with high or low totals (>101 or <96 wt.%) or poor stoichiometries are omitted.
Abbreviations: Avg = average; Std = standard deviation

8.4. Magnetite

LA-ICP-MS compositions for Mag-2 from the antiskarn rocks show high and variable amounts of Mn (1.4 to 1.9 wt%), Ti (0.7 to 16. 9 wt%), and V (0.2 to 0.7 wt%) (Table 6). Cobalt, nickel and gallium are present at the ppm or tens of ppm levels, with average concentrations of 43 ppm, 31 ppm, and 21 ppm, respectively. Zn abundances are in the range of 1800–3300 ppm, with an average content of 2530 ppm. The concentration of Ge is consistently ~2–3 ppm. Abundances of other elements such as Ca, Sc, Ni, Cu, Y, Mo, W, Pb, Th and U are either close to, or below, detection limits. The continental-crust normalized multi-elemental patterns show prominent troughs at Cu, Co, Zr, Ta, and Ga coupled with relative enrichment of Ge, Nb, Mn, Zn, V (Fig. 12A). A characteristic compositional feature is the decoupling of Nb and Ta which contrasts with the behaviour in this pair of conjugate elements in most silicate igneous rocks. These patterns are typical of magnetite from carbonatite complexes worldwide (Chen et al., 2019). Rare earth elements, although rarely reported for magnetite owing to their low abundances, are detectable in some magnetite from Twihinate prospect ranging from below detection limit to 2 ppm (Table 6). Continental-crust normalized REE patterns (Fig. 12B) show a smooth negative slope arising from strong enrichment in light rare earth elements (LREE = La-Eu) over heavy REE (HREE = Gd-Lu) (Fig. 12B). Both the slope and lack of Eu anomaly are similar to those commonly reported for carbonatite-related magnetite (Chen et al., 2019). A remarkable compositional feature of the Twihinate magnetite resides in its substantial enrichment in Nb with concentrations up to 220 ppm (average = 53 ppm). Apart from this, the compositions of the Twihinate antiskarn magnetite (Mag-2) are strikingly similar to those reported for Oka and Mushgai Khudag carbonatite complexes but quite distinct from those characterizing iron oxides from Bayan Obo and Hongcheon carbonatites (Fig. 12).

8.5. Pyrochlore

In addition to magnetite chemistry, EPMA analyses show that uranpyrochlore (Pcl-2) is the dominant phase of pyrochlore group minerals in the antiskarn rocks (Table 7), while U-poor pyrochlore (Pcl-1) occurs as an early orthomagmatic phase in the fresh sövite (Fig. 9C) with ThO_2 and UO_2 concentrations commonly below detection limit (Benaouda et al., 2020b). Similar to the radioactive elements, the total REE + Y concentrations along with Ba and Sr contents are also low commonly near or below detection limits (Y + REE_2O_3 = 1.75–3.86 wt %). No microlite is identified due to the absence of Ta. Pcl-1 is therefore classified as pyrochlore *sensu stricto*, typical of igneous pyrochlore from carbonatites worldwide (Hogarth et al., 2000; Walter et al., 2018). Conversely, Pcl-2 shows remarkable ThO_2 and UO_2 enrichments, up to 22.5 wt% and 3.0 wt%, respectively (Table 7) which set them apart both from igneous Pcl-1 (U-poor pyrochlore) (Fig. 13A, B). Nb is predominant at the B site, whereas the Y-site is fully occupied by OH. Based on these compositional features (i.e., relative Nb, U, and Ti contents), the Pcl-2 compositions which plot with >40% Nb, ≤35% Ti, and <40% Ta on a Nb-Ti-Ta ternary diagram (Fig. 13A) are better defined as

Table 5
Representative EPMA compositions of chlorite from the Twihinate antiskarn (West African Craton Margin, Moroccan Sahara).

SAMPLE	SiO_2	TiO_2	Al_2O_3	Cr_2O_3	FeO	MnO	NiO	CoO	MgO	CaO	Na_2O	K_2O	Cl	H_2O*	Total	Si	Al^{IV}	Al^{VI}	Ti	Cr	Fe^{2+}	Mn	Ni	Co	Mg	Ca	Na	K	Cl	OH^-	XFe	Nomenclature
W8																																
Z3 13	33.22	0.11	11.98	b.d.	13.71	0.67	0.05	n.a.	24.05	0.86	0.13	0.24	n.a.	11.73	96.76	3.397	0.603	0.841	0.009	-	1.172	0.058	0.004	-	3.666	0.095	0.027	0.032	-	8.00	0.24	diabanite
Z3 14	32.82	0.17	13.20	0.06	11.61	0.81	0.03	n.a.	24.39	0.97	0.18	0.12	n.a.	11.77	96.11	3.345	0.655	0.931	0.013	0.005	0.989	0.070	0.002	-	3.706	0.106	0.035	0.016	-	8.00	0.21	diabanite
Z5 1	31.62	0.13	11.60	b.d.	16.17	0.72	b.d.	n.a.	23.67	0.75	0.10	0.36	n.a.	11.52	96.63	3.292	0.708	0.715	0.010	-	1.408	0.064	-	-	3.674	0.083	0.021	0.048	-	8.00	0.28	diabanite
Z5 2	34.17	0.06	10.64	0.04	14.28	0.46	0.04	n.a.	25.53	0.69	0.10	0.13	n.a.	11.88	98.01	3.451	0.549	0.718	0.005	0.003	1.206	0.040	0.003	-	3.844	0.074	0.019	0.017	-	8.00	0.24	diabanite
Z5 3	31.73	0.09	11.94	0.06	14.95	0.68	0.01	n.a.	24.45	0.74	0.16	0.14	n.a.	11.60	96.55	3.282	0.718	0.738	0.007	0.005	1.293	0.060	0.001	-	3.770	0.082	0.033	0.018	-	8.00	0.26	diabanite

NOTES: Analyses with high or low totals (>101 or <96 wt%) or poor stoichiometries are omitted.
n.a. = not analyzed

uranpyrochlore.

8.6. Apatite

In addition to magnetite and uranpyrochlore compositions, trace element data of apatite are roughly consistent and plot close to end-member fluorapatite, typical of carbonatitic apatite worldwide (e.g., Teiber et al., 2015; Chakhmouradian et al., 2017) (Fig. 14). Of note is a slight excess of F over the stoichiometric value (1 apfu) in all samples which is likely due to electron beam induced F migration (Stock et al., 2015). The Na contents are consistently low, whereas Cl is below its limit of detection (~200 ppm) (Table 8).

9. Discussion

While there remains some controversy regarding the origin of the Twihinate Nb-P-Fe ± LREE ± U-Th-rich mineralization, the calc-silicate paragenesis and related mineralization described in this study could provide insights into key processes of its genesis. In a recent study, Benaouda et al. (2020b) advocated that the Twihinate mineralization shares mineralogical attributes in common with Iron-Oxide-Apatite ± REE (IOA; Groves et al., 2010) ore deposits and attributed ore formation to epigenetic processes linked with late-stage circulation of hydrothermal fluids of unknown age(s) and origin(s).

A crucial finding of this study relies on the analogy between the Twihinate calc-silicate paragenesis and the experimentally mineral succession synthetized through contamination of the crystallizing carbonatitic magma by surrounding silica-rich country rocks at temperatures of 550 to 650 °C (Anenburg and Mavrogenes, 2018; Stoppa et al., 2021). As the resulting metasomatic lithotypes are spatially associated with, and genetically related to, the Twihinate sövite, and owing to the fact that the observed crystallization sequence of calc-silicate succession (Fig. 8) matches with the experimental work of Anenburg and Mavrogenes (2018), the Twihinate metasomatic rocks are therefore defined as antiskarns. Here, the term antiskarn refers to Ca-Mg-Fe-Mn-Al silicate-bearing rocks whose genesis is linked to crustally contaminated carbonatite melt in which alkalis are yet to be strongly enriched while concentrations of Mg- and Ca-silicates in the crystallizing residual melt tend to be significant. At this stage, the resulting calc-silicate paragenesis (e.g., diopside, andradite, phlogopite, and titanite) resemble those prograde and retrograde mineral suites that are typically described in skarn deposits (Meinert et al., 2005). Whilst these latter are thought to form by replacement processes (i.e., diffusion and/or dissolution and reprecipitation) when magmatic-hydrothermal fluids expelled from cooling magmas react metasomatically with a reactive protolith of either igneous or sedimentary origin, the calc-silicate paragenesis described therein is interpreted to have formed from contamination of the crystallizing carbonatitic magma by surrounding silica-rich country rocks as shown below. Equally important, the term antiskarn has to be distinguished from the high-temperature metasomatically altered local rocks surrounding carbonatite intrusions known as fenites. These are commonly viewed to result from the involvement of alkali-rich aqueous fluids exsolved from cooling and crystallizing carbonatitic or alkaline melt (Zharikov et al., 2007; Elliott et al., 2018; Yaxley et al., 2022).

More importantly, the analogy between the Twihinate calc-silicate paragenesis and the experimentally produced mineral succession of Anenburg and Mavrogenes (2018) provides permissive evidence that similar physicochemical conditions and ore-forming processes may have prevailed in both systems. In this respect, the experiments of Anenburg and Mavrogenes (2018) invoked a carbonatite origin for the hydrothermal REE-P-U mineralization at Nolans Bore deposit via reactive interaction of carbonatite melt with silicate host rocks. Unlike Nolans Bore where the mineralized structures are not spatially associated with known carbonatite occurrences, the ore system at Twihinate prospect is rooted within the Upper Cretaceous sövite itself and shares many diagnostic similarities with carbonatite-related deposits. A critical

Table 6
Representative LA-ICP-MS compositions of magnetite from the Twihinate antiskarn (West African Craton Margin, Moroccan Sahara).

Sample No.		TW14								TW10			TW9					
	L.D	1	2	3	4	5	6	7	8	1	2	3	1	2	3	4	5	6
Fe (wt%)	0.001	94.40	92.90	94.00	93.20	93.60	93.20	93.10	93.20	94.00	95.10	94.60	94.10	94.70	93.50	92.40	93.10	93.00
SiO_2	0.166	b.d.	0.42	b.d.	0.17	b.d.	b.d.	b.d.	b.d.	b.d.	0.17	b.d.	b.d.	b.d.	0.29	0.89	b.d.	b.d.
Na	7.99	68.40	61.00		37.40	22.10	21.00	58.90	b.d.	75.60	29.70	b.d.	b.d.	9.90	b.d.	610.00	b.d.	b.d.
Mg	0.329	1432.00	1366.00	1268.00	1465.00	1437.00	1493.00	1370.00	1667.00	1607.00	1304.00	1156.00	460.00	461.00	1043.00	1996.00	1068.00	1127.00
Al	0.301	625.00	748.00	642.00	1033.00	478.00	682.00	823.00	1067.00	3367.00	2958.00	2724.00	1005.00	1083.00	902.00	1084.00	726.00	736.00
K	2.3	b.d.	b.d.	166.00	b.d.	b.d.	31.90	b.d.	b.d.	b.d.	b.d.	b.d.	b.d.	b.d.	b.d.	315.00	b.d.	b.d.
Ca	184	b.d.	b.d.	b.d.	b.d.	b.d.	b.d.	b.d.	b.d.	b.d.	b.d.	b.d.	b.d.	b.d.	b.d.	757.00	b.d.	b.d.
Sc	0.206	b.d.	b.d.	b.d.	b.d.	b.d.	b.d.	b.d.	b.d.	b.d.	b.d.	b.d.	b.d.	b.d.	b.d.	b.d.	b.d.	b.d.
Ti	0.1	13217.00	15832.00	13990.00	14881.00	15284.00	15787.00	15987.00	14811.00	11234.00	7154.00	9088.00	10251.00	10272.00	13792.00	15036.00	15782.00	16867.00
V	0.03	5955.00	7267.00	6883.00	6915.00	6841.00	7155.00	7155.00	7126.00	2469.00	2550.00	2438.00	6636.00	6639.00	6948.00	7163.00	6147.00	6761.00
Cr	1	b.d.	b.d.	b.d.	b.d.	b.d.	b.d.	b.d.	b.d.	b.d.	b.d.	b.d.	2.49	b.d.	2.03	b.d.	b.d.	1.94
Mn	2.33	14091.00	17319.00	14976.00	17637.00	16624.00	17985.00	17742.00	16657.00	19615.00	16317.00	19626.00	14815.00	15544.00	16692.00	17096.00	19549.00	18193.00
Co	0.08	12.00	13.30	13.40	13.30	13.80	15.20	12.20	14.10	10.40	10.10	7.65	8.71	8.44	12.90	12.00	10.90	12.30
Ni	0.604	b.d.	b.d.	b.d.	b.d.	b.d.	b.d.	b.d.	b.d.	b.d.	b.d.	b.d.	b.d.	b.d.	b.d.	b.d.	b.d.	b.d.
Cu	0.692	0.78	b.d.	b.d.	b.d.	b.d.	b.d.	b.d.	b.d.	b.d.	b.d.	b.d.	b.d.	b.d.	b.d.	b.d.	b.d.	b.d.
Zn	1.078	2256.00	2564.00	2422.00	2992.00	2382.00	2540.00	2597.00	3285.00	2536.00	2045.00	1786.00	2299.00	1960.00	2862.00	2702.00	2827.00	2948.00
Ga	0.121	56.80	60.80	59.60	61.30	58.70	86.30	69.80	66.30	84.70	61.80	34.50	46.80	49.40	57.30	59.50	56.30	64.60
Ge	0.637	2.08	2.36	2.58	2.03	2.96	2.37	2.71	2.15	1.82	2.23	2.01	1.89	2.25	2.12	2.06	2.01	2.58
Sr	0.016	b.d.	b.d.	0.41	0.05	b.d.	0.52	0.06	b.d.	0.08	0.02	b.d.	b.d.	b.d.	b.d.	17.10	b.d.	b.d.
Y	0.039	b.d.	b.d.	0.03	b.d.	0.01	0.02	b.d.	b.d.	b.d.	b.d.	b.d.	b.d.	b.d.	b.d.	0.29	b.d.	b.d.
Zr	0.044	11.10	31.60	7.17	8.26	2.55	11.70	8.08	2.67	7.55	11.40	0.38	0.64	0.47	3.97	128.00	3.63	8.34
Nb	0.026	36.60	34.50	33.10	37.10	19.00	25.60	32.20	28.50	108.40	219.90	5.12	20.50	24.10	42.10	127.00	40.00	68.10
Mo	0.013	b.d.	0.10	0.29	b.d.	b.d.	b.d.	b.d.	b.d.	b.d.	b.d.	b.d.	b.d.	b.d.	b.d.	b.d.	b.d.	b.d.
Sn	0.343	1.88	2.30	2.30	2.14	2.62	2.30	2.52	2.33	2.47	2.47	2.08	1.64	1.73	2.05	2.67	2.17	2.28
La	0.009	b.d.	b.d.	0.14	0.01	b.d.	0.02	b.d.	b.d.	b.d.	b.d.	b.d.	b.d.	b.d.	b.d.	0.52	b.d.	b.d.
Ce	0.002	b.d.	0.03	0.21	0.05	b.d.	0.06	0.04	b.d.	0.08	b.d.	b.d.	b.d.	b.d.	b.d.	0.99	b.d.	b.d.
Pr	0.001	b.d.	b.d.	0.02	b.d.	b.d.	b.d.	b.d.	b.d.	b.d.	b.d.	b.d.	b.d.	b.d.	b.d.	0.09	b.d.	b.d.
Nd	0.003	b.d.	b.d.	0.06	b.d.	b.d.	b.d.	b.d.	b.d.	0.09	b.d.	b.d.	b.d.	b.d.	b.d.	0.44	b.d.	b.d.
Eu	0.002	b.d.	b.d.	b.d.	b.d.	b.d.	b.d.	b.d.	b.d.	b.d.	b.d.	b.d.	b.d.	b.d.	b.d.	b.d.	b.d.	b.d.
Gd	0.005	b.d.	b.d.	b.d.	b.d.	b.d.	b.d.	b.d.	b.d.	b.d.	b.d.	b.d.	b.d.	b.d.	b.d.	0.02	b.d.	b.d.
Tb	0.001	b.d.	b.d.	b.d.	b.d.	b.d.	b.d.	b.d.	b.d.	b.d.	b.d.	b.d.	b.d.	b.d.	b.d.	b.d.	b.d.	b.d.
Dy	0.005	b.d.	b.d.	b.d.	b.d.	b.d.	b.d.	b.d.	b.d.	b.d.	b.d.	b.d.	b.d.	b.d.	b.d.	b.d.	b.d.	b.d.
Ho	0.001	b.d.	b.d.	b.d.	b.d.	b.d.	b.d.	b.d.	b.d.	b.d.	b.d.	b.d.	b.d.	b.d.	b.d.	0.05	b.d.	b.d.
Er	0.001	b.d.	b.d.	b.d.	b.d.	b.d.	b.d.	b.d.	b.d.	b.d.	b.d.	b.d.	b.d.	b.d.	b.d.	0.01	b.d.	b.d.
Tm	0.001	b.d.	b.d.	b.d.	b.d.	b.d.	b.d.	b.d.	b.d.	b.d.	b.d.	b.d.	b.d.	b.d.	b.d.	0.04	b.d.	b.d.
Yb	0.006	b.d.	b.d.	b.d.	b.d.	b.d.	b.d.	b.d.	b.d.	b.d.	b.d.	b.d.	b.d.	b.d.	b.d.	0.01	b.d.	b.d.
Lu	0.007	b.d.	b.d.	b.d.	b.d.	b.d.	b.d.	b.d.	b.d.	b.d.	b.d.	b.d.	b.d.	b.d.	b.d.	0.07	b.d.	b.d.
Hf	0.012	b.d.	0.06	0.02	0.04	0.02	0.02	0.03	0.04	0.18	0.13	0.04	b.d.	b.d.	b.d.	0.17	b.d.	0.03
Ta	0.007	0.14	0.12	0.10	0.14	0.23	0.12	0.10	0.13	0.60	0.96	0.30	0.10	0.13	0.16	0.46	0.13	0.15
W	0.036	b.d.	0.47	b.d.	b.d.	b.d.	b.d.	b.d.	b.d.	b.d.	b.d.	b.d.	b.d.	b.d.	b.d.	b.d.	b.d.	b.d.
Pb	0.086	b.d.	b.d.	b.d.	b.d.	b.d.	b.d.	b.d.	b.d.	b.d.	b.d.	b.d.	b.d.	b.d.	b.d.	0.09	b.d.	b.d.
Th	0.014	b.d.	b.d.	0.11	0.01	b.d.	b.d.	b.d.	b.d.	b.d.	b.d.	b.d.	b.d.	b.d.	b.d.	0.06	b.d.	b.d.
U	0.009	b.d.	b.d.	1.31	b.d.	b.d.	0.01	b.d.	b.d.	b.d.	b.d.	b.d.	0.01	b.d.	b.d.	0.31	b.d.	b.d.

* b.d; below detection.

Table 7
Representative EPMA compositions of pyrochlore from the Twihinate antiskarn (West African Craton Margin, Moroccan Sahara).

Sample		Na_2O	CaO	La_2O_3	Ce_2O_3	ThO_2	UO_2	TiO_2	ZrO_2	FeO	Nb_2O_5	Ta_2O_5	F	H_2O	O=F	Total	Na	Ca	Fe	La	Ce	Th	U	∑A	Nb	Ta	Ti	Zr	∑B	F	OH	Total
TW9																																
Z1 15		0.10	6.74	0.16	0.83	1.05	21.77	11.73	2.57	2.28	45.23	0.10	0.55	2.02	0.23	94.91	0.003	0.475	0.125	0.004	0.020	0.016	0.318	0.96	1.339	0.002	0.577	0.082	2.00	0.114	0.886	3.85
Z1 17		0.52	4.21	0.10	0.96	1.09	21.15	11.83	2.22	3.05	46.37	0.27	0.41	2.07	0.17	94.07	0.017	0.299	0.169	0.002	0.023	0.016	0.312	0.84	1.352	0.005	0.574	0.070	2.00	0.085	0.915	3.75
Z4 15		0.55	4.15	0.18	1.14	1.95	19.69	7.83	1.52	4.29	45.82	0.08	0.21	2.00	0.09	89.33	0.019	0.317	0.256	0.005	0.030	0.032	0.313	0.97	1.514	0.002	0.430	0.054	2.00	0.047	0.953	3.92
Z4 16		0.20	6.84	0.05	1.12	0.99	13.83	10.20	1.55	3.58	52.21	0.16	0.40	2.15	0.17	93.11	0.006	0.469	0.191	0.001	0.026	0.014	0.197	0.91	1.472	0.003	0.478	0.047	2.00	0.081	0.919	3.83
Z4 17		0.70	2.88	0.23	3.26	3.39	11.11	11.60	1.92	3.54	50.55	0.17	0.29	2.15	0.12	91.66	0.022	0.202	0.194	0.005	0.078	0.050	0.162	0.71	1.404	0.003	0.536	0.057	2.00	0.060	0.940	3.65
TW10																																
Z2 11	1	4.57	18.69	0.16	0.79	0.62	3.60	6.46	2.97	0.48	56.74	0.08	3.77	0.81	1.59	98.17	0.128	1.155	0.023	0.003	0.017	0.008	0.046	1.38	1.604	0.001	0.304	0.091	2.00	0.688	0.312	3.69
Z2 12	2	4.06	16.26	0.08	0.76	1.03	15.24	10.20	2.43	0.70	45.87	0.15	2.33	1.38	0.98	99.51	0.119	1.053	0.035	0.002	0.017	0.014	0.205	1.44	1.400	0.003	0.518	0.080	2.00	0.444	0.556	4.00
Z2 13	1	5.03	18.88	0.13	0.81	0.49	0.00	5.53	2.38	0.87	61.46	0.07	5.37	0.12	2.26	98.86	0.137	1.137	0.041	0.003	0.017	0.006	0.000	1.34	1.678	0.001	0.251	0.070	2.00	0.955	0.045	3.39
Z2 14	2	5.06	18.78	0.19	0.78	0.52	0.19	5.52	2.22	1.18	61.28	0.00	5.21	0.19	2.19	98.92	0.138	1.133	0.056	0.004	0.016	0.007	0.002	1.36	1.682	0.000	0.252	0.066	2.00	0.928	0.072	3.43
Z2 15	3	4.64	16.64	0.16	0.95	1.30	8.04	6.90	2.69	1.21	54.31	0.00	3.43	0.94	1.44	99.77	0.132	1.044	0.059	0.003	0.020	0.017	0.105	1.38	1.581	0.000	0.334	0.085	2.00	0.635	0.365	3.75
Z3 12		0.11	3.38	0.34	3.50	3.43	9.87	7.42	1.56	3.53	57.35	0.13	0.50	2.07	0.21	92.98	0.003	0.235	0.192	0.008	0.083	0.051	0.143	0.72	1.605	0.002	0.345	0.047	2.00	0.103	0.897	3.61
Z3 13		0.94	6.85	0.17	1.58	1.35	11.07	8.92	2.61	2.94	56.52	0.16	0.81	2.05	0.34	95.62	0.028	0.453	0.152	0.004	0.036	0.019	0.152	0.84	1.522	0.003	0.400	0.076	2.00	0.157	0.843	3.69
Z3 14		1.85	13.71	0.36	5.13	1.89	0.84	6.21	1.12	2.73	56.59	0.19	2.80	1.11	1.18	93.35	0.055	0.904	0.140	0.008	0.116	0.026	0.012	1.26	1.659	0.003	0.303	0.035	2.00	0.544	0.456	3.72
Z3 15		0.09	3.08	0.24	2.19	1.49	9.79	3.04	1.17	3.84	65.75	0.07	0.11	2.27	0.04	93.08	0.003	0.213	0.207	0.006	0.052	0.022	0.140	0.64	1.824	0.001	0.140	0.035	2.00	0.022	0.978	3.62
Z3 16		4.34	16.50	0.21	2.56	2.68	7.93	7.54	1.33	0.96	51.08	0.24	3.48	0.84	1.46	98.22	0.127	1.066	0.048	0.005	0.056	0.037	0.106	1.45	1.567	0.005	0.385	0.044	2.00	0.663	0.337	3.78
Z3 17	1	4.90	16.20	0.25	2.09	0.42	7.52	6.40	2.26	0.32	54.10	0.00	3.74	0.73	1.58	97.35	0.142	1.040	0.016	0.005	0.046	0.006	0.100	1.36	1.610	0.000	0.317	0.073	2.00	0.709	0.291	3.65
Z3 18	2	4.91	16.77	0.27	2.29	0.45	7.15	7.01	2.52	0.38	54.36	0.00	4.76	0.30	2.00	99.16	0.140	1.054	0.018	0.006	0.049	0.006	0.093	1.37	1.582	0.000	0.339	0.079	2.00	0.883	0.117	3.48

question, however, is whether the close relationship between the Twihinate sövite and the associated mineralization-metasomatic patterns is spatial and/or genetic.

Direct evidence for a carbonatite origin for the Twihinate antiskarn and associated Nb-P-Fe ± LREE ± U-Th-rich mineralization is provided by the widespread occurrence of fluorite (Montero et al., 2014, and the present study), and the F-bearing minerals (fluorapatite and bastnäsite-(Ce)), biotite, CO_2-bearing minerals (carbonates), and calc-silicate phases (clinopyroxene, garnet, phlogopite, and titanite). Equally important, the involvement of a carbonatite component in the ore-forming system at Twihinate prospect is fully supported by the continental crust-normalized multielement patterns of magnetite (Fig. 12A) which are similar to those characterizing magnetite from carbonatite occurrences worldwide (i.e., pronounced troughs at Cu, Co, Zr, Ta, and Ga coupled with enrichment of Ge, Nb, Mn, Zn, V) (Chen et al., 2019). Moreover, the occurrence of REE–Sr–Ba pseudomorphs (Fig. 9F) which are interpreted as resulting from late-stage replacement of burbankite or calcioburbankite via interaction of the Na-rich pseudomorph-forming fluid with alkali silicate wall-rocks (Andersen et al., 2017; Kozlov et al., 2020; Chakhmouradian and Dahlgren, 2021) provides further compelling argument for the involvement of a residual carbonatitic melt during the antiskarn event. Partial replacement of burbankite by the aforementioned mineral pseudomorphs has been recognized at a number of carbonatite complexes (Zaitsev et al. 1998; Moore et al. 2015; Andersen et al., 2017; Kozlov et al., 2020; Chakhmouradian and Dahlgren, 2021). In this respect, it should be pointed out that burbankite typically forms in a magmatic environment or close to the magmatic-hydrothermal transition (Zaitsev et al., 2002; Moore et al., 2015; Broom-Fendley et al., 2017; Anenburg et al., 2020b). Permissive evidence arguing for the high-silica content of the residual carbonatite melt from which the Twihinate antiskarn calc-silicate phases precipitated comes from the widespread development of silica-rich breccias ringing the central sövite (Fig. 3).

10. Geochemical evidence for crustal assimilation during the evolution of the carbonatite melt

There is growing evidence that assimilation and recycling processes of crustal silicate wall rock play a fundamental role in carbonatite magma evolution (e.g., Chakhmouradian et al. 2008; Giebel et al. 2019; Anenburg et al. 2020a, b; Cangelosi et al., 2020; Wei et al. 2020; Walter et al., 2022) due to the high reactivity of volatile-rich carbonate melts, and the extreme geochemical contrasts with silicate wall-rocks. In the study area, several geochemical signatures of carbonatite melts allow the recognition of specific trends of crustal contribution processes during ascent and subsequent storage of these magmas in the crust, thus clearing the way for constraining the genesis of the Twihinate antiskarn and related Nb-P-Fe ± LREE ± U-Th-rich mineralization.

Stratigraphically, the ca. 421 ± 3 Ma to 410 ± 2 Ma gneissic to mylonitic peraluminous granitoids of the Laknouk suite (Montero et al., 2016; Haissen et al., 2018) are part of the country rocks at Twihinate prospect. Hence, it is necessary to evaluate whether assimilation of these rocks during the intrusion of the mantle-derived carbonatite body could have caused the trace element signature of the Twihinate antiskarn. It this respect, it should be stressed that the similarity in trace element distribution patterns of the Twihinate carbonatites and their antiskarn counterparts (Fig. 10) is suggestive of their origin from a common source.

In surface outcrop, the widespread occurrence of completely to partially replaced mafic to felsic (i.e., gneissic granite) enclaves by diopside and biotite/phlogopite along with the development of the reaction rims at the contact zone between the carbonatite and its host xenoliths (Fig. 4D, E) provide key evidence for magmatic assimilation. Similar structural and textural relationships have been observed in kimberlites contaminated by granitic xenoliths (Caro et al. 2004; Lima et al., 2020). In agreement with Hacker et al. (2005), we interpret these

Table 8
Representative EPMA compositions of apatite from the Twihinate antiskarn (West African Craton Margin, Moroccan Sahara).

Sample		P_2O_5	SiO_2	CaO	FeO	MnO	Na_2O	La_2O_3	Ce_2O_3	F	Cl	Total	O=F,Cl	Total	P	Si	Σ	Ca	Fe	Mn	Na	La	Ce	Σ	F	Cl	OH	XF	XCl	XOH
TW9																														
Z1 12		40.77	0.29	54.70	0.05	0.01	0.10	0.13	0.36	3.37	0.01	99.80	1.42	98.37	5.915	0.049	5.96	10.042	0.007	0.001	0.035	0.008	0.023	10.12	1.826	0.003	0.170	0.91	0.00	0.09
Z1 13		40.21	0.28	54.16	0.06	b.d.	0.10	0.20	0.40	3.49	0.01	98.92	1.47	97.44	5.903	0.049	5.95	10.063	0.009	-	0.033	0.013	0.026	10.14	1.916	0.003	0.082	0.96	0.00	0.04
Z1 14		40.61	0.26	54.09	0.01	0.04	0.18	0.29	0.47	2.56	0.01	98.52	1.08	97.44	5.925	0.044	5.97	9.989	0.002	0.006	0.061	0.018	0.030	10.11	1.398	0.004	0.599	0.70	0.00	0.30
Z3 18		39.52	0.58	53.03	0.26	0.03	0.11	0.41	0.72	3.19	0.01	97.85	1.34	96.51	5.866	0.101	5.97	9.962	0.038	0.004	0.038	0.027	0.046	10.12	1.767	0.003	0.230	0.88	0.00	0.11
Z3 19		40.42	0.43	54.42	0.05	0.06	0.08	0.20	0.35	3.46	0.01	99.49	1.46	98.03	5.892	0.074	5.97	10.039	0.008	0.009	0.028	0.012	0.022	10.12	1.884	0.004	0.112	0.94	0.00	0.06
Z3 20		40.71	0.16	54.81	b.d.	0.09	0.14	0.13	0.31	3.30	0.00	99.66	1.39	98.26	5.915	0.027	5.94	10.080	-	0.013	0.047	0.008	0.020	10.17	1.792	0.001	0.207	0.90	0.00	0.10
Z4 12		40.64	0.29	54.31	0.02	0.05	0.09	0.06	0.28	2.97	0.01	98.74	1.25	97.48	5.927	0.050	5.98	10.025	0.003	0.008	0.030	0.004	0.018	10.09	1.620	0.002	0.378	0.81	0.00	0.19
Z4 13		40.23	0.30	54.33	b.d.	0.06	0.15	0.15	0.39	3.61	0.01	99.24	1.53	97.71	5.894	0.052	5.95	10.075	-	0.009	0.050	0.010	0.025	10.17	1.978	0.004	0.018	0.99	0.00	0.01
Z4 14		39.15	0.72	54.18	0.09	b.d.	0.12	0.23	0.55	3.47	0.01	98.52	1.46	97.06	5.796	0.126	5.92	10.150	0.013	-	0.039	0.015	0.035	10.25	1.919	0.003	0.077	0.96	0.00	0.04
Z6 9		39.49	0.49	54.00	0.17	0.06	0.15	0.24	0.40	2.01	0.00	97.00	0.85	96.16	5.841	0.085	5.93	10.107	0.025	0.009	0.049	0.016	0.026	10.23	1.112	0.000	0.887	0.56	0.00	0.44
Z6 10		40.17	0.25	54.32	0.09	0.06	0.18	0.13	0.35	2.90	0.01	98.45	1.22	97.23	5.892	0.043	5.94	10.086	0.013	0.008	0.060	0.008	0.022	10.20	1.587	0.003	0.410	0.79	0.00	0.20
Z6 11		41.02	0.22	54.74	b.d.	b.d.	0.16	0.15	0.31	3.42	0.01	100.01	1.44	98.57	5.934	0.037	5.97	10.022	-	-	0.052	0.009	0.019	10.10	1.847	0.003	0.150	0.92	0.00	0.07
Z6 12		40.01	0.38	53.85	0.08	0.03	0.12	0.18	0.25	2.97	0.01	97.88	1.26	96.63	5.898	0.065	5.96	10.046	0.012	0.005	0.041	0.011	0.016	10.13	1.638	0.004	0.358	0.82	0.00	0.18
Z7 1	1	40.11	0.31	54.53	0.03	b.d.	0.13	0.12	0.31	3.31	0.01	98.85	1.40	97.45	5.882	0.054	5.94	10.122	0.004	-	0.042	0.008	0.019	10.19	1.813	0.004	0.182	0.91	0.00	0.09
Z7 2	2	40.03	0.24	54.33	0.04	0.05	0.13	0.13	0.35	3.09	0.00	98.37	1.30	97.07	5.889	0.042	5.93	10.115	0.005	0.007	0.043	0.008	0.022	10.20	1.695	0.000	0.304	0.85	0.00	0.15
Z7 3	1	40.08	0.28	54.43	0.02	b.d.	0.13	0.10	0.44	3.14	0.01	98.63	1.32	97.30	5.885	0.048	5.93	10.114	0.003	-	0.044	0.006	0.028	10.20	1.722	0.004	0.275	0.86	0.00	0.14
Z7 4	2	40.18	0.34	54.65	0.04	0.04	0.11	0.18	0.33	3.42	0.02	99.29	1.44	97.85	5.876	0.058	5.93	10.116	0.005	0.005	0.036	0.011	0.021	10.20	1.868	0.005	0.128	0.93	0.00	0.06
Z8 8		40.04	0.24	54.35	0.10	0.03	0.12	0.21	0.36	2.84	0.01	98.30	1.20	97.11	5.885	0.042	5.93	10.110	0.015	0.004	0.040	0.013	0.023	10.21	1.557	0.003	0.440	0.78	0.00	0.22
Z8 9		40.33	0.24	54.41	0.02	0.01	0.11	0.12	0.36	3.40	0.02	99.01	1.43	97.58	5.905	0.041	5.95	10.085	0.003	0.001	0.037	0.008	0.023	10.16	1.857	0.004	0.138	0.93	0.00	0.07
Z8 10		40.10	0.30	54.45	b.d.	0.04	0.16	0.22	0.35	2.41	0.00	98.02	1.02	97.01	5.881	0.051	5.93	10.108	b.d.	0.006	0.053	0.014	0.022	10.20	1.320	0.001	0.679	0.66	0.00	0.34
Z8 11		40.71	0.08	54.55	0.05	0.01	0.12	0.08	0.20	2.98	0.01	98.77	1.26	97.52	5.938	0.014	5.95	10.071	0.007	0.001	0.039	0.005	0.013	10.14	1.623	0.003	0.374	0.81	0.00	0.19
Z8 12		40.24	0.33	53.96	0.00	0.03	0.13	0.19	0.44	2.78	0.00	98.12	1.17	96.94	5.908	0.057	5.96	10.028	0.000	0.005	0.045	0.012	0.028	10.12	1.524	0.001	0.475	0.76	0.00	0.24
TW10																														
Z1 19		40.25	0.21	54.20	0.09	b.d.	0.13	0.22	0.10	1.79	0.01	96.99	0.76	96.24	5.914	0.036	5.95	10.079	0.013	-	0.042	0.014	0.006	10.16	0.983	0.004	1.014	0.49	0.00	0.51
Z1 20		40.15	0.48	53.93	0.08	0.00	0.10	0.31	0.55	3.39	0.01	99.00	1.43	97.57	5.886	0.083	5.97	10.007	0.011	0.000	0.034	0.020	0.035	10.11	1.855	0.003	0.142	0.93	0.00	0.07
Z2 1	1	40.24	0.23	54.30	b.d.	0.04	0.10	0.11	0.36	2.45	0.01	97.85	1.03	96.82	5.906	0.040	5.95	10.086	-	0.005	0.035	0.007	0.023	10.16	1.341	0.004	0.655	0.67	0.00	0.33
Z2 2	core 2	40.61	0.11	54.08	0.03	0.03	0.09	0.08	0.25	3.16	0.01	98.44	1.33	97.11	5.951	0.018	5.97	10.031	0.004	0.004	0.029	0.005	0.016	10.09	1.728	0.002	0.270	0.86	0.00	0.13
Z2 3	3	39.63	0.59	53.84	0.03	0.05	0.11	0.22	0.48	2.34	0.00	97.30	0.99	96.31	5.853	0.104	5.96	10.063	0.004	0.008	0.037	0.014	0.030	10.16	1.293	0.001	0.706	0.65	0.00	0.35
Z2 4		40.24	0.16	54.13	0.00	0.04	0.10	0.04	0.17	2.51	0.01	97.40	1.06	96.34	5.926	0.027	5.95	10.089	0.000	0.006	0.032	0.002	0.011	10.14	1.382	0.004	0.615	0.69	0.00	0.31
Z2 5		40.11	0.40	53.85	0.17	0.02	0.11	0.18	0.41	2.98	0.01	98.22	1.25	96.97	5.896	0.070	5.97	10.019	0.024	0.003	0.036	0.011	0.026	10.12	1.634	0.001	0.364	0.82	0.00	0.18
Z2 6		39.87	0.33	53.95	b.d.	0.01	0.18	0.22	0.34	2.65	b.d.	97.53	1.11	96.42	5.887	0.058	5.94	10.082	-	0.001	0.060	0.014	0.022	10.18	1.460	b.d.	0.540	0.73	b.d.	0.27
Z3 6		40.07	0.10	54.29	0.05	0.06	0.19	0.10	0.22	2.47	0.01	97.55	1.04	96.51	5.905	0.017	5.92	10.125	0.007	0.009	0.062	0.006	0.014	10.22	1.361	0.002	0.637	0.68	0.00	0.32
Z3 7		39.84	0.29	53.76	0.08	0.03	0.22	0.14	0.39	2.54	0.00	97.29	1.07	96.22	5.893	0.051	5.94	10.062	0.012	0.004	0.076	0.009	0.025	10.19	1.402	0.001	0.597	0.70	0.00	0.30
Z3 8		39.82	0.39	53.96	0.05	0.03	0.11	0.27	0.67	2.02	0.00	97.31	0.85	96.46	5.871	0.067	5.94	10.069	0.008	0.004	0.037	0.017	0.043	10.18	1.114	0.001	0.885	0.56	0.00	0.44
Z3 9		39.55	0.30	53.29	0.00	0.09	0.17	0.25	0.53	2.96	0.01	97.15	1.25	95.90	5.892	0.052	5.94	10.047	0.000	0.014	0.057	0.016	0.034	10.17	1.646	0.004	0.350	0.82	0.00	0.18
Z3 10		40.17	0.18	54.39	b.d.	0.06	0.09	0.09	0.18	2.42	0.00	97.59	1.02	96.57	5.907	0.031	5.94	10.121	-	0.009	0.032	0.006	0.011	10.18	1.329	0.001	0.670	0.66	0.00	0.33
Z5 8		40.23	0.14	53.83	b.d.	0.08	0.11	0.18	0.25	2.12	0.01	96.96	0.90	96.06	5.933	0.025	5.96	10.047	-	0.012	0.036	0.012	0.016	10.12	1.170	0.004	0.827	0.58	0.00	0.41
Z6 1		40.27	0.33	54.26	0.11	0.07	0.13	0.14	0.36	2.19	0.01	97.86	0.93	96.93	5.895	0.057	5.95	10.054	0.016	0.010	0.042	0.009	0.023	10.15	1.200	0.003	0.797	0.60	0.00	0.40
Z6 2	1	39.90	0.47	53.99	0.01	b.d.	0.10	0.35	0.55	2.90	0.01	98.29	1.22	97.06	5.871	0.082	5.95	10.054	0.002	-	0.034	0.023	0.035	10.15	1.596	0.002	0.402	0.80	0.00	0.20
Z6 3	core 2	40.17	0.20	54.05	b.d.	b.d.	0.11	0.16	0.34	3.16	0.01	98.19	1.33	96.85	5.916	0.034	5.95	10.075	-	-	0.037	0.010	0.022	10.14	1.739	0.002	0.259	0.87	0.00	0.13
Z6 4	3	39.89	0.25	53.63	0.14	0.03	0.15	0.23	0.39	2.34	0.01	97.05	0.99	96.06	5.903	0.044	5.95	10.044	0.020	0.005	0.051	0.015	0.025	10.16	1.293	0.003	0.705	0.65	0.00	0.35

Notes: Analyses with high or low totals (>101 or <95 wt%) or poor stoichiometries are omitted.
Abbreviations: b.d. = below detection.

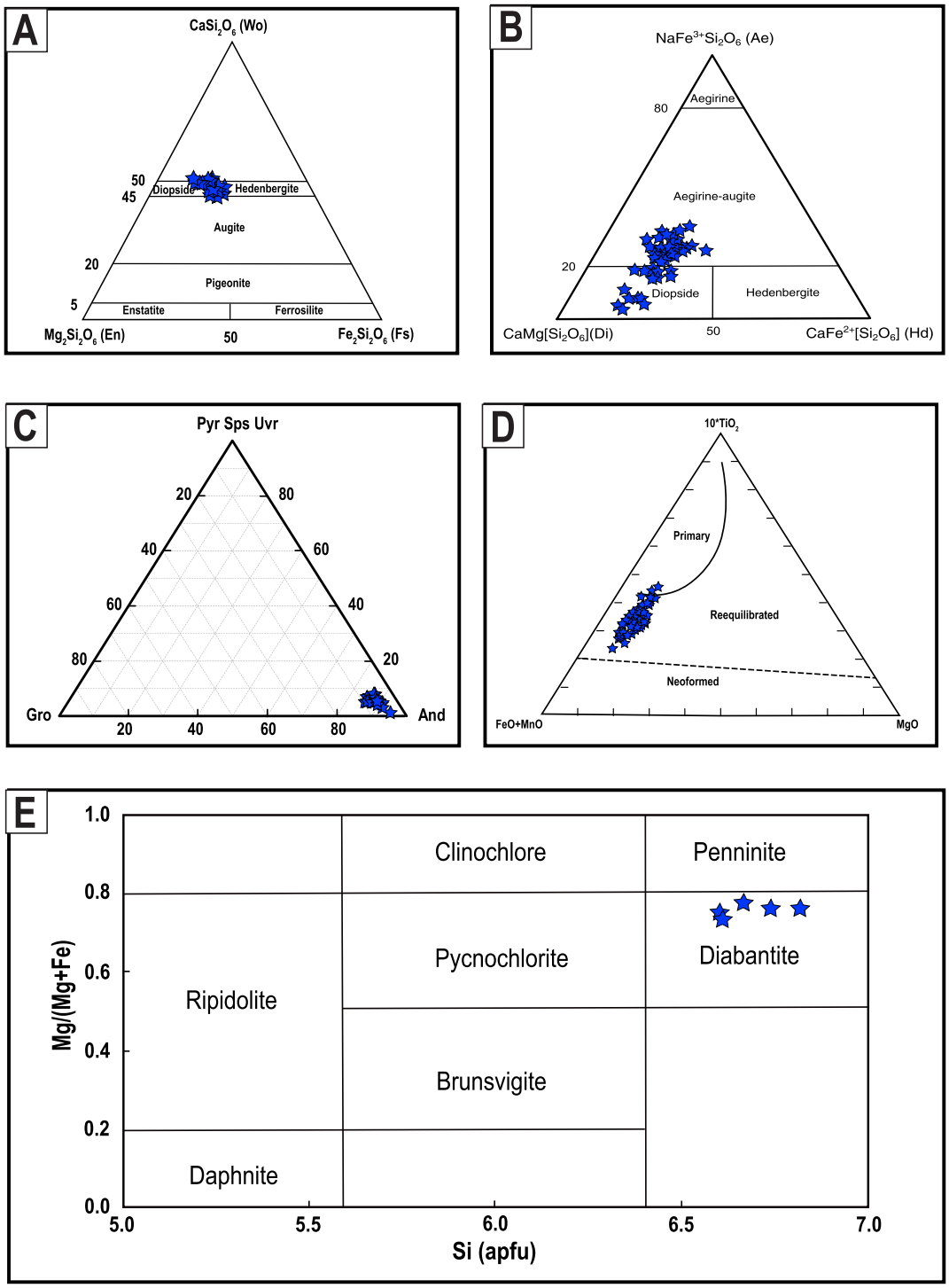

Fig. 11. Discriminating plots showing chemical compositions of the main calc-silicate phases from the Twihinate antiskarn lithotypes. (A, B) EPMA compositions of clinopyroxene plotted on Wo-En-Fs (A) and mol.% Di, Ae and Hd (B) ternary diagrams; (C) EPMA compositions of garnet plotted on Go-And-(Pyr-Sps-Uvr) ternary diagram; (D) EPMA compositions of biotite plotted on FeO + MgO-MgO-10*TiO_2 ternary diagram; (E) EPMA compositions of chlorite plotted on Si (apfu) vs Mg/(Mg + Fe) diagram. Abbreviation: Ae = aegirine; And = andradite; apfu = atomic per formula unit; En = Enstatite, Fs = ferrosilite; Fo = forsterite; Gro = grossular; Jd = jadeite; Pyr = pyrope, Sps = spessartite; Uvr = uvarovite; Wo = wollastonite.

reaction-rim structures/textures as dehydration-melting reactions resulting from high-pressure dehydration melting processes that produce a dense, refractory residuum and a K-rich silicate liquid. The occurrence of biotite/phlogopite (Fig. 4E) and K-feldspar (Montero et al., 2016; their Fig. 5B) support the K-rich nature of the produced silicate liquid.

The hypothesis of crustal assimilation is reinforced by the occurrence of calc-silicate phases such as andradite, diopside, biotite/phlogopite, and titanite; the abundance and stability of which are controlled principally by silica solubility (<2.9 wt% in carbonate melts at subvolcanic pressures; Weidendorfer et al. 2017) and silica activity, respectively. Both these parameters are commonly low in carbonatite magmas. Equally important, the development of andradite, biotite/phlogopite, titanite, and K-feldspar requires an externally derived contribution from

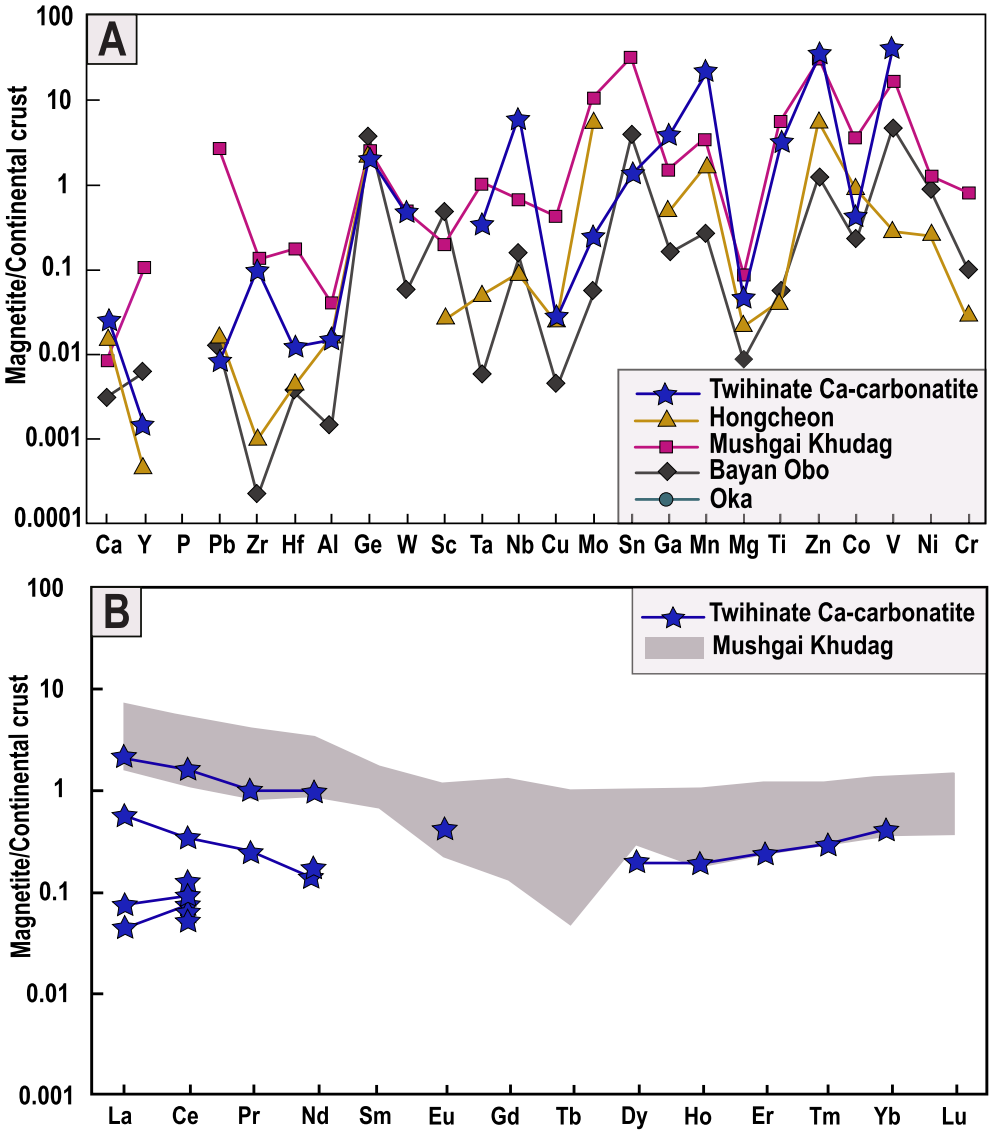

Fig. 12. Continental-crust normalized multi-elemental patterns of magnetite (A) from the Twihinate antiskarn lithotypes. Also plotted are magnetite compositions from carbonatite complexes of Hongcheon, Oka, Bayan Obo, and Mushgai Khudag. Data are from Chen et al., (2019). The bulk continental crust values are form Rudnick and Gao (2003); (B) Continental-crust normalized rare earth element patterns for magnetite from Twihinate prospect. The Mushgai Khudag compositional field is given for comparison after Chen et al. (2019). Data are normalized to bulk continental crust values form Rudnick and Gao (2003).

high Al, Ti, and alkali rock sources as these elements are strongly depleted in carbonatite melts compared with the silicate country rocks. Higher concentrations of SiO_2, Al_2O_3, K_2O, and Na_2O, among other elements, are therefore expected in carbonatitic magmas affected by crustal assimilation even at small degrees of contamination. Such geochemical trends are observed in the Twihinate antiskarn samples (Table 1). Hence, (i) the systematic enrichment of the Twihinate antiskarn in SiO_2, LILE (Sr, Ba, Th), LREE relative to HREE, and U, V, and Pb compared to carbonatite counterpart along with (ii) the compositional trend of clinopyroxene from diopside to aegirine through hedenbergite (Fig. 11A, B), and (iii) the U-rich compositions of pyrochlore, all are interpreted to reflect crustal contamination of the parent carbonatite magma. Of particular note is the symplectitic texture exhibited by titanite (Fig. 7D) which is interpreted to have formed, at magmatic conditions, in the presence of limited amounts of fluids as the result of Si assimilation from the wall-rocks (Chakhmouradian et al., 2003; Anenburg et al., 2020a). Assimilation of silicate wall-rocks is considered essential to producing silica saturation during carbonatite evolution and subsequent crystallization of the calc-silicate phases and related Nb-P-Fe ± LREE ± U-Th-rich mineralization. Accordingly, the addition of crustal silica to the crystallizing carbonatite melts appears as a first order control on antiskarn mineralogy and ore depositional processes.

In summary, the calc-silicate phases and related Nb-P-Fe ± LREE ± U-Th-rich mineralization of the Twihinate antiskarn appear to have been derived from batches of carbonatite melts that were contaminated by the silicate country rocks through which they were intruded.

11. Magnetite geochemistry as a proxy to the origin of the Twihinate and related mineralization

Trace element compositions of magnetite provide key information to distinguish magnetite with different origins, e.g., magnetite formed from melt at deeper levels of the mineral system or low-temperature hydrothermal fluids at shallower levels (e.g., Dupuis and Beaudoin, 2011; Dare et al., 2014; Nadoll et al., 2014; Chen et al., 2019; Huang and Beaudoin, 2019; and references therein). In this respect, a series of discriminant plots have been proposed for genetic and provenance purposes (Dare et al., 2014; Knipping et al., 2015) (Fig. 15). In the (Ti + V) versus (Al + Mn) diagram (Fig. 15A), the elemental compositions of Twihinate antiskarn Mag-2 plot in the field of high-temperature (>500 °C) magmatic Fe-Ti-V deposits. This overlap further reinforces the hypothesis that the antiskarn paragenesis and related Nb-P-Fe ± LREE ± U-Th ore were originally a batch of crystallized products from a magmatic source (Fig. 15B). More importantly, the overlap in elemental compositions between the Twihinate Mag-2 crystals and those from Oka and Mushgai Khudag carbonatite complexes (Fig. 15C, D) is suggestive

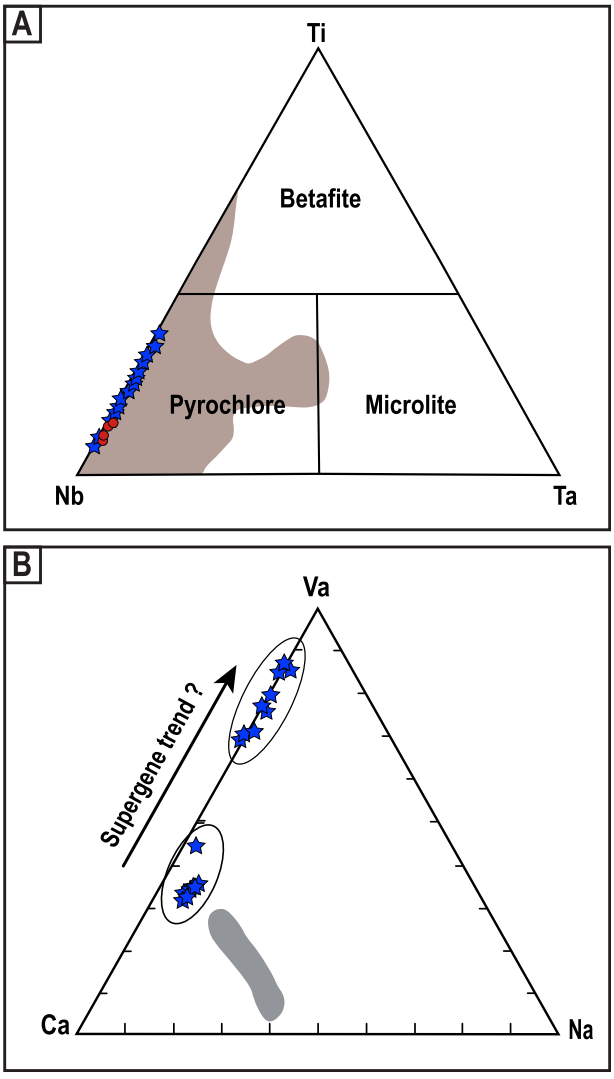

Fig. 13. Chemical compositions of pyrochlore group minerals from the Twihinate antiskarn lithotypes plotted on (A) Ti-Nb-Ta classification scheme for pyrochlore group minerals with compositional data from the selected exploration boreholes 'TWS$_5$', 'TWS$_{20}$' and 'TWS$_{32}$', and (B) Compositional variation of the A-site cations (apfu) and lattice vacancies of pyrochlore grains. Note magmatic pyrochlore crystals from the antiskarn lithotypes and those which have been affected by supergene alteration contain more A-site cations than supergene pyrochlore grains; the latter being dominated by A-site vacancies and water. Solid lines which limit the pyrochlore, betafite and microlite fields are from Atencio et al. (2010). The brown field for pyrochlore-derived carbonatite worldwide as defined by Mackay and Simandl (2015) is shown for comparison. Red dots in (A) and the grey compositional field in (B) are also shown for comparison and refer to the published data of Benaouda et al. (2020b). Abbreviation: VA = vacancy. (For interpretation of the references to color in this figure legend, the reader is referred to the web version of this article.)

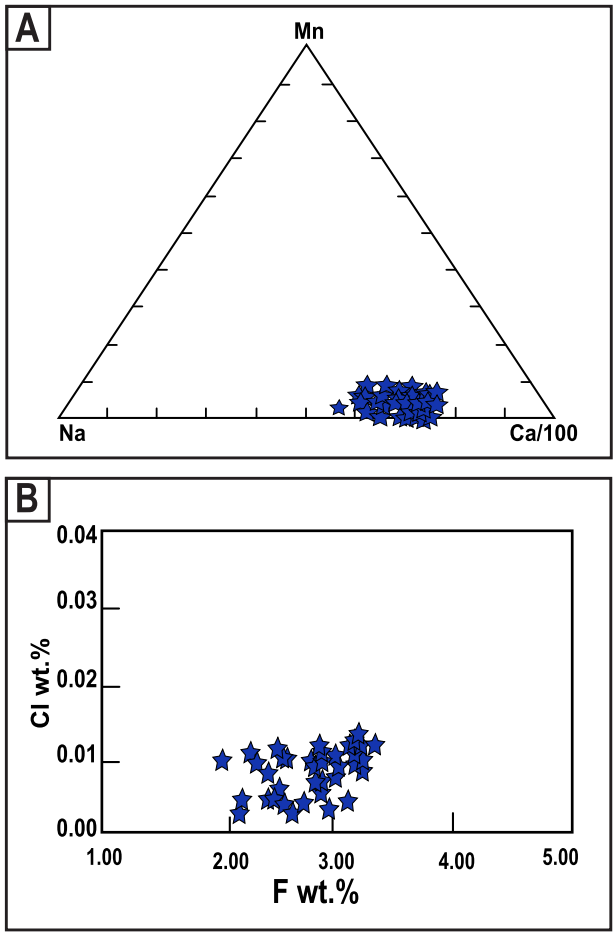

Fig. 14. Chemical compositions of apatite from the Twihinate antiskarn lithotypes plotted on Na-Mn-Ca/100 ternary diagram (A) and F wt.% vs Cl wt.% binary diagram (B).

of a common origin and magma evolution in the context of carbonatite-related environment. Additional evidence arguing for a genetic connection between the Twihinate antiskarn paragenesis and related mineralization to carbonatite melt is provided by the anomalously high Ti (up to 17 wt%), Mn (up to 2 wt%), and V (up to 1 wt%) contents of the examined magnetite crystals which correlate with their substantial enrichment in Zn, Nb, Zr, Ga, Ge, and Sn (up to ~250 ppm) (Table 6, Fig. 15D). Similarly, the low Cr abundances of Mag-2 argue again for its derivation from a carbonatite melt, consistent with previous studies that advocate that the Cr content is low in magnetite from carbonatite and related silicate rocks (Bailey and Kearns, 2002; Reguir et al., 2009; Guzmics et al., 2011). More conclusive is the geochemical trend of increasing U and Th abundances exhibited by the compositions of pyrochlore with advancing paragenetic sequence. Such evolutionary trend of increasing U and Th contents from pyrochlore to uranpyrochlore (Table 6, Fig. 15A) mimics the compositional evolution of pyrochlore group minerals from Miaoya carbonatite complex (Wu et al., 2021). Overall, these trace element signatures are consistent with precipitation from a carbonatite melt. With the simultaneous incorporation of Nb into the early crystallizing magmatic pyrochlore (Pcl-1), the residual carbonatitic melt became more Nb-depleted and U-rich (Pcl-2), which may explain the observed geochemical trend from early U-poor pyrochlore to uranpyrochlore.

In summary, our combined textural and geochemical data support the concept that leaching of silica from the surrounding Laknouk granitic rocks and its subsequent introduction into the Twihinate carbonatite system may have triggered direct precipitation of the calc-silicate paragenesis and related Nb-P-Fe ± LREE ± U-Th-rich mineralization as solid phases by reaction with chemical components present in the carbonatite melt. In this respect, it is well documented that contamination of the carbonatite melts by externally-derived silica constitutes a powerful metasomatic agent that ultimately led to development of the antiskarn mineral assemblages and related mineralization (Stoppa et al., 2021).

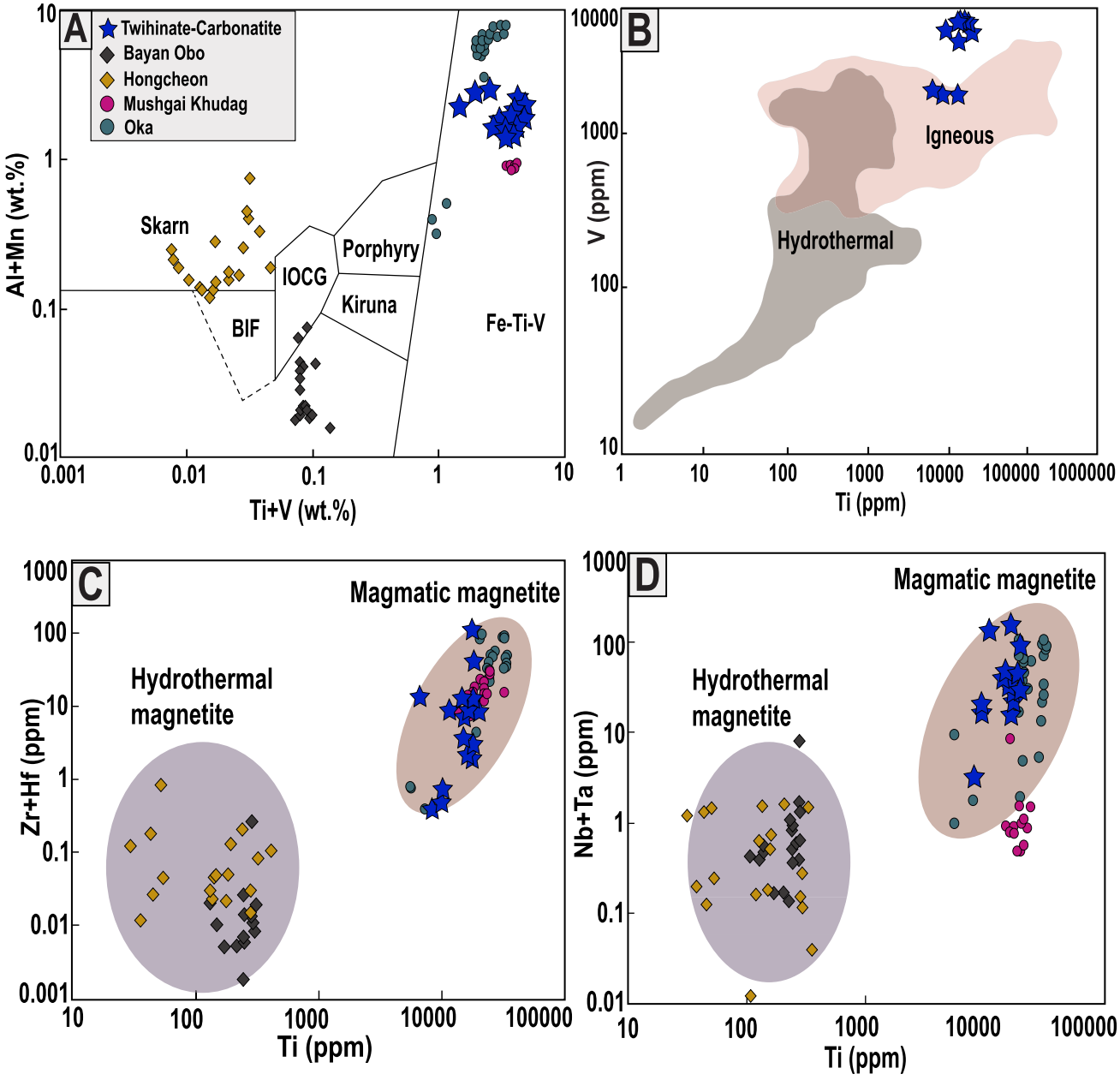

Fig. 15. Bimodal discriminating diagrams showing chemical affinities and related deposit types for magnetite from the Twihinate antiskarn lithotypes. (A) Plot of V + Ti vs Ca + Al + Mn of Twihinate magnetite compared to magnetite from different ore deposit types. Reference fields are from Dupuis and Beaudoin (2011) modified by Nadoll et al. (2014). Data of Bayan Obo, Hongcheon, Mushgai Khudag and Oka carbonatite-related magnetite are from Chen et al. (2019). *Skarn* = Fe-Cu skarn deposits; *IOCG* = iron-oxide-copper–gold deposits; *Porphyry* = porphyry Cu deposits; *Kiruna* = Kiruna apatite-magnetite deposits; *Fe-Ti, V* = magmatic Fe-Ti-oxide deposits; (B) Binary plot of Ti vs V for the Twihinate magnetite showing the position of the analyzed crystals in the field igneous magnetite. Reference fields are from Nadoll et al. (2014); (C) Ti vs Zr + Hf, and (D) Ti vs Nb + Ta diagram showing the plot of the Twihinate magnetite compositions in the magmatic field overlapping the compositions of Oka and Mushgai Khudag magnetites. The igneous and hydrothermal fields are from Nadoll et al. (2014). Data Bayan Obo, Hongcheon, Mushgai Khudag and Oka carbonatite-related magnetite are from Chen et al. (2019).

12. Implications for high-technology mineral exploration in the Moroccan Sahara and the Mauritanide belt

The correct classification of ore deposits in the early stages of mineral exploration is critical not only for genetic purposes but more importantly for a successfully conducted prospection campaign as it provides the preliminary tools to improve the accuracy of a deposit model and reveal vectors to promising targets (Laznicka, 1997; Gregory et al. 2019). This improvement is especially important when exploration programs are conducted in areas where surface outcrops are poorly exposed and stream-sediment geochemistry fails to reveal details about the prospected area at depth.

In this respect, it should be noticed that the currently applied exploration model in the Moroccan Sahara lies on the working hypothesis that mineralization was largely concentrated as a result of magmatic and magmatic-hydrothermal processes during crystallization of the Gleibat Lafhouda and Twihinate carbonatite intrusions (Fig. 2). Based on this assumption, all the past and the ongoing exploration drilling campaigns focused, or are focusing, exclusively on the carbonatite intrusions and their weathered derivatives as the primary sources

of critical metals. Unexpectedly, the occurrence of the newly defined antiskarn rocks which are interpreted to have formed through silica contamination of residual carbonatite melt may serve therefore as a vector to high-grade ore. One of prominent features of the Twihinate carbonatite and related antiskarn lithotypes resides in their diverse mineralogy, particularly for accessory and minor minerals, combined with high V and low Cr contents of the associated iron ore (i.e., vanadiferous titanomagnetite).

Compared with economic vanadium-bearing titanomagnetite deposits worldwide, titanomagnetite from the Twihinate carbonatite shows high V concentrations that are compositionally equivalent to those recorded for magnetite from the orthomagmatic vanadiferous titanomagnetite deposits such as the Bushveld complex in South Africa (Cawthorn et al., 2005), the Panzhihua layered intrusion in China (Zhou et al., 2005), the Kachkanar massif in Russia (Popov and Nikiforova, 2004), the Windimurra complex in Western Australia (Ivanic et al., 2017), and the Canadian Bell River (Matagami deposit) and the Lac Doré complexes in Québec (Taner et al., 1998; Kelley et al., 2017). Accordingly, the currently explored Twihinate prospect has the potential to become an outstanding multi-commodity exploration target, with vanadium as a by-product. These findings put new constraints on the ongoing drilling campaign which should target not only the carbonatite intrusion itself but also the surrounding country rocks proximal to the intrusion and alongside the contact intrusion-host rocks. Regionally, our results highlight the significant potential of the explored Moroccan Sahara carbonatites and those from adjacent countries such as in Mauritania where carbonatites of similar age (i.e., Cretaceous Richat structure; Fig. 2) have been reported (Matton and Jébrak, 2009). Together, these rock types and the genetically related silicate counterparts could constitute important sources of Nb, P, Fe, and LREE ± U-Th and V as well as a by-product.

13. Concluding remarks

The Twihinate prospect is currently considered as one of the most promising carbonatite-hosted strategic metals discoveries that have been made in the Moroccan Sahara over the last two decades. The Nb-P-Fe ± LREE ± U-Th-rich mineralization and associated base metal sulfides, fluorite and baryte are hosted by an Upper Cretaceous calcite carbonatite and its overlying weathered derivates. Our petrographic, mineralogical and geochemical data indicate that part of the newly discovered mineralization is related to a widespread metasomatic event which resulted in development of the Twihinate antiskarn lithotypes. The ore mineralogy consists predominantly of oxides (vanadiferous titanomagnetite), pyrochlore group minerals, phosphates (apatite, monazite), and REE-fluorcarbonates (bastnäsite-(Ce)) with subordinate amounts of sulfides (chalcopyrite, sphalerite, and galena), fluorite and baryte. In addition to the above-referenced strategic metals, the Twihinate ore is characterized by widespread occurrence of vanadiferous titanomagnetite. This V enrichment could constitute a per value for the explored occurrences through the development of mining of magnetite-bearing carbonatitic rocks and related antiskarn rocks targeting V as a by-product. Petrogenetically, we propose that the calc-silicate antiskarn rocks and related Nb-P-Fe ± LREE ± U-Th-rich mineralization were formed as a result of silica contamination of the residual carbonatite-derived melts by the surrounding Silurian-Devonian granitic rocks.

Declaration of Competing Interest

The authors declare that they have no known competing financial interests or personal relationships that could have appeared to influence the work reported in this paper.

Data availability

Data will be made available on request.

Acknowledgments

This research was made possible with help and support from the geological staff of ONHYM to whom we would like to express our deepest gratitude for supporting this project and providing access to the Twihinate property, extensive drill core sampling and advisory assistance. Our gratitude goes specifically to M. Chaib, M. Essaadaoui, and I. Laamouri. We are also indebted to M. Choquette (Université Laval, Canada) for EPMA analyses. Special appreciation is due to M. Anenburg for his thoughtful review, helpful comments and valuable suggestions which have helped improved the quality of the manuscript. We are also thankful to M. Boni for her for his insightful comments and patient revision, and H. Chen for his editorial handling and constructive review of the paper. This project gets partial funding from the European Union's Learning mobility of individuals (Project Number BE01-KA107-016242) awarded to M. Bouabdellah and J. Yans.

References

Andersen, A.K., Clark, J.G., Larson, P.B., Donovan, J.J., 2017. REE fractionation, mineral speciation, and supergene enrichment of the Bear Lodge carbonatites, Wyoming, USA. Ore Geol. Rev. 89, 780–807.

Anenburg, M., Mavrogenes, J.A., 2018. Carbonatitic versus hydrothermal origin for fluorapatite REE-Th deposits: Experimental study of REE transport and crustal "antiskarn" metasomatism. Amer. Jour. Sci 318 (3), 335–366.

Anenburg, M., Mavrogenes, J.A., Bennett, V.C., 2020a. The fluorapatite P-REE–Th vein deposit at Nolans Bore: Genesis by carbonatite metasomatism. J. Petrol. 61 (1), egaa003.

Anenburg, M., Mavrogenes, J.A., Frigo, C., Wall, F., 2020b. Rare earth element mobility in and around carbonatites controlled by sodium, potassium, and silica. Sci. Adv. 6 (41), eabb6570.

Anenburg, M., Broom-Fendley, S., Chen, W., 2021. Formation of rare earth deposits in carbonatites. Elements 17 (5), 327–332.

Atencio, D., Andrade, M.B., Christy, A.G., Gieré, R., Kartashov, P.M., 2010. The pyrochlore supergroup of minerals: nomenclature. Canad. Mineral 48, 673–698.

Bailey, D.K., Kearns, S., 2002. High-Ti magnetite in some fine-grained carbonatites and the magmatic implications. Miner. Mag 66, 379–384.

Bea, F., Montero, P., Haissen, F., El Archi, A., 2013. 2.46 Ga kalsilite and nepheline syenites from the Awsard pluton, Reguibat Rise of the West African Craton, Morocco. Generation of extremely K-rich magmas at the Archean-Proterozoic transition. Precambr. Res. 224, 242–254.

Bea, F., Montero, P., Haissen, F., Rjimati, E., Molina, J.F., Scarrow, J.H., 2014. Kalsilite-bearing plutonic rocks: the deep-seated Archean Awsard massif of the Reguibat Rise, South Morocco. West African Craton. Earth. Sci. Rev 138, 1–24.

Bea, F., Montero, P., Haissen, F., Molina, J.F., Michard, A., Lazaro, C., Mouttaqui, A., Errami, A., Sadki, O., 2016. First Evidence for Cambrian Rift-related Magmatism in the West African Craton margin: the Derraman Peralkaline Felsic Complex. Gondwana Res. 36, 423–438.

Bea, F., Montero, P., Haissen, F., Molina, J.F., Lodeiro, F.G., Mouttaqi, A., Kuiper, Y.D., Chaib, M., 2020. The Archean to Late-Paleozoic architecture of the Oulad Dlim Massif, the main Gondwanan indenter during the collision with Laurentia. Earth Sci. Rev. 208, 103273.

Bell, K., 1989. Carbonatites: Genesis and Evolution. Unwin Hyman, London.

Benaouda, R., Kraemer, D., Sitnikova, M., Goldmann, S., Freitag, R., Bouali, A., Mouttaqi, A., El Haloui, R., Essaadaoui, M., Bau, M., 2020a. Thorium-poor monazite and columbite-(Fe) mineralization in the Gleibat Lafhouda carbonatite and its associated iron-oxide-apatite deposit of the Ouled Dlim Massif, South Morocco. Gondwana Res. 7, 19–39.

Benaouda, R., Kraemer, D., Sitnikova, M., Goldmann, S., Schwarz-Schamper, U., Errami, A., Mouttaqi, A., Bau, M., 2020b. Discovery of high-grade REE-Nb-Fe mineralization associated with calciocarbonatite in south Morocco. Ore Geol. Rev. 124, 103631.

Bouabdellah, M., Chakhmouradian, A., Mouttaqi, A., Cuney, M., Ait Kassi, A., 2012. Potentiel en métaux stratégiques (REE, Nb, Zr, Ta, U, Th) des carbonatites à travers des exemples de gisements du Maroc et d'ailleurs. In Rabeau et al., eds., Programme et résumés. Ressources minérales et nouvelle économie: innovation et découvertes. Colloque international dans le cadre du 80ème Congrès de l'ACFAS: Quatrièmes journées De Launay. Ministère des Ressources naturelles et de la Faune, Québec; GM 66219, 8-9 mai 2012, p. 17.

Bouabdellah, M., Hoernle, K., Kchit, A., Duggen, S., Hauf, F., Klügel, A., Lowry, D., Beaudoin, G., 2010. Petrogenesis of the Eocene Tamazert Continental Carbonatites (Central High Atlas, Morocco): Implications for a Common Source for the Tamazert and Canary and Cape Verde Island Carbonatites. J. Petrol. 51, 1655–1686.

Bouabdellah, M., 2013. Les carbonatites et les métaux stratégiques (REE, Li, Nb, Zr, Ta, U, Th) : enjeux et perspectives de recherches à travers des exemples de gisements du Maroc et d'ailleurs. 8ème édition du Colloque International Magmatisme, Métamorphisme et Minéralisations Associées (3MA), 8 au 12 mai 2013, Marrakech – Maroc. pp. 9.

Boukirou, W., Bouabdellah, M., Chakhmouradian, A.R., Mouttaqi, A., Reguirb, F.H., E.P., Cuney, M., Jébrak, M., Yans, J., Hoernle, K.,, 2022. Petrogenesis of the late

Paleoproterozoic Gleibat Lafhouda dolomite carbonatite (West African Craton Margin, Moroccan Sahara) and its relevance to the onset of fragmentation of the Columbia supercontinent. Chem. Geol. 594, 120764.
Broom-Fendley, S., Wall, F., Spiro, B., Ullmann, C.V., 2017. Deducing the source and composition of rare earth mineralising fluids in carbonatites: insights from isotopic (C, O, 87Sr/86Sr) data from Kangankunde. Malawi. Contri. Miner. Petrol 172, 96.
Cangelosi, D., Broom-Fendley, S., Banks, D., Morgan, D., Yardley, B., 2020. Light rare earth element redistribution during hydrothermal alteration at the Okorusu carbonatite complex. Namibia. Miner. Mag 84, 49–64.
Caro, G., Kopylova, M.G., Creaser, R.A., 2004. The hypabyssal 5034 kimberlite of the Gahcho Kue cluster, southeastern Slave craton, northwest territories, Canada: A granite-contaminated group-I kimberlite. Can. Miner. 42, 183–207.
Cawthorn, R.G., Barnes, S.J., Ballhaus, C., Malitch, K.N., 2005. Platinum group element, chromium, and vanadium deposits in mafic and ultramafic rocks. In Hedenquist, J. W., Thompson, J.F.H., Goldfarb, R.J., Richards, J.P., editors, One Hundredth Anniversary Volume. Society of Economic Geology. doi.org/10.5382/AV100.
Chakhmouradian, A.R., Dahlgren, S., 2021. Primary inclusions of burbankite in carbonatites from the Fen complex, southern Norway. Miner. Petrol 115, 161–171.
Chakhmouradian, A.R., Reguir, E.P., Mitchell, R.H., 2003. Titanite in carbonatitic rocks: Genetic dualism and geochemical significance. Per. Mineral 72, Special Issue Eurocarb, 107–113.
Chakhmouradian, A.R., Mumin, A.H., Demény, A., Elliott, B., 2008. Postorogenic carbonatites at Eden Lake, Trans-Hudson orogen (northern Manitoba, Canada): Geological setting, mineralogy and geochemistry. Lithos 103, 503–526.
Chakhmouradian, A.R., Reguir, E.P., Zaitsev, A.N., Couëslan, C., Xu, C., Kynický, J., Mumin, A.H., Yang, P., 2017. Apatite in carbonatitic rocks: Compositional variation, zoning, element partitioning and petrogenetic significance. Lithos 274–275, 188–213. https://doi.org/10.1016/j.lithos.2016.12.037.
Chakhouradian, A.R., Wall, F., 2012. Rare Earth Elements: Rare earth mineralization in igneous rocks: Sources and processes. Elements 8, 347–353.
Chen, W., Ying, W.C., Bai, T., Zhang, J.J., Jiang, S.Y., Zhao, K.D., Shin, D., Kynicky, J., 2019. In situ major and trace element analysis of magnetite from carbonatiterelated complexes: Implications for petrogenesis and ore genesis. Ore Geol. Rev. 107, 30–40.
Chmyz, L., Azzone, R.G., Ruberti, E., Marks, M.A.W., Saraiva dos Santos, T.J., 2022. Olivines as probes into assimilation of silicate rocks by carbonatite magmas: Unraveling the genesis of reaction rocks from the Jacupiranga alkaline–carbonatite complex, southern Brazil. Lithos 416–417, 106647.
Dare, S., Barnes, S.J., Beaudoin, G., 2012. Variation in trace element content of magnetite crystallized from a fractionating sulfide liquid, Sudbury, Canada: Implications for provenance discrimination. Geochim. Cosmochim. Acta 88, 27–50. https://doi.org/10.1016/j.gca.2012.04.032.
Dare, S., Barnes, S.J., Beaudoin, G., Meric, J., Boutroy, E., 2014. Trace elements in magnetite as petrogenetic indicators. Miner. Depos 49, 785–796. https://doi.org/10.1007/s00126-014-0529-0.
Dupuis, C., Beaudoin, G., 2011. Discriminant diagrams for iron oxide trace element fingerprinting of mineral deposit types. Miner. Depos 46, 319–335.
Elliott, H.A.L., Wall, F., Chakhmouradian, A.R., Siegfried, P.R., Dahlgren, S., Weatherley, S., Finch, A.A., Marks, M.A.W., Dowman, E., Deady, E., 2018. Fenites associated with carbonatite complexes: A review. Ore Geol. Rev. 93, 38–59.
Foster, M.D., 1960. Interpretation of the composition of trioctahedral micas. U.S, Geological Survey Professional Paper, p. 49.
Gärtner, A., Villeneuve, M., Linnemann, U., El Abdelkrim, A., Bellon, H., 2013. An exotic terrane of Laurussian affinity in the Mauritanides and Souttoufides (Moroccan Sahara). Gondwana Res. 24, 687–699.
Gärtner, A., Villeneuve, M., Linnemann, U., Gerdes, A., Youbi, N., Guillou, O., Rjimati, E. C., 2016. History of the West African Neoproterozoic Ocean: Key to the geotectonic history of circum-Atlantic Peri-Gondwana (Adrar Souttouf Massif, Moroccan Sahara). Gondwana Res. 29, 220–223.
Giebel, R.J., Marks, M.A.W., Gauert, C.D.K., Markl, G., 2019. A model for the formation of carbonatite-phoscorite assemblages based on the compositional variations of mica and apatite from the Palabora Carbonatite Complex, South Africa. Lithos 324–325, 89–104.
Goldoff, B., Webster, J.D., Harlov, D.E., 2012. Characterization of fluor-chlorapatites by electron probe microanalysis with a focus on time-dependent intensity variation of halogens. Amer. Mineral 97, 1103–1115.
Gonzàlvez-Alvarez, I., Stoppa, F., Yang, X.Y., Porwal, A., 2021. Introduction to the special Issue, insights on carbonatite and their mineral exploration approach: A challenge towards resourcing critical metals. Ore Geol. Rev. 133, 104073.
Goodenough, K.M., Wall, F., Merriman, D., 2018. The rare earth elements: Demand, global resources, and challenges for resourcing future generations. Nat. Resour. Res. 27, 201–216.
Gregory, D.D., Cracknell, M.J., Large, R.R., McGoldrick, P., Kuhn, S., Maslennikov, V.V., Baker, M.J., Fox, N., Belousov, I., Figueroa, M.C., Steadman, J.A., Fabris, A.J., Lyons, T.W., 2019. Distinguishing ore deposit type and barren sedimentary pyrite using laser ablation-inductively coupled plasma-mass spectrometry trace element data and statistical analysis of large data sets. Econ. Geol. 114 (4), 771–786.
Groves, D.I., Bierlein, F.P., Meinert, L.F., Hitzman, M.W., 2010. Iron Oxide Copper-Gold (IOCG) deposits through Earth history: Implications for origin, lithospheric setting, and distinction from other epigenetic iron oxide deposit. Econ. Geol. 105, 641–654.
Guzmics, T., Mitchell, R.H., Szabó, C., Berkesi, M., Milke, R., Abart, R., 2011. Carbonatite melt inclusions in coexisting magnetite, apatite and monticellite in Kerimasi calciocarbonatite, Tanzania: melt evolution and petrogenesis. Contributions Miner. Petrol 161, 177–196.
Hacker, B., Luffi, P., Lutkov, V., Minaev, V., Ratschbacher, L., Plank, T., Ducea, M., Patino-Douce, A., McWilliams, M., Metcalf, J., 2005. Near-ultrahigh pressure processing of continental crust: Miocene crustal xenoliths from the Pamir. Jour. Petrol. 46 (8), 1661–1687. https://doi.org/10.1093/petrology/egi030.
Haissen, F., Montero, P., Cambeses, A., Bea, F., Molina, J.F., Mouttaqi, A., Gonzalez-Lodeiro, F., Sadki, O., Errami, A., 2018. Petrogenesis of Derraman Peralkaline granite (Oulad Dlim Massif, West African Craton Margin, Morocco): New constraints from zircon Hf and O isotopic compositions. Compt. Rendus Geosci 50, 236–244.
Hogarth, D., Williams, C., Jones, P., 2000. Primary zoning in pyrochlore group minerals from carbonatites. Miner. Mag 64, 683–697.
Huang, X.W., Beaudoin, G., 2019. Textures and chemical compositions of magnetite from Iron Oxide Copper-Gold (IOCG) and Kiruna-type Iron Oxide-Apatite (IOA) deposits and their implications for ore genesis and magnetite classifications schemes. Econ. Geol. 114 (3), 653–979.
Ivanic, T.J., Nebel, O., Brett, J., Murdie, R.E., 2017. The Windimurra igneous complex: An Archean Bushveld? In: Gessner, K., Blenkinsop, T. G. and Sorjonen-Ward, P. (eds) Characterization of Ore-Forming Systems from Geological, Geochemical and Geophysical Studies. Geological Society, London, Special Publications, 453(1): SP453.1, https://doi.org/10.1144/SP453.1.
Kelley, K.D., Scott, C.T., Polyak, D.E., and Kimball, B.E., 2017. Vanadium, chap. U of Schulz, K.J., DeYoung, J.H., Jr., Seal, R.R., II, and Bradley, D.C., eds., Critical mineral resources of the United States—Economic and environmental geology and prospects for future supply: U.S. Geological Survey Professional Paper 1802, p. U1–U36, https://doi.org/ 10.3133/pp1802U.
Knipping, J.L., Bilenker, L.D., Simon, A.C., Reich, M., Barra, F., Deditius, A.P., Lundstrom, C., Bindeman, I., Munizaga, R., 2015. Giant Kiruna-type deposits form by efficient flotation of magmatic magnetite suspensions. Geology 43 (7), 591–594.
Kozlov, E., Fomina, E., Sidorov, M., Shilovskikh, V., Bocharov, V., Chernyavsky, A., Huber, M., 2020. The Petyayan-Vara carbonatite-hosted rare earth deposit (Vuoriyarvi, NW Russia): Mineralogy and geochemistry. Minerals 10 (1), 73. https://doi.org/10.3390/min10010073.
Laznicka, P., 1997. Quantitative Relationships among Giant Deposits of Metal. Econ. Geol. 94, 455–473.
Lécorché, J.P., Bronner, G., Dallmeyer, R.D., Rocci, G., Roussel, J., 1991. In: The Mauritanide Orogen and Its NorThern Extensions (Western Sahara and Zemmour), West Africa. The West African Orogen and Cirum-Atlantic Correlatives, pp. 187–227.
Li., W., Chakraborty, S., Nagashima, K., Costa, F.,, 2020. Multicomponent diffusion of F, Cl and OH in apatite with application to magma ascent rates. Earth Planet. Sci. Letters 550, 116545.
Lima, N.M., Azzone, R.G., Chmyz, L., Guarino, V., Ruberti, E., Silva, S., Svisero, D.P., 2020. Petrographic, geochemical, and isotopic evidence of crustal assimilation processes in the Indaiá-II kimberlite, Alto Paranaíba province, southeast Brazil. Can. Miner. 58, 1–23.
Locock, A.J., 2008. An Excel spreadsheet to recast analyses of garnet into end-member components and a synopsis of the crystal chemistry of natural silicate garnets. Comput. Geosci. 34 (12), 1769–1780.
Mackay, D.A.R., Simandl, G.J., 2015. Pyrochlore and columbite-tantalite as indicator minerals for specialty metal deposits. Geochemistry: Exploration. Environment, Analysis 15, 167–178. https://doi.org/10.1144/geochem2014-289.
Matton, G., Jébrak, M., 2009. The Cretaceous Peri-Atlantic Alkaline Pulse (PAAP): Deep mantle plume origin or shallow lithospheric break-up. Tectonophysics 460, 1–12.
Matton, G., Jébrak, M., 2014. The ‘‘eye of Africa’’ (Richat dome, Mauritania): An isolated Cretaceous alkaline–hydrothermal complex. J. Afr. Earth Sc. 97, 109–124.
McDonough, W.F., Sun, S.S., 1995. The composition of the earth. Chem. Geol. 120, 2523–2553.
Meinert, L.D., Dipple, G.M., Nicolescu, S., 2005. World skarn deposits. Econ. Geol 100th Anniversary 299–336.
Michard, A., Soulaimani, A., Hoeffner, C., Ouanaimi, H.L.B., Rjimati, E.C., Saddiqi, O., 2010. The South-Western Branch of the Variscan Belt: evidence from Morocco. Tectonophysics 492, 1–24.
Molina, J.F., Bea, F., Montero, P., Haissen, F., Gonzalez-Lodeiro, F., Errami, A., Sadki, O., Moreno, J.A., Cambeses, A., Mouttaqi, A., 2018. High-P amphibolite-facies metamorphism in the Adrar-Souttouf Metamafic Complex, Oulad Dlim Massif (West African Craton margin, Morocco). Compt. Rendus Geosci 350, 245–254.
Montero, P., Haissen, F., El Archi, A., Rjimati, E., Bea, F., 2014. Timing of Archean crust formation and cratonization in the Awsard-Tichla zone of the NW Reguibat Rise, West African Craton. A SHRIMP, Nd-Sr isotopes, and geochemical reconnaissance study. Precambr. Res. 242, 112–137.
Montero, P., Haissen, F., Mouttaqui, A., Molina, J.F., Errami, A., Sadki, O., Cambeses, A., Bea, F., 2016. Contrasting SHRIMP U-Pb zircon ages of two carbonatite complexes from the peri-cratonic terranes pf the Reguibat Shield: Implications for the lateral extension of the West African Craton. Gondwana Res. 38, 238–250.
Moore, M., Chakhmouradian, A.R., Mariano, A.N., Sidhu, R., 2015. Evolution of rare-earth mineralization in the Bear Lodge carbonatite, Wyoming: Mineralogical and isotopic evidence. Ore Geol. Rev. 64, 499–521.
Nachit, H., Ibhi, A., Abia, E.-H., Ben Ouhoud, M., 2005. Discrimination between primary magmatic biotites, reequilibrated biotites and neoformed biotites. C.R. Geosci. 337 (16), 1415–1420.
Nadoll, P., Angerer, T., Mauk, J.L., French, D., Walshe, J., 2014. The chemistry of hydrothermal magnetite: a review. Ore Geol. Rev. 61, 1–32.
Pandur, K., Ansdell, K.M., Kontak, D.J., 2015. Graphic-textured inclusions in apatite: Evidence for pegmatitic growth in a REE-enriched carbonatitic system. Geology 43, 547–550.
Pandur, K., Ansdell, K.M., Kontak, D.J., Halpin, K.M., Creighton, S., 2016. Petrographic and mineral chemical characteristics of the Hoidas Lake deposit, northern Saskatchewan, Canada: constraints on the origin of adistal magmatic-hydrothermal REE system. Econ. Geol. 111, 667–694.

Paton, C., Hellstrom, J., Paul, B., Woodhead, J., Hergt, J., 2011. Iolite: Freeware for the visualisation and processing of mass spectrometric data. J. Anal. Atom. Spectrometry 26 (12), 2508–2518. https://doi.org/10.1039/c1ja10172b.

Pdah, D.S.M., Khonglah, M.A., 2022. Orbicular and Nodular Structures in Carbonatite of the Sung Valley Ultramafic-Alkaline-Carbonatite Complex, Shillong Plateau, Meghalaya, NE India: Their Petrogenetic Implications. Jour. Geol. Soc. India 98, 635–640.

Popov, V.S., Nikiforova, N.F., 2004. Ultramafic rocks, gabbroids, and titanomagnetic ore at Kachkanar, the Central Urals: An integrated petrological model. Geochem. Int. 42 (1), 11–25.

Pyle, D.M., Dawson, J.B., Ivanovich, M., 1991. Short-lived decay series disequilibria in the natrocarbonatite lavas of Oldoinyo Lengai, Tanzania: constraints on the timing of magma genesis. Earth Planet. Sci. Lett. 105, 378–396.

Reguir, E.P., Chakhmouradian, A.R., Halden, N.M., Malkovets, V.G., Yang, P., 2009. Major- and trace-element compositional variation of phlogopite from kimberlites and carbonatites as a petrogenetic indicator. Lithos 112, 372–384.

Rjimati, E., Zemmouri, A., 2002. Mémoire explicatif de la carte géologique du Maroc, feuille d'Awsard. Notes et Mémoires du Service Géologique du Maroc, 439 bis.

Rudnick, R.L., Gao, S., 2003. Composition of the continental crust. In: The Crust, vol. 3 (ed. R. L. Rudnick). Elsevier, pp. 1-64.

Simandl, G.J., Paradis, S., 2018. Carbonatites: related ore deposits, resources, footprint, and exploration methods. Appl. Earth Sci. 127 (1677), 1–30.

Sougy, J., 1962. West African Fold Belt. Geol. Soc. Am. Bull. 73, 871–876.

Sougy, J., Bronner, G., 1969. Nappes hercyniennes au Sahara espagnol méridional (tronçon nord des Mauritanides). In: Coll. Géol. africaine. Clermont-Ferrand, 9–12 avril. Ann. Fac. Sc. Univ. Clermont 41, 75–76 Géol. et Miner. Fasc.19.

Stock, M.J., Humphreys, M.C., Smith, V.C., Johnson, R.D., Pyle, D.M., Eimf,, 2015. New constraints on electron-beam induced halogen migration in apatite. Am. Mineral. 100, 281–293.

Stoppa, F., Cirilli, S., Sorci, A., Broom-Fendley, S., Principe, C., Perna, M.G., Rosatelli, G., 2021. Igneous and sedimentary 'limestones': the puzzling challenge of a converging classification. Geological Society, London, Special Publications, p. 520.

Stormer, J.C., Pierson, M.L., Tacker, R.C., 1993. Variation of F-X-ray and Cl-X-ray intensity due to anisotropic diffusion in apatite during electron-microprobe analysis. Amer. Mineral 78, 641–648.

Taner, M.F., Ercit, T.S., Gault, R.A., 1998. Vanadium-bearing magnetite from the Matagami and Chibougamau mining districts, Abitibi, Québec, Canada. Exploration Mining Geology 7 (4), 299–311.

Teiber, H., Marks, M.A.W., Arzamastsev, A.A., Wenzel, T., Markl, G., 2015. Compositional variation in apatite from various host rocks: clues with regards to source composition and crystallization conditions. Neues Jahrb. Mineral. Abh. 192 (2), 151–167. https://doi.org/10.1127/njma/2015/0277.

Verplanck, P.L., Mariano, A.N., Mariano, A.Jr., in Rare Earth and Critical Elements in Ore Deposits, Verplanck, P.L., and Hitzman, M.W. Eds. (Society of Economic Geologists, Littleton, Colorado, USA, 2016), chap. 1, pp. 5–32.

Villeneuve, M., Bellon, H., El Archi, A., Sahabi, M., Rehault, J.P., Olivet, J.L., Aghzer, A. M., 2006. Evénements panafricains dans l'Adrar Souttouf (Sahara marocain). Compt. Rendus Geosci 338, 359–367.

Villeneuve, M., Gartner, A., Youbi, N., El Archi, A., Vernhet, E., Rjimati, E.C., Linnemann, U., Bellon, H., Gerdes, A., Guillou, O., Corsini, M., Paquette, J.L., 2015. The southern and central parts of the "Souttoufide" belt. Northwest Africa. J. Afr. Earth Sci 112, 451–470.

Wall, F., 2014. Rare earth elements. In: Critical Metals Handbook. John Wiley & Sons, Oxford, pp. 312–339.

Walter, B.F., Parsapoor, A., Braunger, S., Marks, M.A.W., Wenzel, T., Martin, M., Markl, G., 2018. Pyrochlore as a monitor for magmatic and hydrothermal processes in carbonatites from the Kaiserstuhl volcanic complex (SW Germany). Chem. Geol. 498, 1–16.

Walter, B.F., Giebel, R.J, Marlow, A.G., Siegfried, P.R., Marks, M., Markl, G., Palmer, M. Kolb, J. 2022. The Kieshöhe carbonatites of southwestern Namibia – the post-magmatic role of silicate xenoliths on REE mobilisation. Communications of the Geological Survey of Namibia, 25, 1-31.

Wang, Z.Y., Fan, H.R., Zhou, L., Yang, K.F., Hai-Dong, S., 2020. Carbonatite-related REE deposits: An overview. Minerals 10, 965. https://doi.org/10.3390/min10110965.

Wei, C.W., Xu, C., Chakhmouradian, A.R., Brenna, M., Kynicky, J., Song, W.L., 2020. Carbon–strontium isotope decoupling in carbonatites from Caotan (Qinling, China): implications for the origin of calcite carbonatite in orogenic settings. Jour Petrol 61 (2), egaa024.

Weidendorfer, D., Schmidt, M.W., Mattsson, H.B., 2017. A common origin of carbonatite magmas. Geology 45, 507–510.

Weng, Z., Jowitt, S.M., Mudd, M.G., Haque, N., 2015. A detailed assessment of global rare earth element resources: Opportunities and challenges. Econ. Geol. 110, 1925–1952.

Woolley, A., Church, A., 2005. Extrusive carbonatites: a brief review. Lithos 85, 1–14.

Wu, B., Hu, Y.K., Bonnetti, C., Xu, C., Wang, R.C., Zhang, Z.S., Li, Z.Y., Yin, R., 2021. Hydrothermal alteration of pyrochlore group minerals from the Miaoya carbonatite complex, central China and its implications for Nb mineralization. Ore Geol. Rev. 132, 104059.

Yaxley, G., Anenburg, M., Tappe, S., Decrée, S., Guzmics, T., 2022. Carbonatites – Classification, Sources, Evolution and Emplacement. Annu. Rev. Earth Planet. Sci. 50 https://doi.org/10.1146/annurev-earth-032320-104243.

Zaitsev, A., Demény, A., Sindern, S., Wall, F., 2002. Burbankite group minerals and their alteration in rare earth carbonatites: source of elements and fluids: Evidence from C-O and Sr–Nd isotopic data. Lithos 62, 15–33.

Zaitsev, A.N., Wall, F., Le Bas, M.J., 1998. REE-Sr-Ba minerals from the Khibina carbonatites, Kola Peninsula, Russia: their mineralogy, paragenesis and evolution. Miner. Mag. 62, 225–250.

Zharikov, V.A., Pertsev, N.N., Rusinov, V.L., Callegari, E., Fettes, D.J., 2007. Metasomatism and metasomatic rocks. Recommendations by the IUGS Sub-commission of the systematics of metamorphic rocks. [available at https://www.bgs.ac.uk/scmr/products.html].

Zhou, M.F., Robinson, P.T., Lesher, C.M., Keays, R.R., Zhang, C.J., Malpas, J., 2005. Geochemistry, petrogenesis and metallogenesis of the Panzhihua gabbroic layered intrusion and associated Fe-Ti-V oxide deposits, Sichuan Province. SW China. Jour. Petrology 46, 2256–2380.